Title

Characterization of Barium Titanate and Strontium Titanate Nanoparticles Synthesized by Hydrothermal and Molten-Salt Methods

Author

Zhou, Jin

Publication Date

2022

UNIVERSITY OF CALIFORNIA SAN DIEGO

Characterization of Barium Titanate and Strontium Titanate Nanoparticles Synthesized by Hydrothermal and Molten-Salt Methods

A Thesis submitted in partial satisfaction of the requirements
for the degree Master of Science

in

Materials Science and Engineering

by

Jin Zhou

Committee in charge:

Professor Olivia Graeve Chair
Professor Javier Garay
Professor Jian Luo

2022

The Thesis of Jin Zhou is approved, and it is acceptable in quality and form for publication on microfilm and electronically.

University of California San Diego

2022

TABLE OF CONTENTS

LIST OF FIGURES

LIST OF TABLES

ABSTRACT OF THE THESIS

Characterization of Barium Titanate and Strontium Titanate Nanoparticles Synthesized by Hydrothermal and Molten-Salt Method

by

Jin Zhou

Master of Science in Materials Science and Engineering

University of California San Diego, 2022

Professor Olivia Graeve, Chair

This thesis mainly focused on investigating the suitable synthesis methods to get barium titanate ($BaTiO_3$) and strontium titanate ($SrTiO_3$) nanocubes without using any capping agents. Two synthesis methods (hydrothermal and molten-salt) were used to synthesize $BaTiO_3$ and $SrTiO_3$ nanoparticles. X-ray diffraction (XRD) was used to identify phases and determine the phase purity of synthesized $BaTiO_3$ and $SrTiO_3$ nanoparticles. The morphology and formation mechanisms were investigated through scanning electron microscopy (SEM) and transmission electron microscopy (TEM). It was verified that $BaTiO_3$ nanocubes can be successfully synthesized by molten-salt method, while $SrTiO_3$ nanocubes were obtained by hydrothermal method. The synthesized nanocubes for both materials have high crystallinity and high purity.

The formation mechanism of $BaTiO_3$ nanocubes was proposed due to the low surface energy of {100} crystal planes. Crystal planes with low surface energy are preferred in the crystal growth stage. The formation of $SrTiO_3$ nanocubes was proposed due to the crystal growth of {100} crystal planes and face-to-face attachment. These mechanisms provided clear explanations for the formation of $BaTiO_3$ and $SrTiO_3$ nanocubes without using any capping agents, which can be applied to other metal oxide nanocubes. Future studies can be focused on the synthesis of other metal oxide nanocubes by using the formation mechanisms proposed in this thesis.

INTRODUCTION

Metal oxides play an important role in many applications, such as catalysis [1], gas sensors [2], energy conversion devices [3], and biomedical materials [4]. Compared with bulk materials (larger than 100 nm), metal oxide nanoparticles (the size is in the range of 1 – 100 nm) have been extensively investigated because of their excellent properties.

(1) Large surface area: Metal oxide nanoparticles possess larger surface area than the bulk materials, which is beneficial for gas sensing and catalytic performance [1], [2]. The interaction between target molecules and the surface of metal oxide nanoparticles determines the sensitivity and activity of the sensors and catalysts, therefore, metal oxide nanoparticles with larger surface area have better sensitivity and activity than bulk materials.

(2) Quantum mechanical effect: When the particle size decreases into nanoscale (1 – 100 nm), quantum mechanics become dominant, and nanoparticles exhibit unique optical and electrical properties. Due to the quantum effect of metal oxide nanoparticles, the absorption of solar radiation and electron transportation improve significantly, which leads to the better solar cell performance and higher electrical conductivity [5], [6].

(3) Better magnetic properties: Metal oxide nanoparticles possess much better magnetic properties than bulk materials. For example, saturation and remanent magnetization value of metal oxide nanoparticles are four orders of magnitude higher than of bulk materials [7]–[10].

(4) Excellent mechanical properties: Metal oxide nanoparticles show unique mechanical properties compared with bulk materials. Some metal oxide nanoparticles, such as ZrO_2 and TiO_2, exhibit superplasticity [1]. This property enables metal oxide to endure extensive tensile deformation without necking and fracture.

(5) Chemical properties: Metal oxide nanoparticles show better chemical reactivity than bulk materials, since by decreasing the particle size, the amount of structural and electronic defects increase [2]. Metal oxide nanoparticles have more oxygen vacancies on the surfaces than the bulk materials, which leads to better redox properties and chemical reactivity [1].

1. SIZE-PROPERTY AND MORPHOLOGY-PROPERTY DEPENDENCE OF METAL OXIDE NANOPARTICLES

Despite the unique advantages of metal oxide nanoparticles compared with bulk materials, the properties of metal oxide nanoparticles, such as electrical, dielectric, magnetic, optical, catalytic and chemical properties, also significantly depend on their size and morphology. Therefore, it is important to study how the size and morphology affect the properties of metal oxide nanoparticles. There have been many studies focusing on the size-property and morphology-property relationship. For example, it was verified that saturation magnetization and remanent magnetization value highly depend on the size and morphology of metal oxide nanoparticles. Yang et al. [11] synthesized Fe_3O_4 nanocubes with different sizes (6.5 nm, 15 nm and 30 nm) through a one-pot synthesis method. With increasing the particle size, the saturation magnetization value increased accordingly (at 300 K, 6.5 nm: 39.5 emu g^{-1}; 15.0 nm: 80.5 emu g^{-1}; 30 nm: 83.0 emu g^{-1}). In addition, Jiang et al. [12] synthesized α-Fe_2O_3 nanocubes through microwave-assisted solvothermal method. The saturation magnetization value changed from 8 emu g^{-1} to 30 emu g^{-1}, due to the increase of the particle size from 13 nm to 28 nm. Song et al. [13] synthesized $CoFe_2O_4$ nanocubes and nanospheres through a combination of nonhydrolytic reaction and seed-mediated growth and found that saturation magnetization and remanent magnetization value depended on the size of $CoFe_2O_4$ nanoparticles; the corresponding coercivity was also highly dependent on the morphology of $CoFe_2O_4$ nanoparticles. Furthermore, Sathya et al. [14] synthesized $Co_xFe_{3-x}O_4$

through a thermal decomposition method by changing the amount of cobalt precursor (cobalt acetylacetonate). The saturation magnetization decreased from 74 emu g^{-1} to 42 emu g^{-1} when the corresponding size changed from 18 nm to 27 nm.

Besides saturation and remanent magnetization, the size and morphology also influence the superparamagnetic properties, ferromagnetic properties and magnetic anisotropy density of metal oxide nanoparticles. Yang et al. [11] and Song et al. [12] found that at room temperature small Fe_3O_4 and $CoFe_2O_4$ nanocubes exhibited superparamagnetic properties, while large nanocubes possessed ferromagnetic properties. Elsayed et al. [15] synthesized Fe_3O_4 nanocubes and nanospheres through a β-amyrin assisted solvothermal method. Compared with nanospheres, Fe_3O_4 nanocubes possessed a larger magnetic anisotropy density (2.11×10^6 erg/cm^3 for nanocubes and 3.46×10^5 erg/cm^3 for nanospheres).

The biomedical properties of metal oxide nanoparticles also depend on their size and morphology. For example, hyperthermia treatment and MRI performance highly depend on the specific absorption rate (SAR) and r_2 relaxivity of metal oxide nanoparticles, while the size and morphology of metal oxide nanoparticles will significantly affect SAR and r_2 relaxivity. Based on the characterization results of $Co_xFe_{3-x}O_4$ nanoparticles with a size of 20 nm, SAR was found to be about 915 W/g and r_2 relaxivity value was about 958 mM^{-1} s^{-1}, which makes it an excellent material for hyperthermia treatment and a promising contrast agent for magnetic resonance imaging [14]. In addition, Situ-Loewenstein et al. [16] synthesized Fe_3O_4 nanocubes and nanospheres by a thermal decomposition method. Fe_3O_4 nanocubes exhibited much higher r_2 relaxivity value (862.2 $mM^{-1}s^{-1}$) than nanospheres (147.5 $mM^{-1}s^{-1}$), which makes Fe_3O_4 nanocubes an excellent contrast agent for magnetic resonance (MR) imaging technique.

Catalytic properties also highly depend on the size and morphology of metal oxide nanoparticles. Nanoparticles with different size and morphology have different surface area, and the concentration of structural and chemical defects on the surface are also different, which significantly affects the catalytic performance of metal oxide nanoparticles. For example, CeO_2 nanoparticles have been widely used as catalyst, and its catalytic performance significantly depends on the surface area, oxygen vacancy and Ce^{3+} reactive site on the surface, which related to the size and morphology of CeO_2 nanoparticles. In addition, Fisher et al. [17] synthesized CeO_2 nanocubes, nanorods and nanooctahedra through a microwave-assisted hydrothermal method; the catalytic performance for decomposition of H_2O_2 was investigated. It was found that CeO_2 nanorods had the highest catalytic activity followed by nanocubes and nanooctahedra. By characterizing different ceria nanoparticles through Raman spectra and X-ray photoelectron spectroscopy, CeO_2 nanorods was found to have the highest concentration of oxygen vacancies and Ce^{3+} reactive sites on the surface, which explains their excellent catalytic properties. Alhumaimess et al. [18] and He et al. [19] studied the catalytic performance of CeO_2 nanocubes, nanorods and nanowires for CO oxidation and olefins oxidation. Due to the larger surface area and higher Ce^{3+} concentration on the surface of CeO_2 nanoparticles, CeO_2 nanorods and nanowires showed much better catalytic activity than nanocubes in terms of CO and olefins oxidation.

Furthermore, in order to investigate the underlying mechanism of size-catalytic dependence of CeO_2 nanocubes, Hao et al. [20] studied the Ce valence state distribution and lattice expansion of CeO_2 nanocubes with different sizes (5 nm and 12 nm) and found lattice expansion happened when the size of CeO_2 nanocube decreased from 12 nm to 5 nm, as shown in Figure 1. Due to the lattice expansion of small nanocubes, the formation energy of oxygen vacancies decreases, which leads to the high concentration of oxygen vacancies and Ce^{3+} cations. In contrast, for large nanocubes, Ce^{3+} cations mainly existed in the surface layers. However, for small nanocubes, Ce^{3+} cations also existed in the center layers, as shown in Figure 2. Because of the high concentration of oxygen vacancies and Ce^{3+} cations, small CeO_2 nanocubes have more reactive sites for catalytic performance. In addition, target molecules can easily diffuse into the small nanocubes, due to the large interplanar distance, which also improves the catalytic performance.

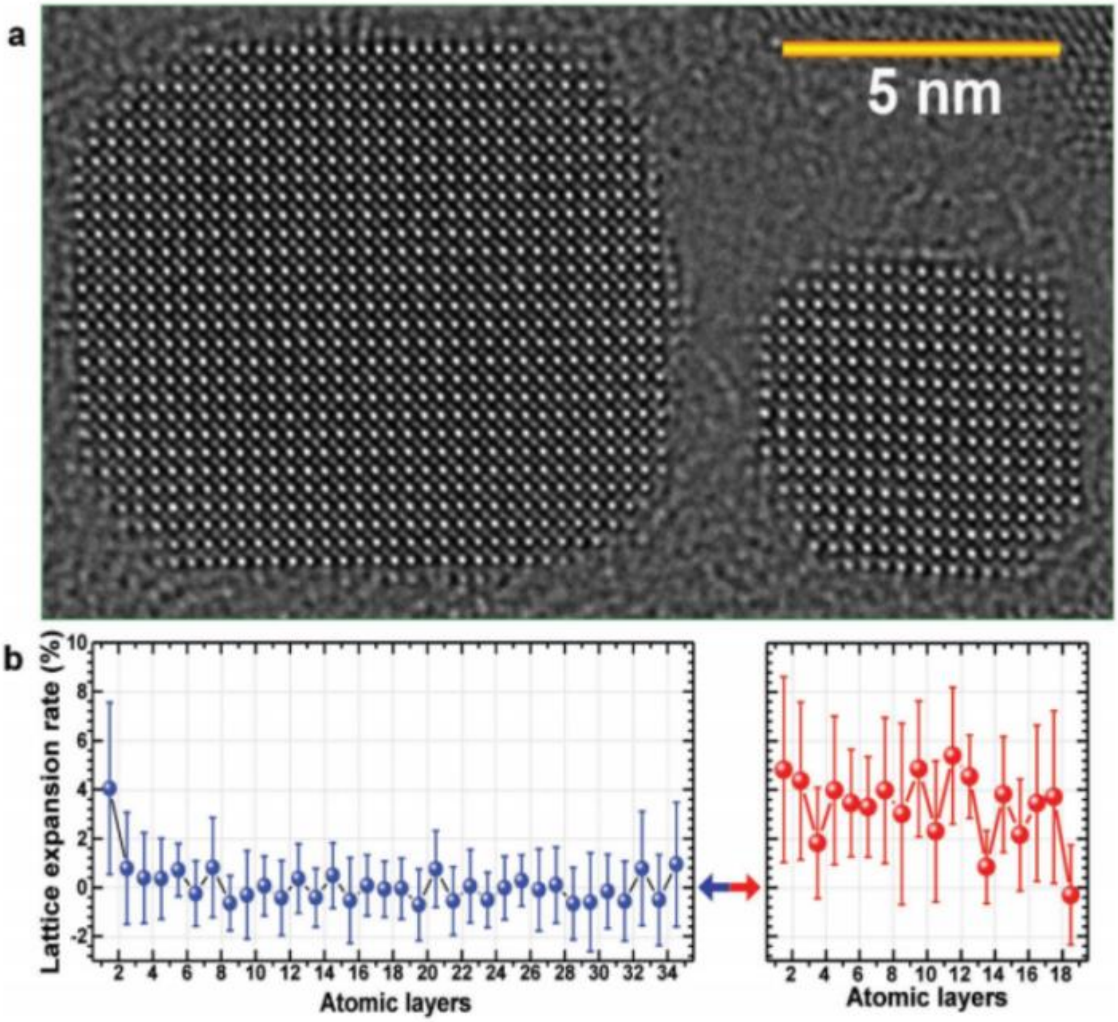

Figure 1: [20] Atomic-scale analysis of 5 and 12 nm CeO_2 Nanocubes. (a) aberration-corrected TEM images of CeO_2 Nanocubes. (b) The lattice expansion rate of CeO_2 Nanocubes (blue line: nearly no lattice expansion for 12 nm CeO_2 Nanocubes; red line: large lattice expansion for 5 nm CeO_2 Nanocubes).

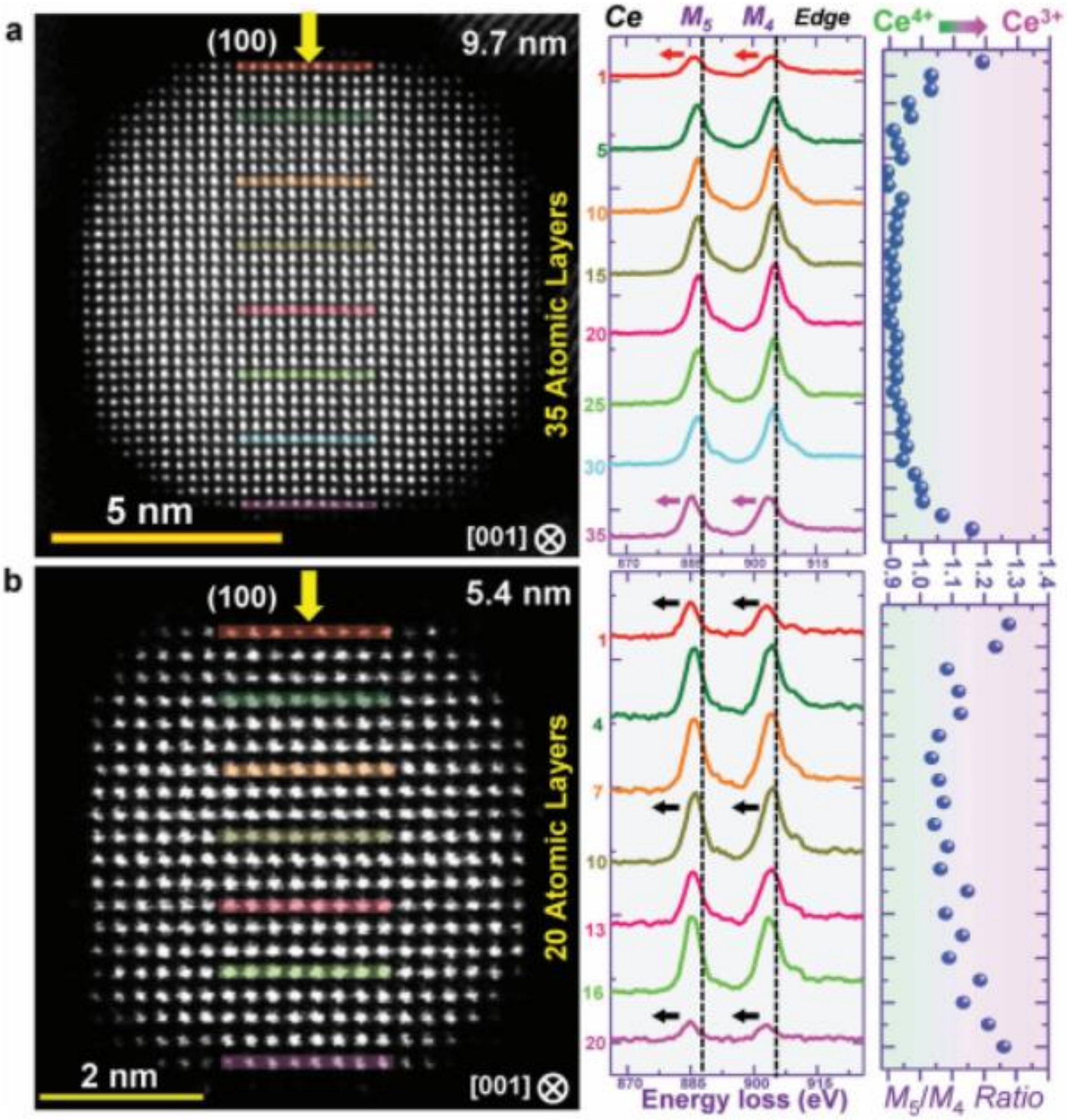

Figure 2: [20] STEM-EELS detection of Ce valence state distribution inside 5 nm and 12 nm CeO_2 nanocubes.

In_2O_3 and Cu_2O nanoparticles also used as catalysts for the degradation of hexamethyl pararosaniline chloride and the reduction of H_2O_2 [21], [22]. In_2O_3 nanocubes have excellent photocatalytic activity in terms of the degradation of hexamethyl pararosaniline chloride (the degradation rate is 93.6% after 14h irradiation) [21]. By using the cyclic voltammograms (CVs) and nitrogen sorption isotherm test, Meng et al. [22] found the Cu_2O nanocubes with smaller size have a much better catalytic activity for the reduction of H_2O_2, due to the larger surface area which provides more reactive sites for the reduction of H_2O_2.

Electrochemical and biochemical properties also depend on the size and morphology of metal oxide nanoparticles. Chavhan et al. [23] synthesized CeO_2 nanocubes through a urea-assisted hydrothermal method. By using CeO_2 nanocubes as electrode materials, they found the electrochemical properties of CeO_2 nanocube based supercapacitor significantly depended on the size of CeO_2 nanocubes. With increasing the size from 7 nm to 18 nm, electrode capacitance (maximum: 122.85 F/g at 5mV/s and 88.71 F/g at 5 A/g) and specific capacity (maximum: 28 C/g at 1 A/g) increased accordingly. In addition, the CeO_2 electrode showed the excellent cyclic stability (96.24 % capacitance remaining after 1000 cycles). Lyu et al. [24] also studied the biochemical performance of CeO_2 nanocubes used as an antioxidant to protect the β-cell. From catalase mimetic activity assay, they found CeO_2 nanocubes can protect INS-1 cells from H_2O_2-induced oxidative stress. In addition, CeO_2 nanocubes with smaller size exhibited much better antioxidant and anti-apoptotic effects.

2. CUBIC MORPHOLOGY OF METAL OXIDE NANOPARTICLES

According to the morphology-property relationship discussed above as well as by other studies [25]–[27], among the different morphology (such as nanorod, nanowire, nanosphere, nanocube and nanooctahedra), nanocubes possess much better electrical, optical, magnetic, biomedical and gas sensing properties. For example, for equal volume, nanocube has larger surface area than other morphologies, which is beneficial for fabrication of nanocube-polymer nanocomposite materials with excellent electric properties. Parizi et al. [28] fabricated this kind of nanocomposite capacitor by using $BaTiO_3$ nanocubes and poly(vinylidene fluoride-co-hexafluoropropene) (P(VDF-HFP)) as building blocks. Because of the large surface-to-volume ratio of nanocube compared with other morphologies, the contact interface between nanocubes or between nanocubes and polymer matrix increased which resulted in the better electrical properties. As a result, the synthesized $BaTiO_3$/P(VDF-HFP) film showed good dielectric and excellent electrical property (high permittivity: $\varepsilon = 21$; high energy density: $E = 4.66$ J/cm^3 at 150 MV/m). The reason was ascribed to the large contact interface, which significantly restricted the movement of the molecular dipoles, leading to the decrease of dipole relaxation.

In addition, the large contact interface facilitates the ion or electron transportation at the interfacial region, which results in improved electrochemical properties. In particular, Yang et al. [29] studied the electrochemical performance of $CoFe_2O_4$/graphene composite used as anodes in lithium-ion battery. By using cyclic voltammetry (CV), they found $CoFe_2O_4$/graphene composite anode showed an excellent cyclic performance (1109 mA h g^{-1} after 100 cycles at 0.2 A g^{-1}) and enhanced rate capability (420 mA h g^{-1} at 5 A g^{-1}). In addition, Zhang et al. [30] studied the electrochemical performance of $NiFe_2O_4$/reduced graphene oxide (rGO) electrode used in the solid-state supercapacitor. The electrochemical properties were measured by using cyclic voltammetry (CV), galvanostatic charge-discharge (GCD) and electrochemical impedance spectroscopy (EIS). From the characterization results, $NiFe_2O_4$/rGO electrode exhibited excellent specific capacity (488 F g^{-1} at 1A g^{-1}), rate ability (89.8 % of its initial capacitance was remained at 8 A g^{-1}) and long cycle life (89.8 % of its initial capacitance was remained after 10000 cycles).

Besides the enhanced interfacial properties, nanocubes can easily self-assemble and form a closed-packed and ordered assembly because of the size uniformity compared with other morphologies, which is important for energy storage, electric as well as for catalysis applications [31]–[34]. Caruntu et al. [35] synthesized $BaTiO_3$ nanocubes through solvothermal method. By using the obtained $BaTiO_3$ nanocubes as building blocks, simple cubic superlattice and body-centered superlattice were fabricated, as shown in Figure 3 and Figure 4, respectively. The formation of different superlattice was due to the type of solvent used to disperse $BaTiO_3$ nanocubes. When toluene was used, simple cubic superlattice was formed (see Figure 3). Body-centered superlattice was produced by using hexane as a solvent (see Figure 4). The reason behind the formation of simple cubic superlattice was due to the face-to-face attachment of each nanocube along the same orientation (they attached to each other through (001) facets). The size-uniformity of $BaTiO_3$ nanocubes was another reason for the formation of simple cubic superlattice. As for the body-centered superlattice, the formation mechanism was due to the charge transformation between $BaTiO_3$ nanocubes and oleic acid molecules, which introduced the Coulomb force and reconstructed the arrangement of $BaTiO_3$ nanocubes [35].

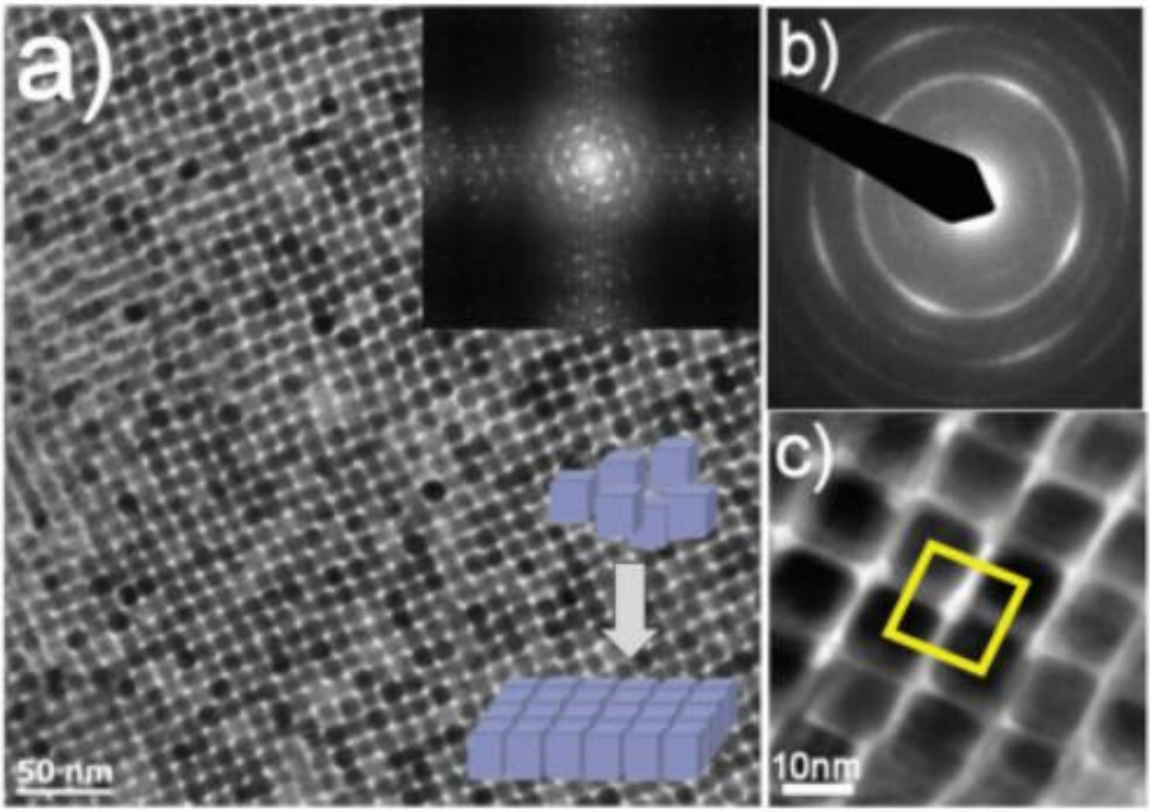

Figure 3: [35] TEM image (a), HRTEM image (c) and selected area electron diffraction pattern (SAED, b) of simple cubic superlattice of $BaTiO_3$ nanocubes.

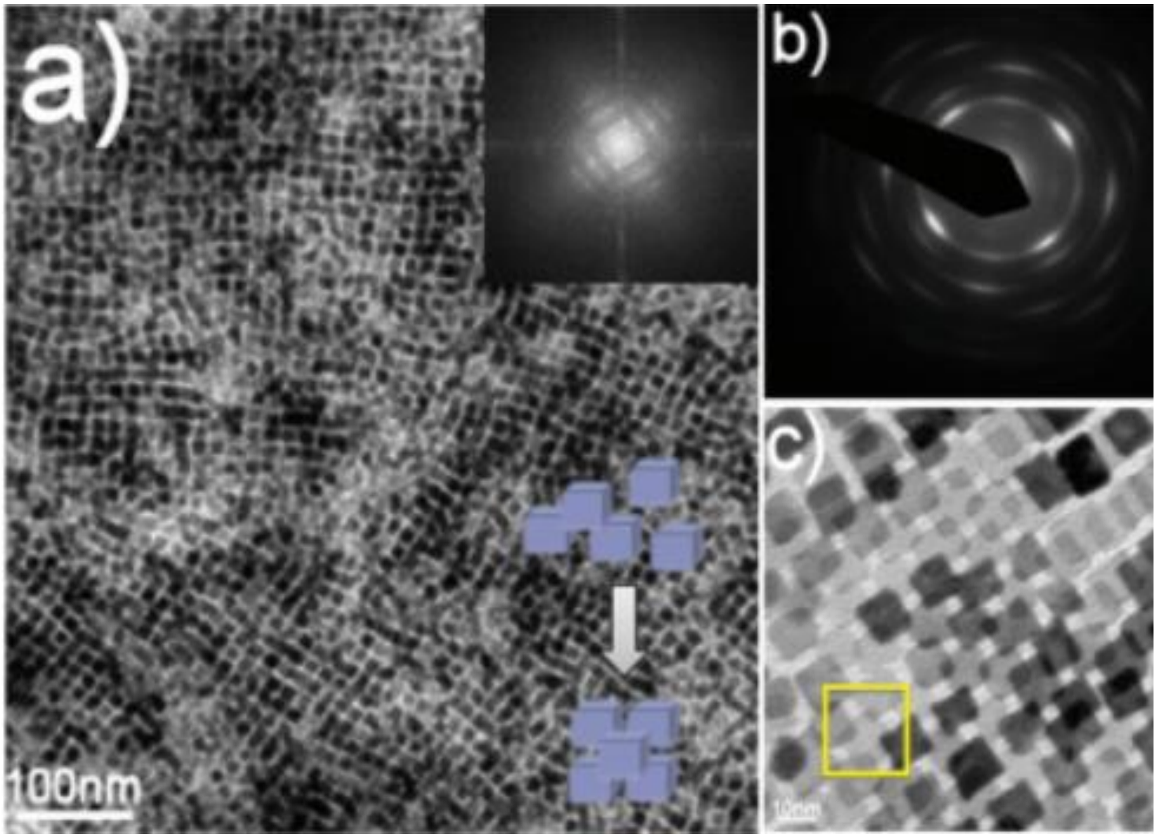

Figure 4: [35] TEM image (a), HRTEM image (c) and selected area electron diffraction pattern (SAED, b) of body-centered superlattice of $BaTiO_3$ nanocubes.

Furthermore, Yang et al. [11] synthesized Fe_3O_4 nanoparticles through a one-pot synthesis method. The convective assembly technique was used to produce superlattice by using Fe_3O_4 nanocubes and Fe_3O_4 nanospheres as building blocks. From the XRD results, the intensity of (220) peak was higher than (311) peak in the superlattice fabricated by using Fe_3O_4 nanocubes. However, in the superlattice fabricated by using Fe_3O_4 nanospheres, the intensity of (311) peak was much higher than (200) peak. This result indicated that the shape of the building block affected the texture of the superlattice.

3. CONTROLLED SYNTHESIS AND FORMATION MECHANISMS OF METAL OXIDE NANOCUBES

Based on the above discussion (size-property relationship, morphology-property relationship and excellent properties that nanocubes possess compared with other morphologies), in order to get metal oxide nanoparticles with cubic morphology, it is important to investigate the factors that will affect the size and morphology of metal oxide nanoparticles during the synthesis process. In addition, a better understanding on the formation mechanism of metal oxide nanocubes can also help to modify the synthesis process, which leads to the formation of uniformed nanocubes.

There have been many studies focusing on the formation mechanisms of metal oxide nanocubes (such as growth kinetics of different crystal planes, in situ growth mechanism, dissolution-precipitation mechanism, dissolution-recrystallization mechanism and oriented attachment mechanism) and the factors that will affect the formation of cubic morphology (such as capping agent or surfactant, the concentration and type of precursors, the type of solvents, reaction time, reaction temperature, reaction atmosphere, heating rate, reflux time and dopant) [12], [23], [24], [36]–[39].

Kato et al. [40], [41] synthesized $BaTiO_3$ nanocubes through hydrothermal method by using $Ba(OH)_2$ and bis(ammonium lactate) titanium dihydroxide (TALH) as barium and titanium precursor. Oleic acid and tert-butylamine worked as capping agent and stabilizer. By changing the concentration of $Ba(OH)_2$ and TALH, nanocubes with different sizes were obtained (as shown in Figure 5). From Figure 5, with decreasing the concentration of $Ba(OH)_2$ and TALH from 0.1 M to 0.025 M, the corresponding size of nanocubes increased from 15 nm to 30 nm. The size variation was due to the competition between nucleation and crystal growth processes. When the concentration of $Ba(OH)_2$ and TALH was high, the nucleation process dominated, which resulted in the small nuclei. Small nanocubes were formed by the further crystal growth of small nuclei. When the concentration of $Ba(OH)_2$ and TALH was low, the crystal growth process dominated, therefore, relatively large nuclei were formed, which leaded to larger nanocubes.

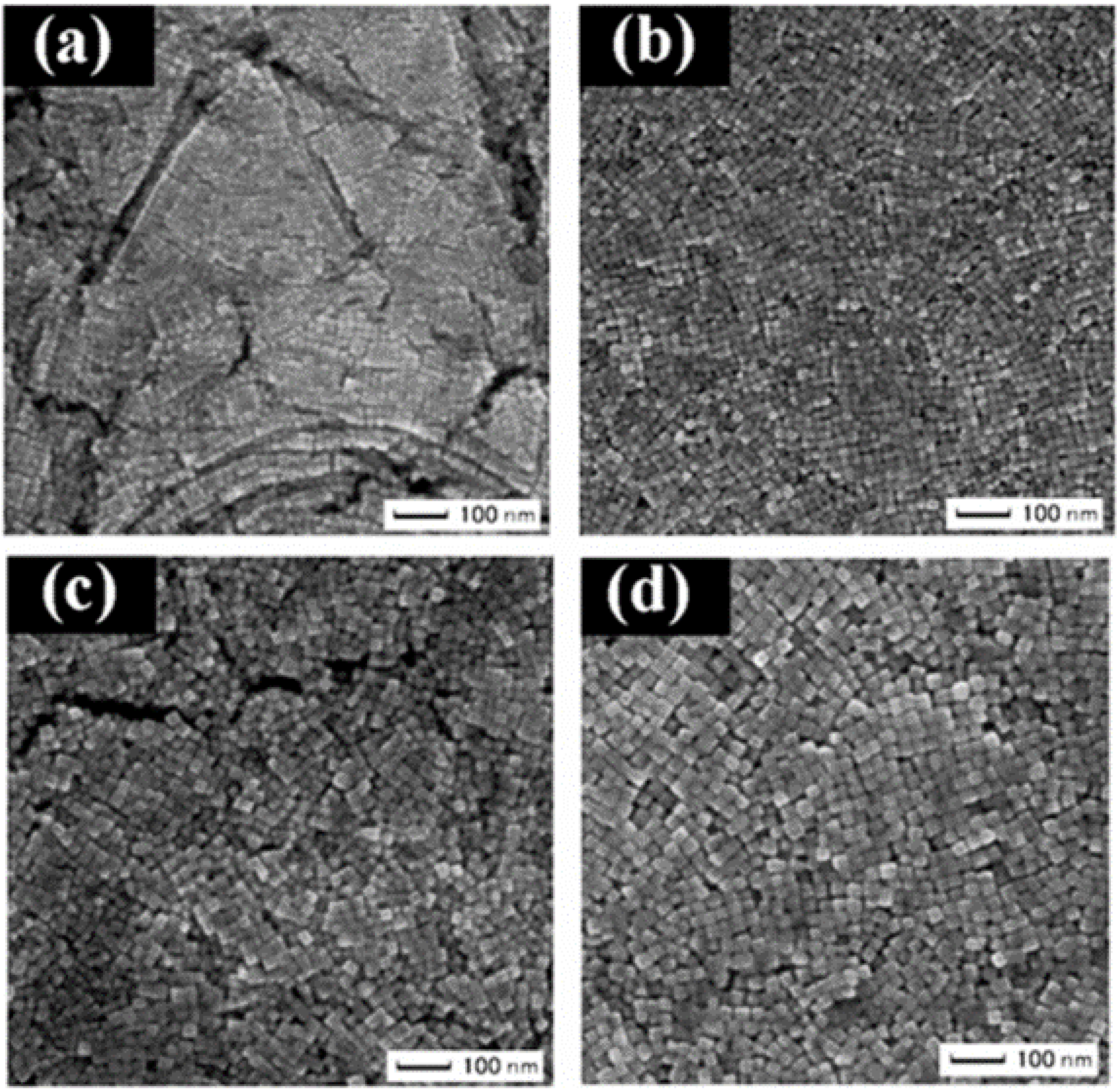

Figure 5: [41] SEM images of $BaTiO_3$ nanocubes synthesized by varying the concentrations of $Ba(OH)_2$ and TALH. (a): 0.1 M; (b): 0.05 M; (c): 0.03 M; (d): 0.025 M.

Kato et al. also discussed the formation mechanism of $BaTiO_3$ nanocubes and the factors that affected the size and shape of $BaTiO_3$ nanocubes. In order to study the formation mechanism, the reaction time changed from 4 h to 48 h. At early stage of the reaction (4h), no nanocubes were formed. With prolonging the reaction time, more and more nanocubes were formed directly from Ti-based hydrous gel. Therefore, in situ growth mechanism was proposed, as shown in Figure 6. Specifically, when TALH is added into $Ba(OH)_2$, the hydrolysis process of TALH began. By condensation, titanium octahedra connected with each other through vertex point. Then, barium species were incorporated into this titanium-based structure to form $BaTiO_3$ crystal structure.

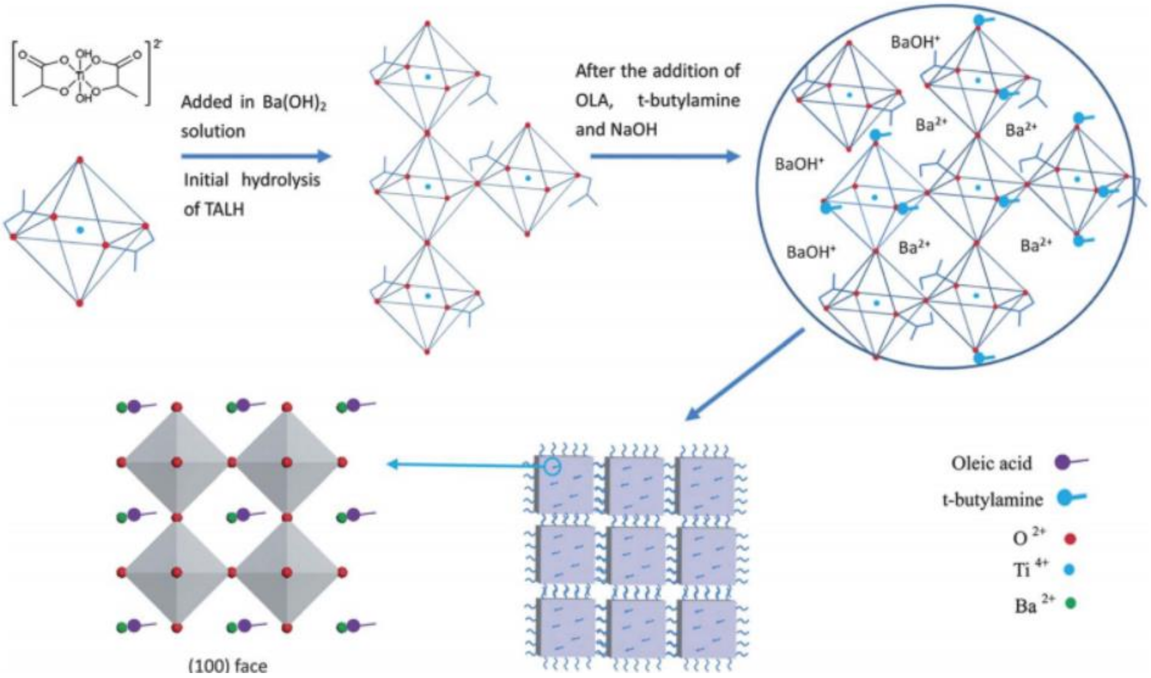

Figure 6: [40] In situ growth mechanism of $BaTiO_3$ nanocubes.

The final formation of cubic morphology was due to the different growth rate of crystal planes, which is related to the surface energy of the crystal planes (Gibbs-Curie-Wulff theory) [42]. {100} crystal planes have the lowest surface energy, which results in the slowest growth of {100} crystal planes. In contrast, for crystal planes with high surface energy, the growth rate is high. Crystal planes with high growth rate will completely grow out and, finally, be restricted by the crystal planes with low growth rate, which results in the disappearance of crystal planes with high growth rate in the final morphology. Therefore, the cubic morphology with six exposed {100} crystal planes is obtained. Oleic acid and tert-butylamine, working as capping agent and stabilizer, respectively, also played important roles in formation $BaTiO_3$ nanocubes. Specifically, oleic acid selectively attached to {100} crystal planes, which stabilized the cubic morphology. In addition, ordered assembly based on $BaTiO_3$ nanocubes was also formed. This phenomenon was due to the interaction between the oleic acid molecules. Oleic acid molecules were adsorbed on the surfaces of $BaTiO_3$ nanocubes, and hydrophobic and van der Waals forces between nanocubes facilitated the formation of ordered assembly. Tert-butylamine in its turn not only stabilized the hydroxyl groups of titanium octahedra, but also facilitated the formation of $BaTiO_3$ nanocubes.

Furthermore, Sun et al. [43], Vara et al. [44] and Huango et al. [45] investigated a different formation mechanism (dissolution-precipitation mechanism, also known as Oswald ripening mechanism) and the influence of different reaction conditions (such as morphology of titanium precursor and the concentration of NaOH as a solvent material) on the formation of $BaTiO_3$ nanocubes. Sun et al. [43] synthesized $BaTiO_3$ nanocubes through a thermo-hydrolysis route. Oleic acid and hydrazine were used as capping agents, while NaOH solution worked as solvent. The concentration of NaOH and the molar ratio of oleic acid to hydrazine affected the corresponding morphology of $BaTiO_3$ nanoparticles. By increasing the concentration of NaOH from 1 to 2 mol L^{-1}, the morphology of $BaTiO_3$ nanoparticles changed from nanocube to polyhedron mixed with nanocube with round edges, and finally nanosphere. By increasing the amount of hydrazine, the nanoparticles changed from irregular shape to cubic morphology. By adding hydrazine, the formation mechanism changed from in situ formation mechanism to dissolution-precipitation mechanism. Hydrazine can also facilitate the dissolution process of titanium monomers and the formation of $BaTiO_3$ phase. The new $BaTiO_3$ phase will precipitate on the already existed larger $BaTiO_3$ nanoparticles.

Vara et al. [44] further illustrated the dissolution-precipitation mechanism by synthesizing $BaTiO_3$ nanocubes through a solvothermal method with oleic acid used as capping agent. Figure 7 shows the formation process of $BaTiO_3$ nanocubes. At the beginning of reaction, titanium precursor (TiO_2) dissolved and formed titanium hydroxide. At the same time, barium precursor also dissolved and reacted with titanium hydroxide to form small $BaTiO_3$ nanoparticles. With reaction proceeding, newly generated $BaTiO_3$ nanoparticles precipitated on the existing $BaTiO_3$ nanoparticles to form larger particles. With the help of oleic acid, cubic morphology can be obtained. Oleic acid molecules adsorbed on the {100} crystal planes and restrict the growth of these crystal planes. Combining the fast crystal growth along <111> direction, {111} crystal planes finally disappeared and left the nanoparticle with cubic morphology and exposed {100} facets.

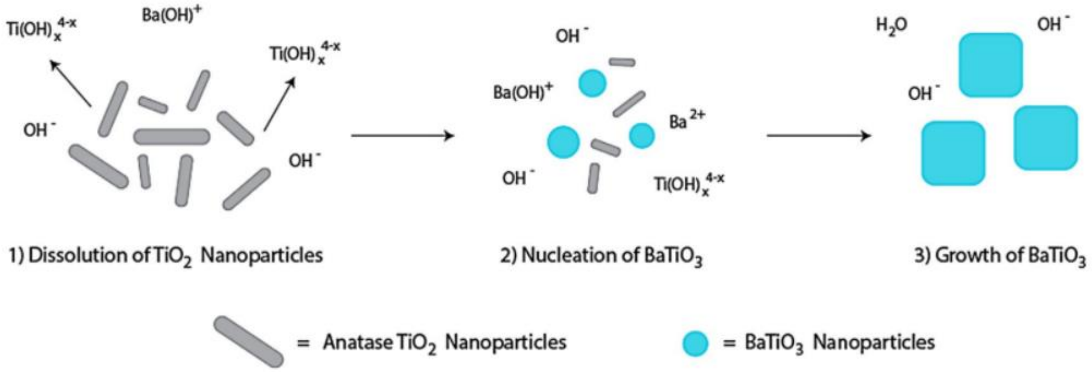

Figure 7: [44] Dissolution-precipitation formation mechanism of $BaTiO_3$ nanocubes.

Huango et al. [45] synthesized $BaTiO_3$ nanoparticles by using a molten-salt method. BaO, $BaCO_3$ and TiO_2 were used as precursors. They found the morphology of $BaTiO_3$ nanoparticles depended on the morphology of TiO_2 precursor and the relative dissolution rate of BaO and $BaCO_3$ precursors. When using rod-shape and sphere-shape TiO_2 precursors, the final products had rod shape and sphere shape accordingly. By using BaO and $BaCO_3$ as precursors, nanocubes and nanorods were formed accordingly. The mechanism of the corresponding $BaTiO_3$ nanoparticles formation is dissolution-precipitation formation mechanism. However, the final shape depends on the dissolution rate of the barium precursors. In the case of BaO used as precursor, the dissolution rate was slower than for titanium precursor. As a result, the titanium rod broke up and formed small grains, while the barium precursor dissolved and reacted with titanium precursor to form nanocubes. However, in the case of $BaCO_3$ used as precursor, the dissolution rate of $BaCO_3$ was much faster than titanium precursor. Therefore, the $BaCO_3$ first dissolved and attached to the surface of titanium precursor to form a shell, and the barium ions diffused into the titanium precursor. Finally, the $BaTiO_3$ was produced and the rod shape can be preserved.

In addition, Adireddy et al. [46] synthesized $BaTiO_3$ nanocubes through solvothermal method. The effect of reaction atmosphere on the morphology of $BaTiO_3$ nanoparticles was discussed. When the reaction was under open atmosphere, the final product was a mixture of nanocubes and nanospheres. But when the reaction was under inert atmosphere, $BaTiO_3$ nanocubes were formed.

Souza et al. [47] synthesized $SrTiO_3$ nanocubes through microwave-assisted hydrothermal method. Based on the SEM images (shown in Figure 8), the formation of $SrTiO_3$ nanocubes was confirmed and the nanocube formation process was investigated. When reaction time was 4 min (Figure 8(a)), small nanoparticles aggregated together to form the sphere-like particles. When reaction time was 10 min (Figure 8(b)), sharp edges appeared and cubic morphology started to form. After increasing reaction time to 20 min, perfect nanocubes were formed (see Figure 8(c)). A new morphology (dodecahedron) was formed after 40 min reaction (see Figure 8(d) and 8(e)). This was due to the instability of solution induced by microwave. However, most of the $SrTiO_3$ nanoparticles were still in cubic morphology. Further increasing the reaction time to 80 min, some small nanocubes started to aggregate on the surfaces of existing large nanocubes (see Figure 8(f)). Finally, nanorods were formed by continuing aggregation of small nanocubes after 160 min (see Figure 8(g)). Three mechanisms were used to explain the formation of $SrTiO_3$ nanocubes. (1) The small $SrTiO_3$ nanoparticles were formed by the reconstruction and grain growth of octahedra (TiO_6) and cuboctahedra (SrO_{12}) clusters. (2) From thermodynamic point view, in order to minimize the overall surface energy, small $SrTiO_3$ nanoparticles will aggregate together to form lager nanoparticles. (3) From Wulff rule, the final shape depends on the growth rate of different crystal planes with different surface energy. Crystal planes with high surface energy, in this case {111} planes, will grow rapidly, which results in the small surface or complete disappearance. Crystal planes with low surface energy grow slowly, which leads to the formation of $SrTiO_3$ nanocubes with exposed {100} facets.

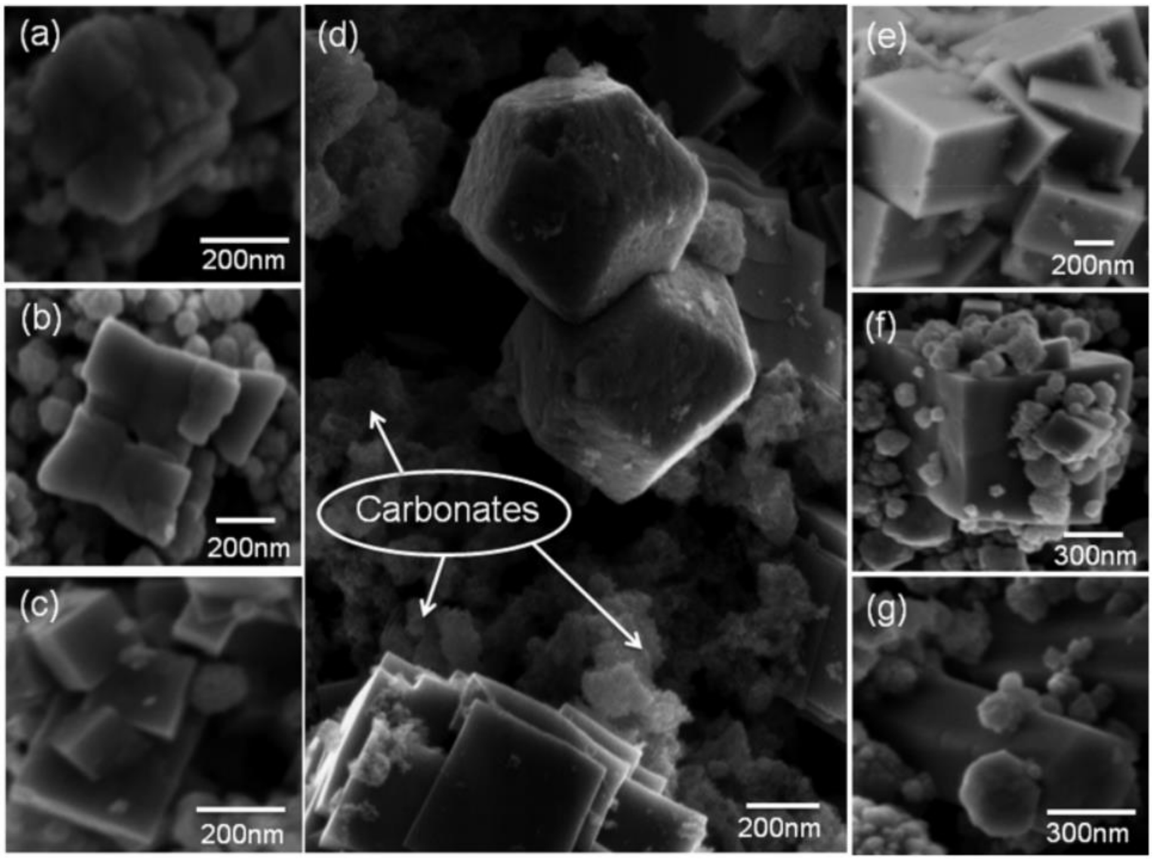

Figure 8: [47] SEM images of $SrTiO_3$ nanoparticles at different synthesis time. (a) 4 min; (b) 10 min; (c) 20 min; (d, e) 40 min; (f) 80 min; (g) 160 min.

Muro-Cruces et al. [48] synthesized Fe_3O_4 nanocubes by thermally decomposing iron acetylacetonate precursor. By changing the amount of iron acetylacetonate precursor from 0.400 to 0.690 g, reaction temperature from 25 ℃ to 100 ℃ and heating rate from 3 ℃/min to 20 ℃/min, Fe_3O_4 nanoparticles with different morphologies and sizes were formed (as shown on Figure 9). As shown on Figure 9(a) – 9(e), when the amount of iron acetylacetonate was lower than 0.420 g,

Fe_3O_4 nanoparticles had irregular shape. When the amount of iron acetylacetonate was higher than 0.610 g, Fe_3O_4 nanoparticles changed to octahedra. When the amount of iron acetylacetonate was within the range of 0.420 – 0.610 g, Fe_3O_4 nanocubes were formed. Generally, as summarized on Figure 9(f), the size of Fe_3O_4 nanocubes increased with increasing the amount of iron acetylacetonate. On the other hand, by increasing reaction temperature from 25 ℃ to 100 ℃, the size of Fe_3O_4 nanocubes decreased from 23.7 nm to 11.8 nm (see Figure 9(g) – 9(i)). In addition, by increasing the total concentration of iron acetylacetonate precursor while applying a higher heating rate, Fe_3O_4 nanocubes with a larger size were produced (52.6 nm, see Figure 9(k), and 80 nm, see figure 9(l)).

Another formation mechanism of producing cubic morphology of metal oxide nanoparticles was discussed in Muro-Cruces et al.'s research on synthesis and characterization of Fe_3O_4 nanoparticles. The final shape of Fe_3O_4 nanoparticles was controlled by two factors: The chemical potential of the monomers and the chemical potential of the crystal planes [49]. In the case of Fe_3O_4 nanoparticles, {111} crystal planes have the lowest chemical potential, and {100} crystal planes have the highest chemical potential ($\mu\{100\} > \mu\{110\} > \mu\{111\}$). As a result, at the beginning of the reaction, monomers start to form and accumulate. As soon as the chemical potential of the monomers (μm) is higher than any of the crystal planes ($\mu m > \mu\{100\} > \mu\{110\} > \mu\{111\}$), the monomers can attach to those three crystal planes, which leads to the growth of {111}, {110} and {100} crystal planes. The only difference in this stage is the growth rate of those crystal planes is different. Because of the high energy barrier of {111} crystal planes, the growth rate of {111} crystal planes is the smallest, therefore, the octahedral morphology is formed. With the reaction proceeding, the chemical potential of the monomers decreases ($\mu\{100\} > \mu m > \mu\{110\} > \mu\{111\}$), therefore, the growth of {100} crystal planes stops and other crystal planes continue growing, which leads to the formation of tetradecahedron. With prolonging the reaction time and consuming the monomers, the chemical potential of the monomers keeps decreasing (μ{100} > μ{110} > μm > μ{111}). Finally, only {111} crystal planes can grow, and Fe_3O_4 nanocubes are formed. Figure 10 [48] shows the formation mechanism of Fe_3O_4 nanocubes.

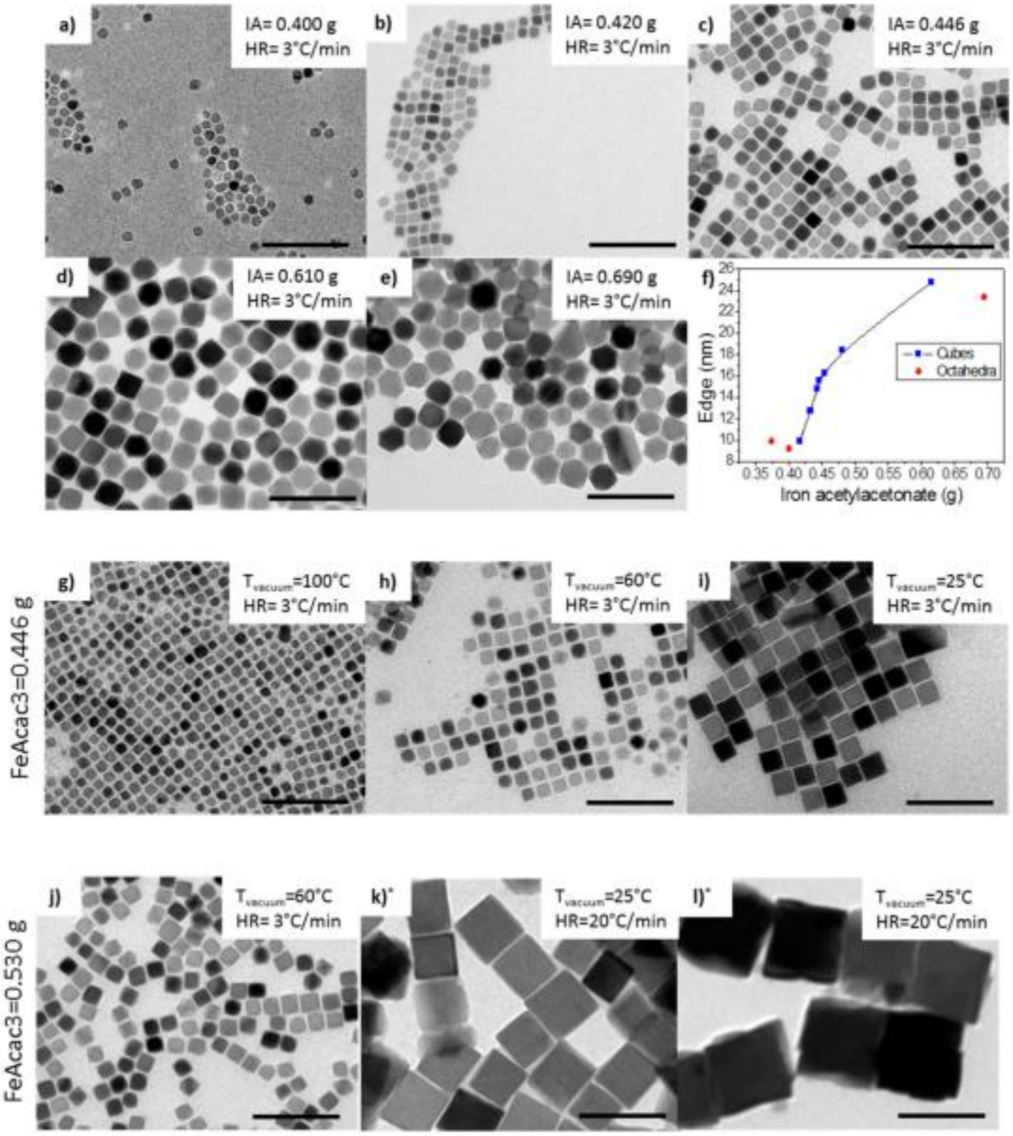

Figure 9: [48] TEM images of Fe_3O_4 nanoparticles synthesized at different reaction conditions. (a – e): change the amount of iron acetylacetonate; (g - i): change the reaction temperature; (j - l) change the heating rate.

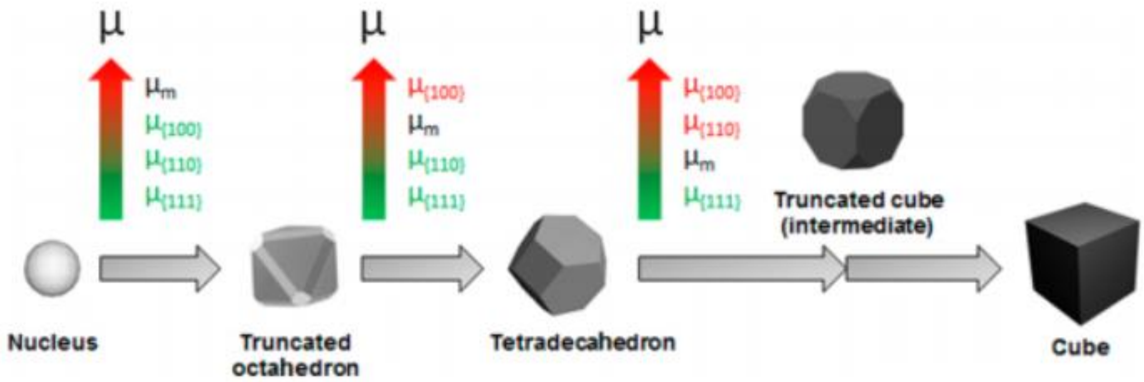

Figure 10: Formation mechanism of Fe_3O_4 nanocubes.

A new formation mechanism (stepwise oriented attachment mechanism) of Co_3O_4 nanocubes was proposed in Tsukiyama et al.'s research. Tsukiyama et al. [50] synthesized Co_3O_4 nanocubes by using water-toluene two-phase solvothermal method. Oleic acid and tert-butylamine were used as capping agent. By changing the concentration of tert-butylamine, Co_3O_4 nanoparticles with different morphology and size were obtained. Figure 11 shows the TEM images of synthesized Co_3O_4 nanoparticles together with the selected area electron diffraction patterns and the size distribution of these Co_3O_4 nanocubes. Specifically, when the concentration of tert-butylamine is low (1.44 mmol), Co_3O_4 nanoparticles with irregular shape were synthesized (see Figure 11(a)), and the size of the nanoparticle is relatively small with a diameter of 3 - 8 nm (see Figure 11(c)). With gradually increasing the concentration of tert-butylamine from 2.88 mmol to 5.76 mmol, more and more nanocubes with larger size were formed (see Figure 11(d), (g) and (j)). In addition, the size distribution became narrow (see Figure 11(l)), which indicated the formation of uniformed Co_3O_4 nanocubes. Stepwise oriented attachment mechanism was used to explain the formation of Co_3O_4 nanocubes (as shown in Figure 12). When tert-butylamine is added into the water phase, the nucleation process is initiated at the water-toluene interface region. Then, the formed nuclei will diffuse into the toluene phase with oleic acid molecules on the surfaces. When an excessive amount of oleic acid is added, the oleic acid will restrict the growth of the nuclei, which leads to the formation of nanoparticles with irregular shape. When a suitable concentration of oleic acid is applied, small nanocubes were formed through direct oriented attachment. When only a small amount of oleic acid is added, small nanocubes will grow into larger nanocubes by further direct oriented attachment.

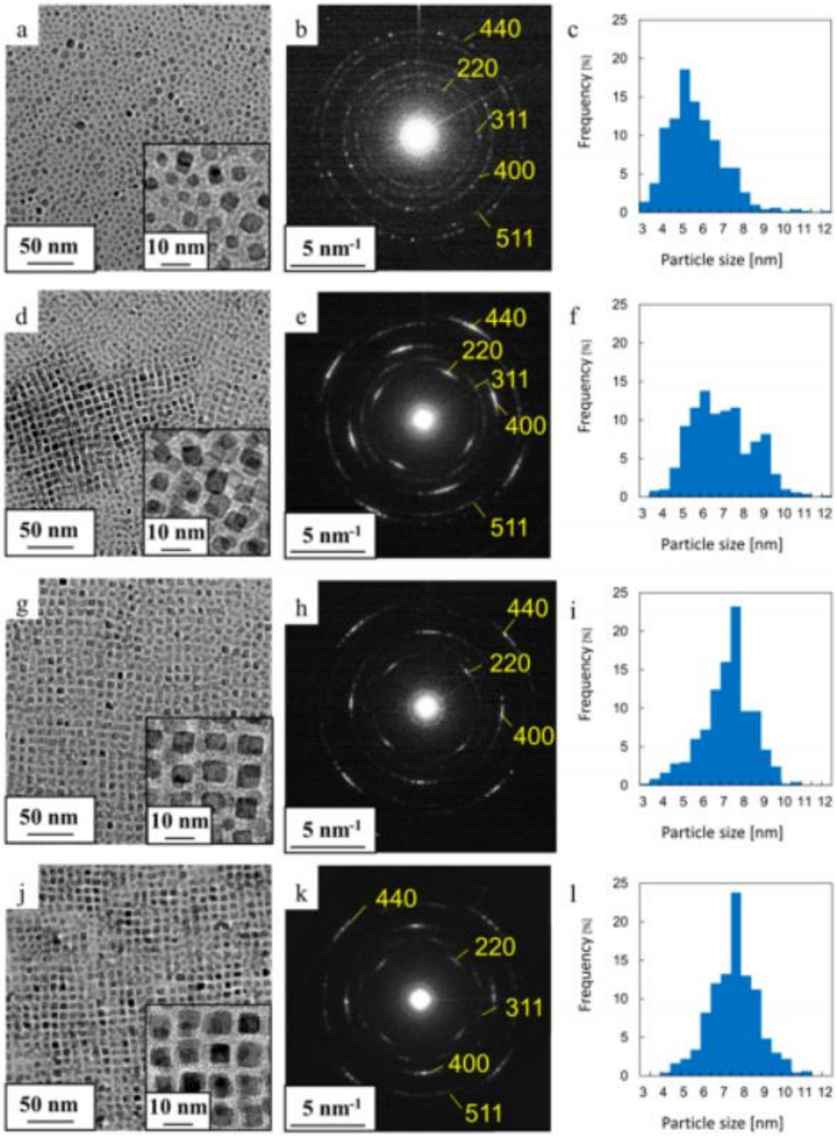

Figure 11: [50] TEM images (a, d, g, j) of Co_3O_4 nanocubes synthesized by changing the amount of tert-butylamine. (a) 1.44 mmol; (d) 2.88 mmol; (e) 4.32 mmol; (j) 5.76 mmol tert-butylamine; parts b, e, h and k show the corresponding selected area electron diffraction patterns and parts c, f, I and l show the size distribution of synthesized Co_3O_4 nanocubes.

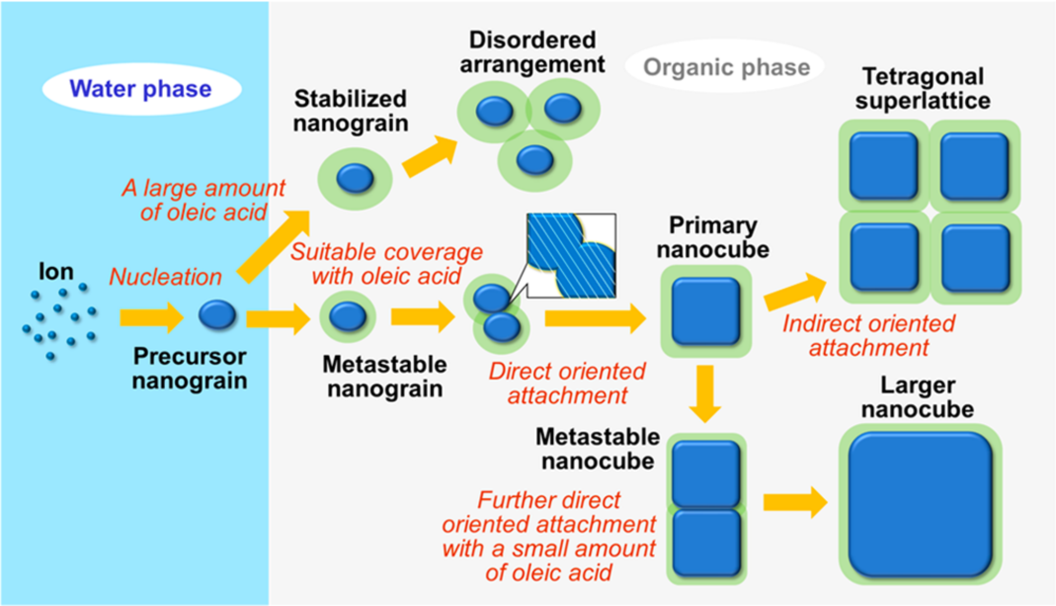

Figure 12: [50] Illustration of stepwise oriented attachment mechanism of Co_3O_4 nanocubes.

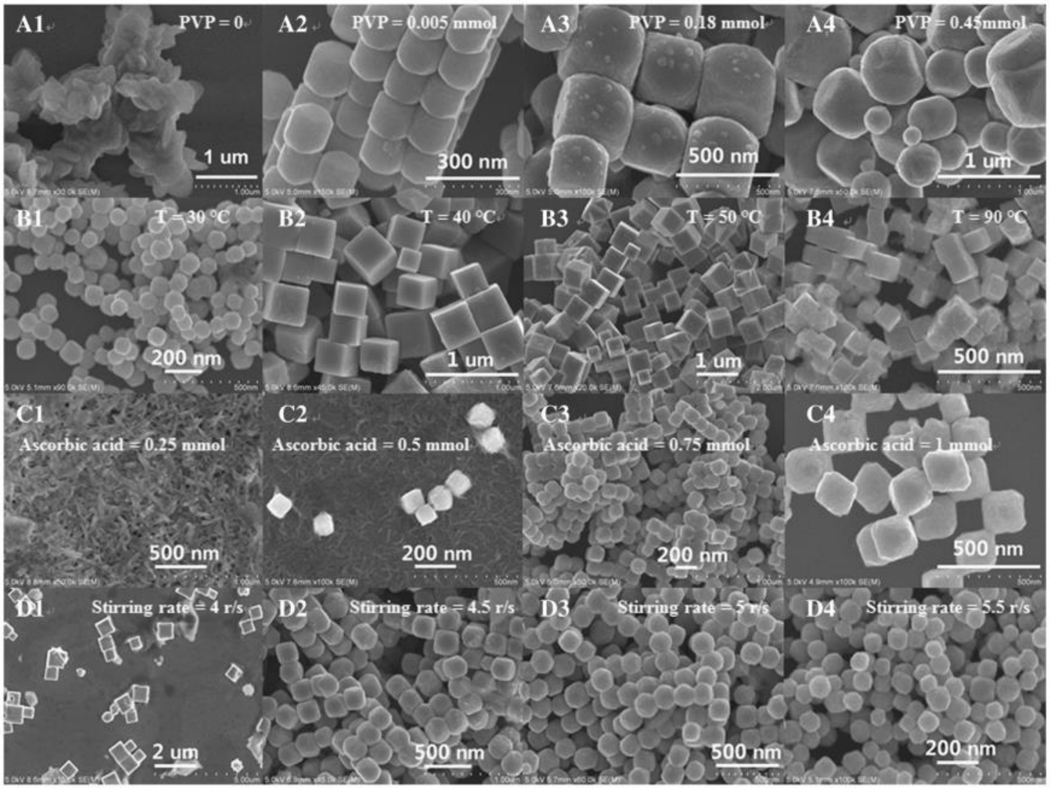

Figure 13: [51] SEM images of Cu_2O nanoparticles synthesized at different reaction conditions. A1 – A4: increase the amount of PVP surfactant from 0 to 0.45 mmol; B1 – B4: increase the rection temperature from 30 to 90 °C; C1 – C4: increase the amount of reducing agent (ascorbic acid:) from 0.25 to 1 mmol; D1 - D4: increase the stirring rate from 4 to 5.5 r/s.

Bai et al. [51] also systematically investigated the influence of reaction conditions (such as polyvinylpyrrolidone surfactant (PVP), reaction temperature, reducing agent (ascorbic acid: $C_6H_8O_6$) and stirring rate) on the size and morphology of Cu_2O nanoparticles. Figure 13 shows the SEM images of Cu_2O nanoparticles synthesized at different reaction conditions.

Specifically, Figure 13(A1) – 13(A4) showed the effect of surfactant. Without PVP surfactant, the Cu_2O nanoparticles had irregular shapes and were highly agglomerated (see Figure 13(A1)). In the presence of PVP surfactant, the cubic-like nanoparticles were formed. With increasing the amount of PVP surfactant, the size of Cu_2O nanocubes increased accordingly (see Figure 13(A2) – 13(A4)). The mechanism behind the formation of these nanocubes is that the PVP surfactant will selectively absorbed on {100} crystal planes which will restrict the growth of these planes along the <100> directions [52]. Crystal planes with high growth rate will grow rapidly and disappear at the end of the crystal growth process, which leads to the cubic morphology [53]. The mechanism behind the size variation of nanocubes summarized in Figure 13(A2) – 13(A4) is that the nucleation process will be hindered with increasing the amount of PVP surfactant. But the growth rate of the nanocubes will increase relatively, which leads to larger nanocubes [54].

Furthermore, Figure 13(B1) – 13(B4) show the effect of reaction temperature on the formation of Cu_2O nanoparticles. When the temperature is relatively low, truncated nanocubes with exposed {111} crystal planes in the corner were formed (see Figure 13(B1)), because this morphology is stable from thermodynamic point of view. With increasing the reaction temperature, the monomers diffuse more easily from the aqueous solution to the nuclei, which facilitates the growth rate along <111> directions (see Figure 13(B2) – 13(B4)). Finally, the perfect nanocubes were produced at highest temperature of 90 ℃ (see Figure 13(B4)). Next, Figure

13(C1) – 13(C4) show the effect of reducing agent (ascorbic acid) on the formation of Cu_2O nanoparticles. The reaction mechanism is shown as following [51]:

$$Cu(OH)_2 + C_6H_8O_6 \rightarrow Cu^{2+} + 2H_2O + C_6H_6O_6^{2-}$$

$$2Cu^{2+} + C_6H_6O_6^{2-} + H_2O \rightarrow Cu_2O + C_6H_6O_6 + 2H^+$$

Specifically, when the amount of reducing agent (ascorbic acid: $C_6H_8O_6$) is low, the amount of Cu^{2+} cations is not sufficient to continue the second reaction (see Figure 13(C1)). With increasing the amount of reducing agent, more and more Cu^{2+} cations were separated from $Cu(OH)_2$ and could be further reduced to form Cu_2O nanocubes (see Figure 13(C2) and (C3)). When the amount of reducing agent is very high (~ 1mmol), the nanocubes finally change to octahedron (see Figure 13(C4)).

Finally, Figure 13(D1) – 13(D4) show the effects of stirring rate on the formation of Cu_2O nanoparticles. A shown on these images, with increasing the stirring rate, the morphology of nanoparticles changes from nanocube to nanosphere. This phenomenon described by the fact that higher stirring rate makes it difficult for particles to aggregate and grow, e.g. the mechanical force makes the Cu_2O nanocubes hard to form. At the same time, the high stirring rate will introduce more oxygen into the solution which will decrease the effectiveness of the ascorbic acid, leading to less amount of Cu^{2+} cations to be further reduced to form Cu_2O nanoparticles [51].

More studies on the metal oxide nanoparticle formation were performed by Mateo et al. [55] and Bai et al. [56] where the effect of surfactant on the morphology of NiO nanoparticles was discussed. Mateo et al. [55] synthesized NiO nanoparticles through sol-gel method by using cetrimonium bromide (CTAB), polysorbate 80 (Tween 80) and sodium dodecyl sulfate (SDS) as surfactants. From SEM images, shown on Figure 14, the morphology of NiO nanoparticles significantly depends on the type of surfactants. Without surfactant, no nanoparticle was formed (see Figure 14(a)). By using cetrimonium bromide (CTAB) as surfactant, NiO nanocubes were formed (see Figure 14(b)). In the presence of polysorbate 80 (Tween 80), NiO nanospheres were synthesized (see Figure 14(c)), while, with sodium dodecyl sulfate (SDS), NiO nanorods were produced (see Figure 14(d)). Additionally, Figure 15 shows the interaction between surfactant molecules and Ni ions, which results in the different morphology of NiO nanospheres.

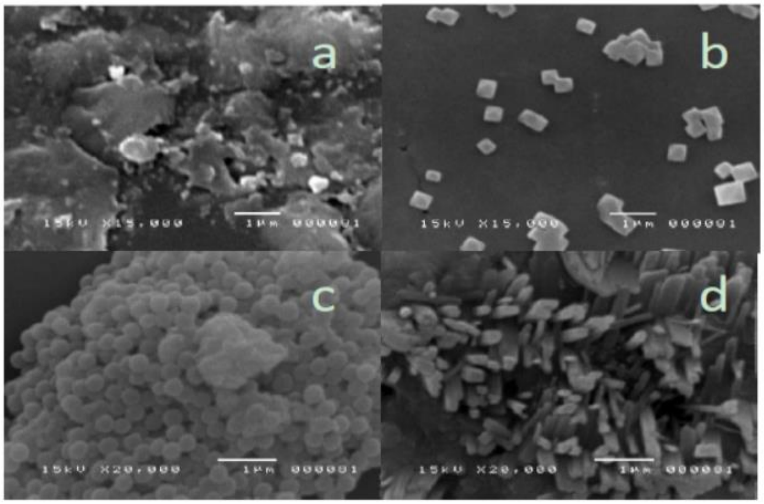

Figure 14: [55] SEM images of NiO nanoparticles synthesized without surfactant (a) and by using cetrimonium bromide (b), polysorbate 80 (c) and sodium dodecyl sulfate (d) as surfactants.

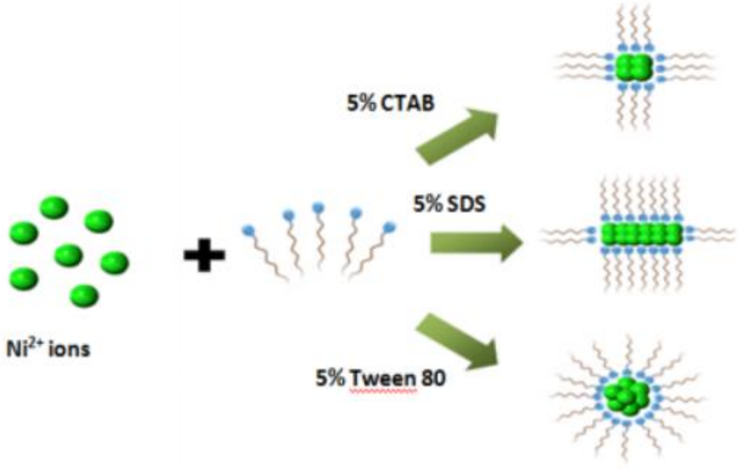

Figure 15: [55] Interaction between surfactant molecules and Ni ions.

Bai et al. [56] also synthesized NiO nanoparticles through microemulsion route by using sodium dodecyl sulfate (SDS) and cetrimonium bromide (CTAB) as surfactants. NiO nanocubes were synthesized by using SDS as surfactant, and NiO nanorods were formed in the presence of CTAB, which was completely different result compared to Mateo's experiment [55]. Therefore, more studies should focus on the effect of surfactant on the formation of NiO nanoparticles.

Elsayed et al. [15] and Situ-Loewenstein et al. [16] studied how the capping agent affect the formation of Fe_3O_4 nanocubes. Elsayed et al. [15] synthesized Fe_3O_4 nanoparticles through a β-amyrin and trimethylamine N-oxide assisted solvothermal method. In the presence and absence of β-amyrin, Fe_3O_4 nanocubes and Fe_3O_4 nanospheres were synthesized, respectively. In the presence of β-amyrin, the hydroxyl group of β-amyrin has a strong interaction with iron oxide, which results in the formation of hydrogen bonds with Fe_3O_4 nanoparticles. This further restricts the attachment of trimethylamine N-oxide to the {400} crystal planes. Therefore, {400} crystal planes grow much faster than other crystal planes, which leads to the formation of nanocubes. However, in the absence of β-amyrin, trimethylamine N-oxide can uniformly attach to {400}, {311}, {220} and {422} crystal planes, which results in the formation of nanospheres. Situ-Loewenstein et al. [16] also synthesized Fe_3O_4 concave nanocubes by a thermal decomposition method. The mixture of trioctylamine (TOA, a coordinating solvent) and 1-ocatadecence (ODE, a non-coordinating solvent) was used as solvent, while oleic acid worked as capping agent. By decreasing the molar ratio of trioctylamine to 1-ocatadecence, the morphology of Fe_3O_4 nanoparticles changed from concave nanocubes to nanospheres. This phenomenon is due to the selective binding of oleic acid (OA) and TOA (shown on Figure 16). When TOA was used as solvent, TOA will coordinate to iron atoms, which restricted the attachment of OA to {100} and {110} crystal planes. Therefore, OA can only attach to the {111} crystal planes. The growth of

{111} crystal planes is much faster than other crystal planes, which results in the formation of concave nanocubes. When gradually increasing the concentration of ODE, ODE will not coordinate to iron atoms. Therefore, OA will uniformly attach to {100}, {111} and {110} crystal planes, which results in the formation of nanospheres.

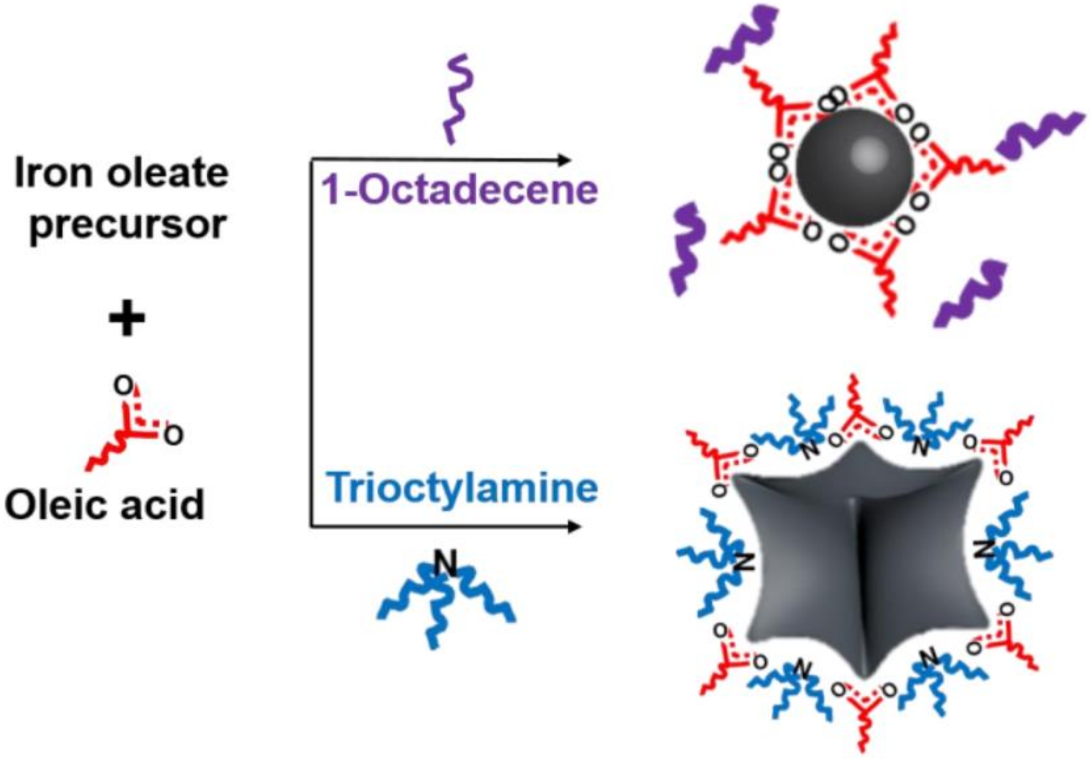

Figure 16: [16] Effects of Oleic acid (OA), trioctylamine (TOA) and 1-ocatadecence (ODE) on the morphology of Fe_3O_4 nanoparticles.

In addition, the capping agent can also be used to control the formation mechanism of metal oxide nanocubes. Specifically, Wu et al. [57] synthesized Fe_2O_3 nanocubes through a facile and rapid one-step solvothermal method by using oleic acid as capping agent and studied the corresponding formation mechanism of Fe_2O_3 nanocubes. In the presence and absence of oleic acid, Fe_2O_3 nanocubes were synthesized by following different formation mechanism (oriented attachment mechanism and Oswald ripening mechanism), as shown in Figure 17.

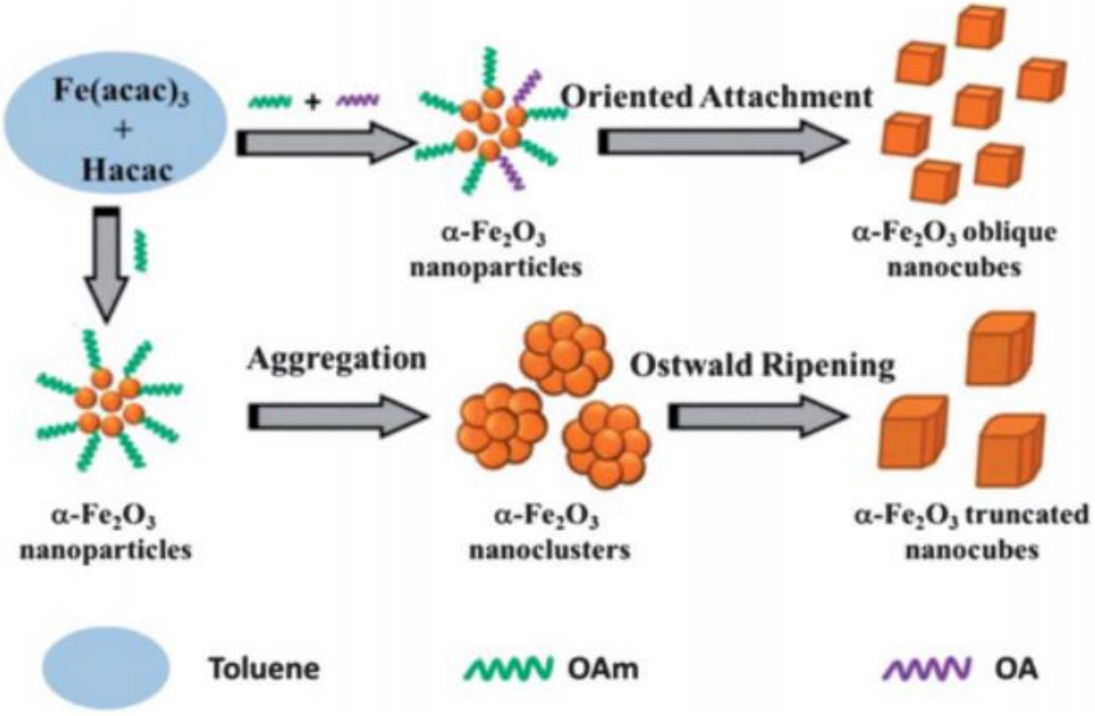

Figure 17: [57] Formation mechanism (oriented attachment mechanism and Oswald ripening mechanism) of oblique and truncated α-Fe_2O_3 nanocubes.

In order to investigate the influence of reaction time on the formation of Fe_2O_3 nanoparticles, TEM was applied to characterize the obtained Fe_2O_3 nanoparticles. Figure 18 shows the TEM images of Fe_2O_3 nanocubes synthesized at different reaction conditions. Specifically, Figure 18(a) – 18(c) shows the TEM images of Fe_2O_3 nanoparticles synthesized by gradually changing the solvothermal treatment time in the presence of oleic acid (OA). When the solvothermal treatment time is short, 0.5h (see Figure 18(a)), only small nanoparticles with irregular shape were formed. With increasing the solvothermal treatment time to 1h (see Figure 18(b)), some nanocubes started to form by the aggregation of previous small nanoparticles. By forming the larger nanocubes, the surface energy of small nanoparticles will decrease, and the nanoparticles become more stable. By further increasing the solvothermal treatment time to 2h (see Figure 18(c)), crystal growth finished and more nanocubes were produced. This process is ruled by oriented attachment mechanism. Furthermore, Figure 18(d) – 18(f) shows the TEM images of Fe_2O_3 nanoparticles by gradually changing the solvothermal treatment time in the absence of oleic acid (OA). For this case, a completely different mechanism was proposed. When the solvothermal treatment time is short, 20min (see Figure 18(d)), small nanoparticles with irregular shape aggregated together to form larger spherical shape nanoparticles. With increasing the solvothermal treatment time to 30min (see Figure 18(e)), some truncated nanocubes started to form at the edge of the nanosphere. By further increasing the solvothermal treatment time to 40min (see Figure 18(f)), more truncated nanocubes were produced. This process is ruled by Oswald ripening mechanism. The smaller nanoparticles dissolve and deposit on the larger truncated nanocubes.

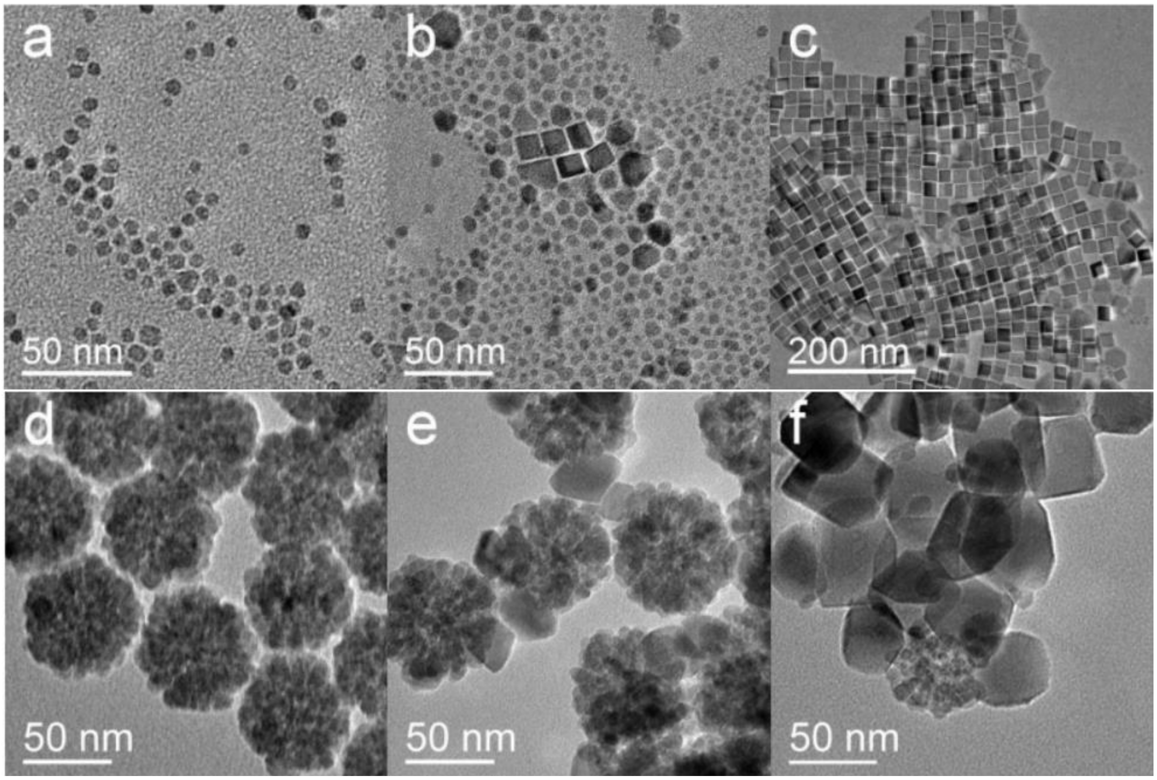

Figure 18: [57] TEM images of α-Fe_2O_3 oblique nanocubes (a - c) and truncated nanocubes (d - e) synthesized by changing solvothermal treatment time (a: 0.5h; b: 1h; c: 2h; d: 20min; e: 30min; f: 40min).

Besides the reaction conditions discussed above, the valence state of cations and the type of anions in the precursor, as well as the type of dopant, will also affect the formation of metal oxide nanocubes. Taniguchi et al. [58] synthesized ceria nanocubes through hydrothermal method by using cerium precursors with different cerium valence state ($(NH_4)_2Ce(NO_3)_6$ and $Ce(NO_3)_3$). During this process, ceria nanocubes were formed by following different formation mechanisms: For Ce^{4+} precursor ($(NH_4)_2Ce(NO_3)_6$), the formation follows Oswald ripening mechanism, when the small nanoparticles dissolved and precipitated on the larger nanoparticles to form nanocubes. On the other hand, by using Ce^{3+} precursor ($Ce(NO_3)_3$), the formation of nanoparticles was ruled by oriented attachment mechanism: The nanocubes with exposed {200} facets will attach to each other along [001] zone axis to form larger nanocubes. Moreover, because many Ce^{3+} ions exist on the surface of small nanocubes, the overall surface energy is high. Therefore, in order to decrease the surface energy, small nanocubes will aggregate together to form larger nanocubes by the dipole-dipole interaction between {200} facets to decrease the total surface energy and reach a stable state.

Wu et al. [59] also synthesized CeO_2 nanoparticles through hydrothermal method and investigated how the anions in the precursor will affect the morphology of CeO_2 nanoparticles. $Ce(NO_3)_3$ and $CeCl_3$ were used as precursors. Figure 19 shows the TEM images of CeO_2 nanoparticles synthesized under different reaction conditions. Figure 19(a) shows the CeO_2 nanoparticles synthesized by using $CeCl_3$ as precursor, where CeO_2 nanoparticles have rod shape. Figure 19(b) – 19(f) show the CeO_2 nanoparticles synthesized by using $Ce(NO_3)_3$ as precursor with prolonging reaction time from 7 h to 48 h CeO_2 nanocubes were successfully synthesized. With increasing reaction time, more and more nanocubes were formed.

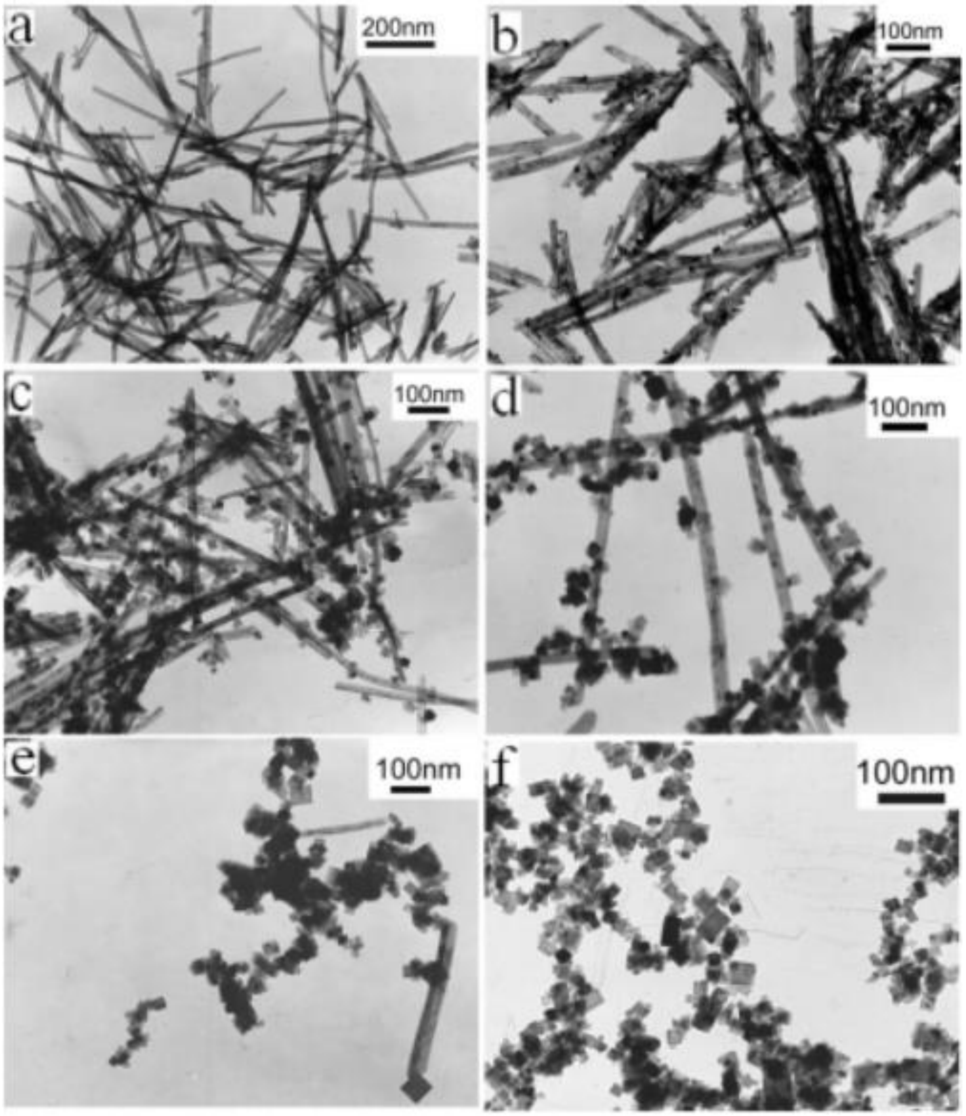

Figure 19: [59] TEM images of CeO_2 nanoparticles synthesized by using $Ce(NO_3)_3$ as precursor (b, c, d, e, f) and $CeCl_3$ as precursor (a) at different reaction time. a: 48 h; b: 7 h; c: 16 h; d: 26 h; e: 36 h; f: 48 h.

Figure 20 shows the corresponding formation process of CeO_2 nanoparticles and how the anions in the precursors influence the morphology of CeO_2 nanoparticles. Specifically, when using $CeCl_3$ as precursor, CeO_2 nanorods can be obtained through dissolution-recrystallization mechanism by oxidation and dehydration of $Ce(OH)_3$ nanorods. When $Ce(NO3)_3$ was used as precursor or sodium nitrate was added into the solution, nitrate ions drastically changed the formation mechanism. Nitrate ions oxidized Ce^{3+} ions to Ce^{4+} ions by extraction Ce^{3+} ions from $Ce(OH)_3$ nanorods. Therefore, $Ce(OH)_3$ nanorods will gradually disappear and CeO_2 nuclei will form. Then, nitrate ions working as capping agent adsorb on {100} crystal planes of CeO_2 nuclei, which significantly changed the surface energy and growth rate of different crystal planes. As discussed previously, crystal planes with high surface energy will grow rapidly and finally disappear, which leads to the formation of CeO_2 nanocubes with low surface energy.

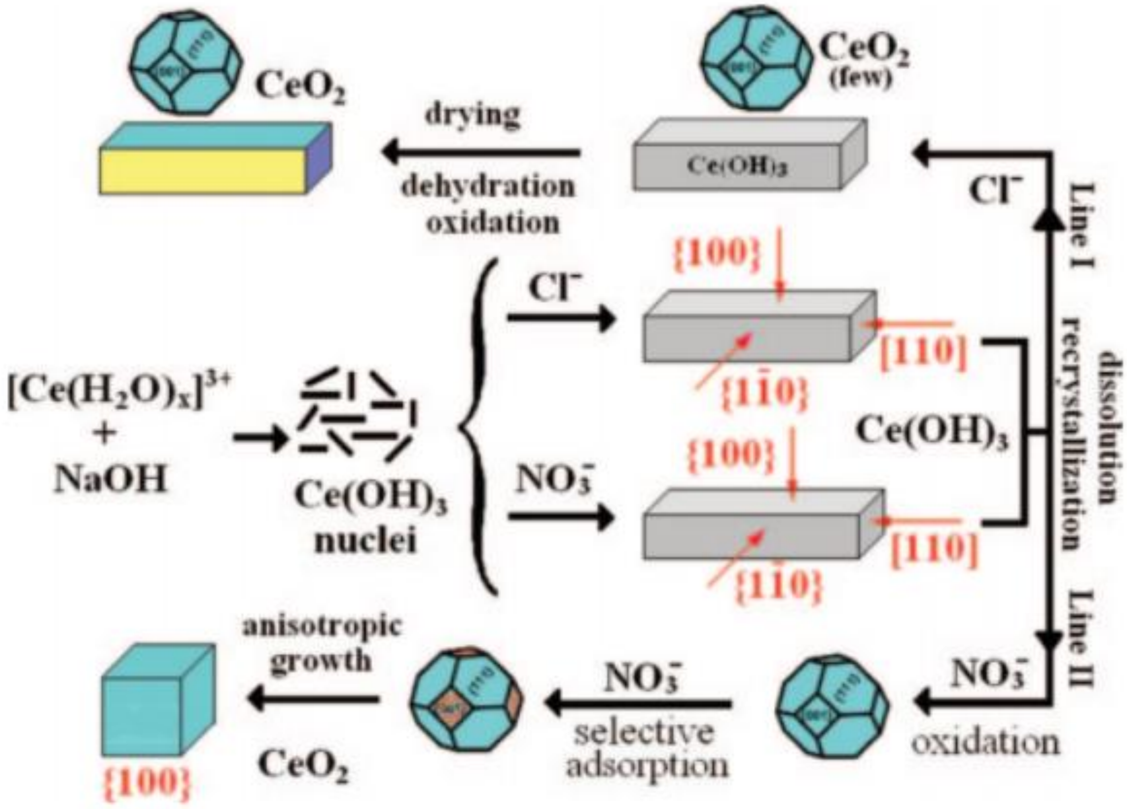

Figure 20: [59] Formation mechanism of CeO_2 nanorods and nanocubes.

Fisher et al. [17], [60] specifically investigated how the nitrate ions will affect the formation of CeO_2 nanocubes. CeO_2 nanoparticles were synthesized through a microwave-assisted hydrothermal method by using sodium nitrate as surface modifying agent. Without addition of sodium nitrate, nanorods were formed. In the presence of sodium nitrate, nanocubes were synthesized, and, with increasing the amount of sodium nitrate, the size of nanocube decreased. Therefore, sodium nitrate can not only modify the morphology of CeO_2 nanoparticles, but also restrict the crystal growth of CeO_2 nanoparticles. A corresponding proposed mechanism was proposed is shown on Figure 21. Specifically, $Ce(OH)_3$ nuclei will form at the beginning of the reaction. By applying a high reaction temperature, $Ce(OH)_3$ nuclei will be oxidized into CeO_2 nuclei. Without sodium nitrate, CeO_2 nuclei will absorb adequate microwave energy, which will facilitate the growth of crystal planes with low formation energy, therefore, nanorods are obtained. When adding a large amount of sodium nitrate, sodium nitrate molecules will adsorb on the {100} facets, which promotes the formation of {100} facets and destabilizes the formation of {111} and {110} facets, therefore, nanocubes are synthesized. In addition, nitrate ions can restrict the deposition of cerium nitrate precursor on the surface of nanocubes, resulting in the diffusion-controlled growth, which favors the formation of symmetric morphology, for example cubic morphology.

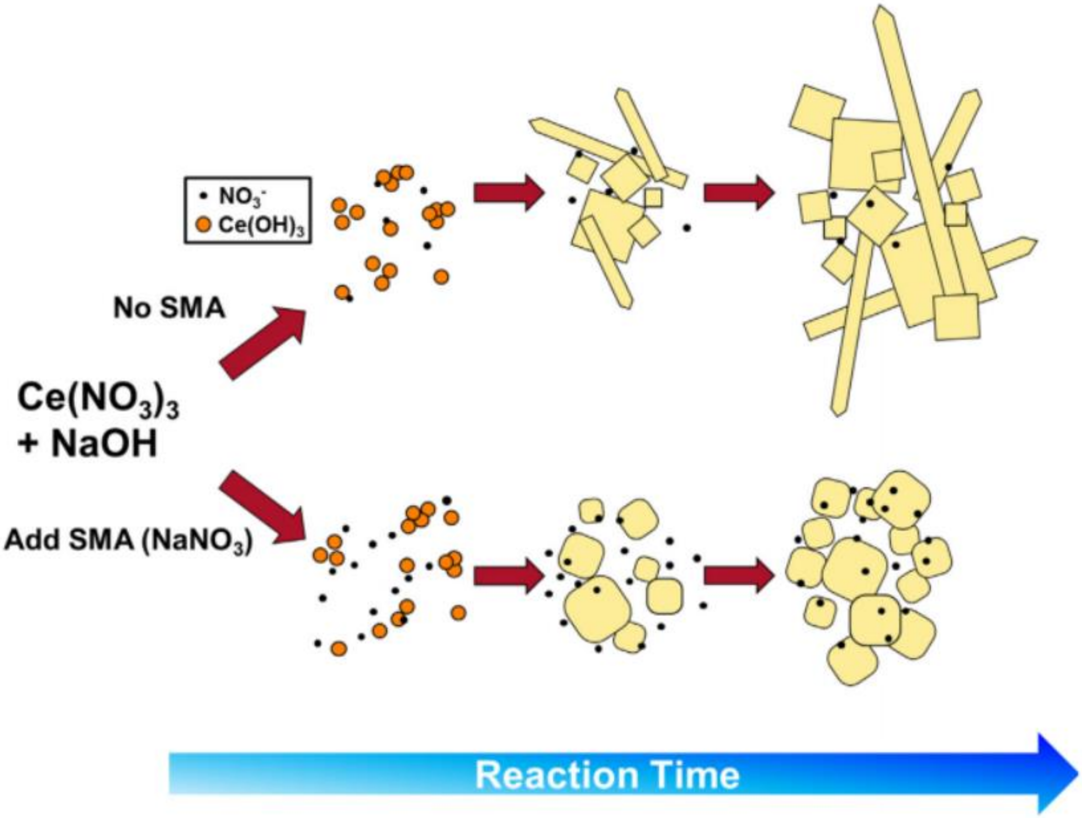

Figure 21: [60] Formation process of CeO_2 nanoparticles of different morphology.

Another factor that affects the formation of CeO_2 nanoparticles is the doping atoms. Mendiuk et al. [61] synthesized $Ce_{1-x}Ln_xO_{2-y}$ nanoparticles doped with different metal elements (Ln = Pr, Sm, Gd, Tb) through hydrothermal method. The morphology and size of $Ce_{1-x}Ln_xO_{2-y}$ nanoparticles were related to the doping level and the type of doping elements. When $0.05 < x < 0.1$, $Ce_{1-x}Ln_xO_{2-y}$ nanocubes were synthesized with a narrow size distribution. When $0.2 < x < 0.3$, the growth of $Ce_{1-x}Ln_xO_{2-y}$ nanocubes was restricted and the morphology changed from nanocube to nanosphere. At $x > 0.3$, $Ln(OH)_3$ nanorods were obtained as a second phase. In addition, compared to Tb and Pr doping, Gd and Sm facilitate the formation of larger ceria nanocubes.

CHAPTER 1 BARIUM AND STRONTIUM TITANATE NANOCUBES

Barium titanate ($BaTiO_3$) and strontium titanate ($SrTiO_3$) are two types of metal oxide materials with ABO_3 perovskite structure. Because of their excellent ferroelectric, dielectric, and thermoelectric properties, $BaTiO_3$ and $SrTiO_3$ nanoparticles have been widely used in energy conversion devices (capacitors), thermistors and photocatalyst [62]–[64].

Many studies have shown that the ferroelectric and dielectric properties of $BaTiO_3$ and $SrTiO_3$ nanoparticles highly depended on their size and morphology [65]–[68]. Therefore, a better understanding on the size- and morphology-controlled synthesis process is important for studying the ferroelectric and dielectric properties of $BaTiO_3$ and $SrTiO_3$ nanoparticles.

Another reason for investigating the synthesis process of $BaTiO_3$ and $SrTiO_3$ nanoparticles is to find a suitable way to obtain $BaTiO_3$ and $SrTiO_3$ nanocubes. As was discussed earlier in the Introduction part, the advantage of nanocubes is at that it can easily form ordered self-assembly, which exhibits excellent dielectric properties.

Multiple studies have been conducted to investigate the size- and morphology-controlled synthesis of $BaTiO_3$ and $SrTiO_3$ nanocubes. For example, Fujinami et al. [69] synthesized $SrTiO_3$ nanocubes through hydrothermal method. The morphology and size of nanoparticle depended on the reaction temperature and capping agent (oleic acid). When the reaction temperature was low (120 ℃) and no oleic acid was added into the solution, $SrTiO_3$ nanoparticles had irregular shape, while with increasing the reaction temperature and adding the oleic acid, $SrTiO_3$ nanocubes with the size of sub-10 nm and sharp edges were successfully obtained. The oleic acid molecules, working as capping agents, adsorbed on the surface of $SrTiO_3$ nanocubes, which restricted the dissolution of high-energy faceted edges of $SrTiO_3$ nanocubes and facilitated the crystallographic growth. Therefore, $SrTiO_3$ nanocubes were obtained.

Borah et al. [70] synthesized $BaTiO_3$ nanocubes through a composite-hydroxide-mediated method and found out that the size of $BaTiO_3$ nanocubes depended on the reaction time. By increasing the reaction time from 12 h to 28 h, the size of nanocube increased from 3 nm to 44 nm.

Furthermore, Hou et al. [71] synthesized barium strontium titanate ($Ba_xSr_{1-x}TiO_3$) through solvothermal method. They found the morphology of BST nanoparticles depended on the molar ratio of Sr/(Sr + Ba). When the molar ratio of Sr/(Sr + Ba) is below 0.5, nanocubes were formed. With increasing the molar ratio of Sr/(Sr + Ba) to 0.75, nanospheres were obtained, and they were also highly agglomerated.

Several researchers also focused on the synthesis of ordered assembly by using $BaTiO_3$ and $SrTiO_3$ nanocubes as building blocks and studied their dielectric properties. Specifically, Mimura et al. [72] studied the dielectric properties of $BaTiO_3$ ordered assembly synthesized by dip-coating method and sintered at different temperature (from 750 ℃ to 900 ℃). Figure 22 shows the SEM images of $BaTiO_3$ ordered assemblies sintered at different sintering temperature. When the sintering temperature was low (750 ℃), the individual nanocubes can be observed, which indicated that the face-to-face conjugation between nanocubes did not happen, therefore, the assembly was brittle (see Figure 22(b)). By increasing the sintering temperature, face-to-face conjugation happened between nanocubes (see Figure 22(c)). This process was due to the epitaxial attachment without crystal growth. In addition, with increasing sintering temperature, cracks were formed, which indicates the interfacial strain (see Figure 22(d) and 22(e)). The corresponding dielectric constant for those assemblies was also characterized. It was verified, for example, that $BaTiO_3$ ordered assemblies sintered at 800 ℃ and 850 ℃ showed the highest dielectric constant ($\varepsilon = 4000$) compared with other samples ($\varepsilon = 3000$ was found for $BaTiO_3$ ordered assembly sintered at 900 ℃). The dielectric constant for $BaTiO_3$ ordered assembly sintered at 750 ℃ cannot be measured because the ordered assembly was brittle and can be easily broken by the probe.

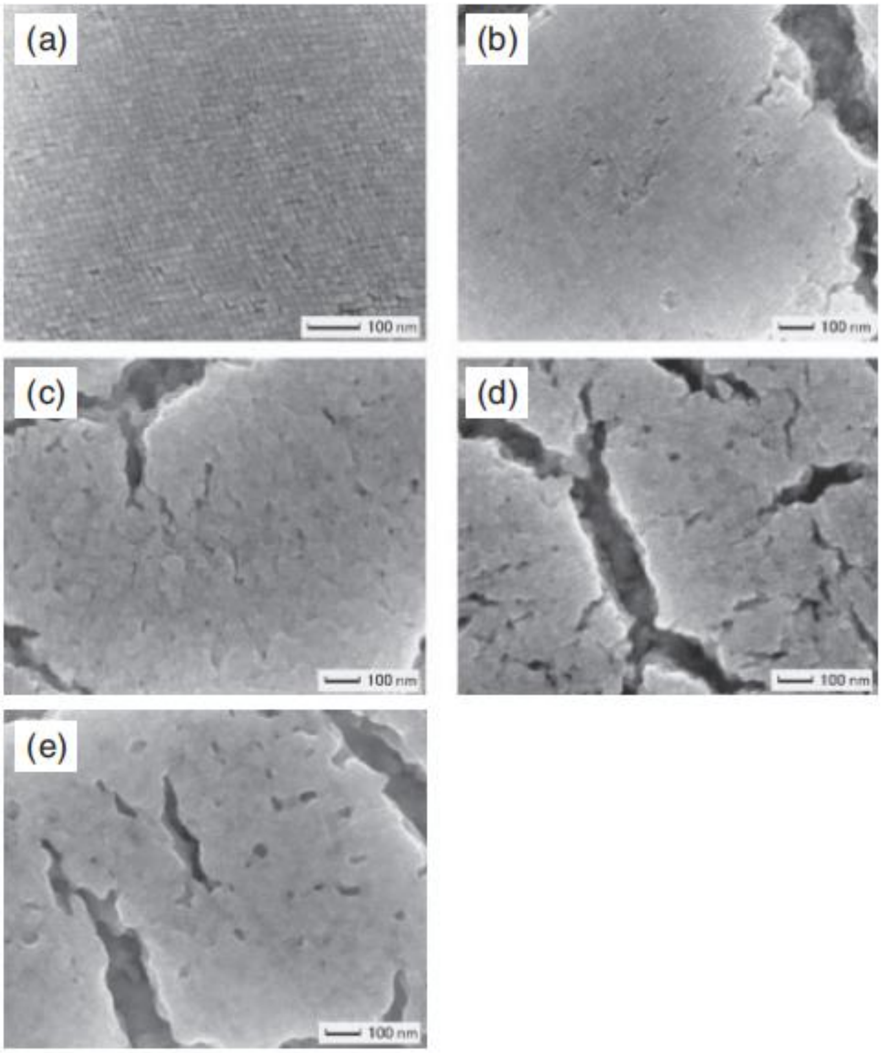

Figure 22: [72] SEM images of $BaTiO_3$ assembly before and after sintering. (a) before sintering; (b) sintered at 750 ℃; (c) sintered at 800 ℃; (d) sintered at 850 ℃; and (e) sintered at 900 ℃.

In addition, by using $SrTiO_3$ (ST) and $BaTiO_3$ (BT) nanocubes as building blocks, Mimura et al. [73], [74] fabricated ST, BT and ST-BT mixture self-assembly through capillary-force-assisted method and studied the formation mechanism of this self-assembly. From SEM characterization (see Figure 23), the formation of ST (Figure 23(a)), BT (Figure 23(b) and 23(c)) and ST-BT (Figure 23(d)) mixture self-assembly were confirmed. The nanocubes attached to each other face to face. This attachment restricted the mass transfer and grain growth; therefore, the structure of ordered assembly can be retained even after the high temperature treatment. The formation process of ST-BT mixture hetero-assembly (see Figure 23(d)) can be described as following (shown on Figure 24): First, with evaporation of the solution, convection happens and the nanocubes gradually start to deposit on the substrate (see Step 1 in Figure 24). Next, highly ordered assembly is formed under the capillary immersion force and lateral capillary force (see Step 2 in Figure 24). During this process, the capping agent (oleic acid) works as lubricant. The nanocubes can move easily on the substrate and form ordered assembly.

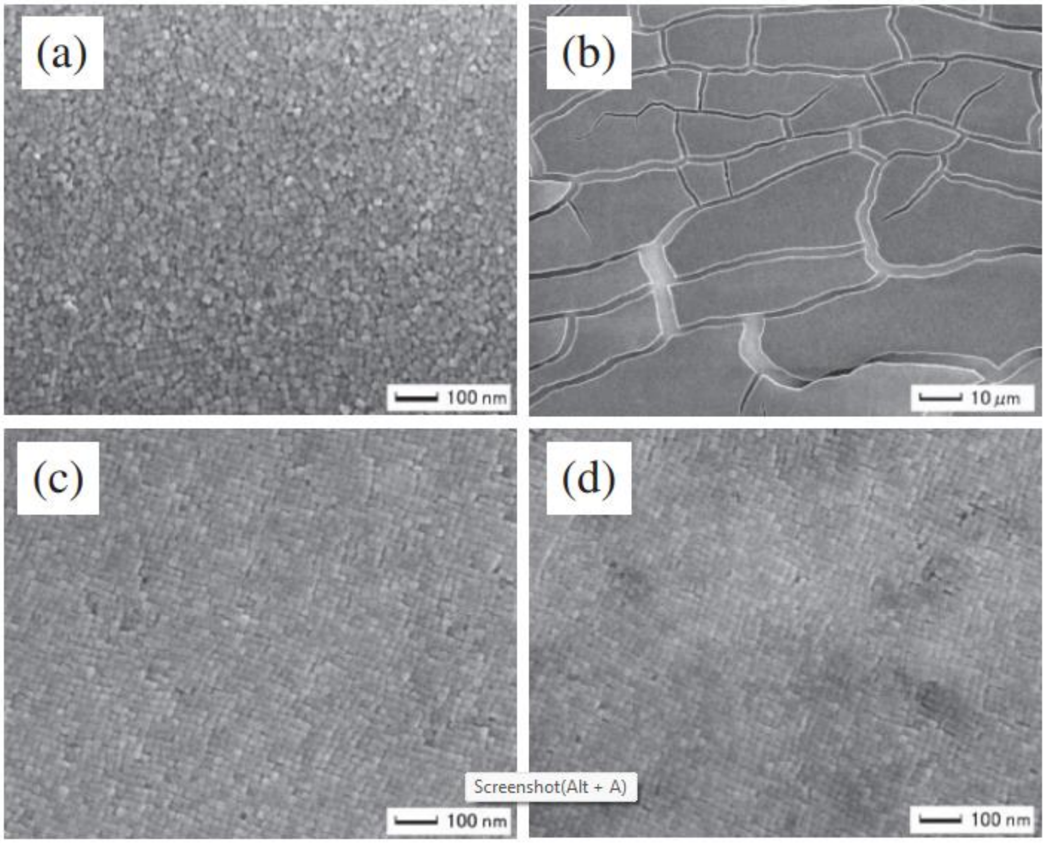

Figure 23: [73] SEM images of (a) ST nanocube assembly, (b) and (c) BT nanocube assembly, and (d) BT–ST nanocube mixture assembly.

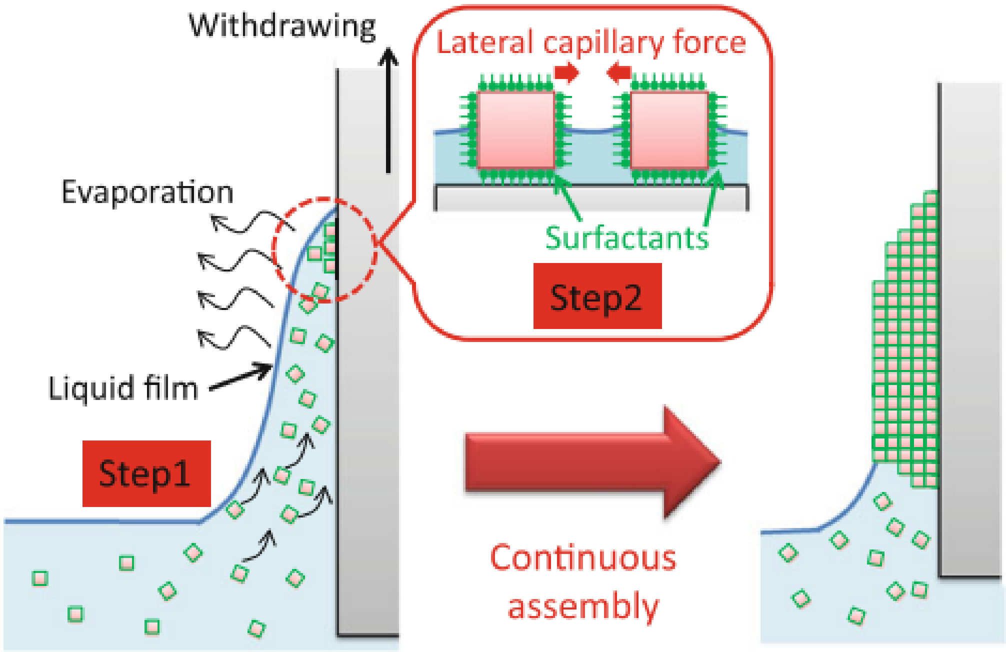

Figure 24: [75] Formation process (capillary-force-assisted method) of ST, BT and ST-BT mixture self-assemblies.

Furthermore, Ma et al. [76] studied the crystallographic fusion behavior and interface evolution of $BaTiO_3$ ordered assembly, which clearly illustrates why this assembly has excellent dielectric properties (with dielectric constant of 4000 [72]). The assembly formed by the capillary force due to evaporation of the solvent and by the van der Waals forces between oleic acid molecules on the surface of $BaTiO_3$ nanocubes. It was found that, during sintering process, the thermal expansion and epitaxial attachment between nanocubes leads to the formation of misalignment of $BaTiO_3$ nanocubes, edge dislocations and lattice distortion. These defects facilitate the formation of special transmission channels for electrons, which results in the high dielectric constant of $BaTiO_3$ ordered assembly. Figure 25 shows the crystallographic fusion behavior of $BaTiO_3$ ordered assembly. Semi-coherent fusion region with atom-to-atom attached interface was formed after sintering at 850 °C. Lattice defects generated at the interface region of nanocubes. After sintering at 950 °C, small angle grain boundary and edge dislocations formed.

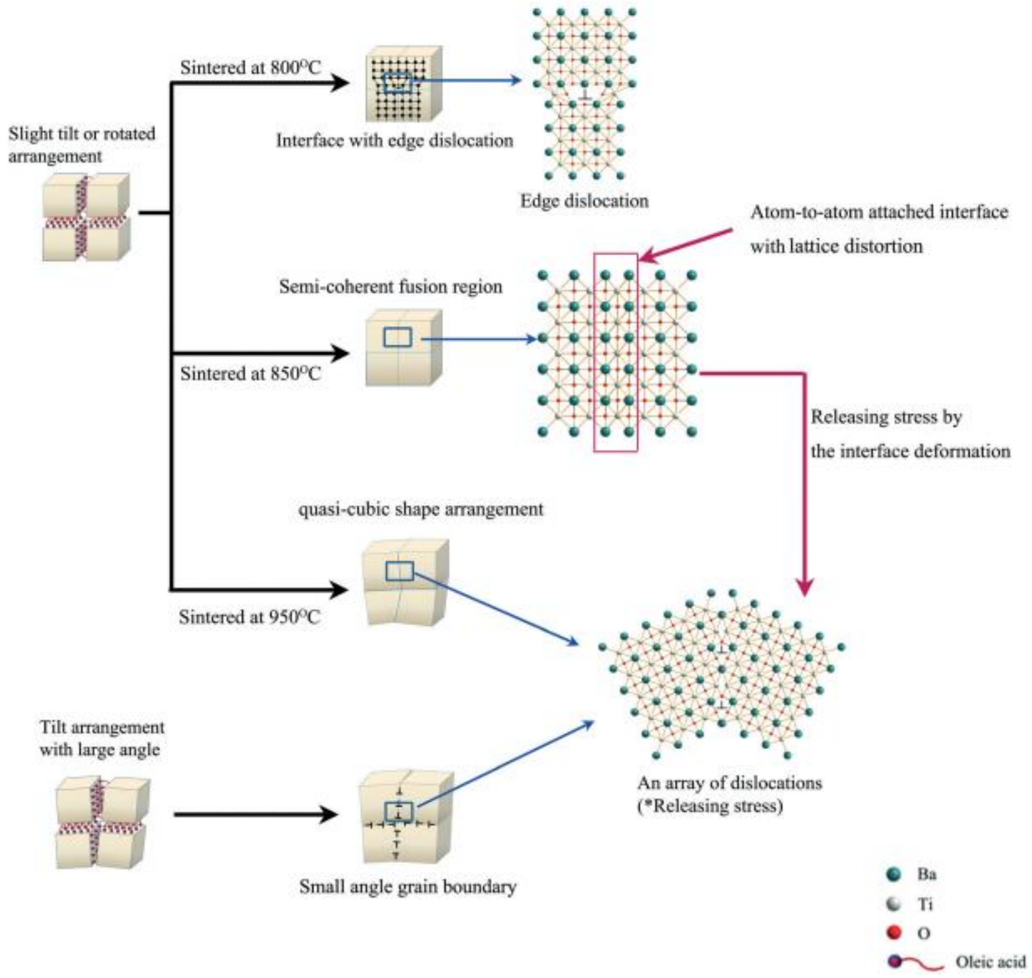

Figure 25: [76] Crystallographic fusion behavior of $BaTiO_3$ ordered assembly.

Although many studies have been done on the $BaTiO_3$ and $SrTiO_3$ nanocubes, the formation mechanisms of $BaTiO_3$ and $SrTiO_3$ nanocubes are still unclear. In situ formation mechanism and dissolution-precipitation mechanism were used to explain the formation of $BaTiO_3$ and $SrTiO_3$ nanocubes, as was mentioned in the Introduction part [40], [43]–[45]. In these studies, oleic acid and hydrazine were used as capping agent. However, oleic acid or hydrazine can negatively affect the formation mechanism of $BaTiO_3$ and $SrTiO_3$ nanocubes according to the Introduction section. Therefore, the formation mechanisms of $SrTiO_3$ and $BaTiO_3$ nanocubes synthesized by using capping agents are not the intrinsic formation mechanism of $SrTiO_3$ and

$BaTiO_3$ nanocubes. In addition, the capping agents will adsorb on the surface of $BaTiO_3$ and $SrTiO_3$ nanocubes, which will contaminate the nanocubes.

In order to get pure $BaTiO_3$ and $SrTiO_3$ nanocubes and better understand the formation mechanisms, $BaTiO_3$ and $SrTiO_3$ nanocubes should be synthesized without capping agents. Therefore, one of the main goals of this thesis is to find the synthesis methods to successfully synthesize $BaTiO_3$ and $SrTiO_3$ nanocubes without using any capping agent. For that, two synthesis methods (molten-salt and hydrothermal) were investigated to determine which synthesis method is suitable for obtaining $BaTiO_3$ or $SrTiO_3$ nanocubes.

The other goal is to use different characterization methods (such as X-ray diffraction (XRD), scanning electron microscopy (SEM) and transmission electron microscopy (TEM)) to verify the feasibility of these two synthesis methods. By using XRD, the phases appearing in the $BaTiO_3$ and $SrTiO_3$ nanoparticles and the phase purity were characterized. Crystallite size of $BaTiO_3$ and $SrTiO_3$ was also evaluated based on the XRD diffraction patterns by using Scherrer equation, and the influences of reaction temperature, reaction time and synthesis method on the size of $BaTiO_3$ and $SrTiO_3$ crystallites were discussed. The actual morphology of $BaTiO_3$ and $SrTiO_3$ nanoparticle was observed by SEM. TEM was applied to confirm that the $BaTiO_3$ (or $SrTiO_3$) nanoparticles synthesized by using molten-salt method (or hydrothermal method) have cubic morphology. The electron diffraction patterns were obtained to further confirm the crystal structure of synthesized $BaTiO_3$ and $SrTiO_3$ nanocubes, and the high-resolution TEM images of synthesized nanocubes were also acquired. Combining the TEM results and the formation mechanisms of metal oxide nanocubes discussed in the Introduction section, the formation mechanisms of the $BaTiO_3$ and $SrTiO_3$ nanocubes were also proposed and discussed in detail.

CHAPTER 2 EXPERIMENTAL PROCEDURE

2.1 SYNTHESIS OF BARIUM TITANATE AND STRONTIUM TITANATE NANOPARTICLES

Hydrothermal methods (Method 1 and Method 3) and molten-salt method (Method 2) were used in the current study to synthesize $BaTiO_3$ and $SrTiO_3$ nanoparticles.

Method 1 (hydrothermal synthesis) was used to prepare samples BT1 – BT9 and ST1 – ST9 (BT = Barium titanite, ST = Strontium titanite). Barium nitrate ($Ba(NO_3)_2$) and titanium dioxide (TiO_2) were used as main reactants to synthesize $BaTiO_3$ nanoparticles, while strontium nitrate ($Sr(NO_3)_2$) and titanium dioxide (TiO_2) were used as main reactants to synthesize $SrTiO_3$ nanoparticles. In a typical synthesis process, 66.6 mg $Ba(NO_3)_2$ (or 54 mg $Sr(NO_3)_2$) were added into 25 mL deionized water. The mixed solution was kept on the stirring plate for 10 min. Next, 5 g of NaOH were added into the mixed solution and stirred for another 10 min. 20.4 mg TiO_2 were added into the above solution and stirred for 10 min. At the end, the uniform solution was transformed into the Teflon-lined stainless-steel autoclave and kept in the oven at different temperatures (180 ℃, 200 ℃ and 220 ℃) for different times (12 h, 18 h and 24 h), see Table 1 for all the details about the corresponding parameters of this synthesis.

Method 2 (molten-salt synthesis) was used to prepare samples BT10 – BT18 and ST10 – ST18. Barium carbonate ($BaCO_3$) and titanium dioxide (TiO_2) were used as main reactants to synthesize $BaTiO_3$ nanoparticles, while strontium carbonate ($SrCO_3$) and titanium dioxide (TiO_2) were used as main reactants to synthesize $SrTiO_3$ nanoparticles. In a typical synthesis process, 4.636 g NaOH and 4.365 g KOH were first put into the Teflon vessel. Then, 98.7 mg $BaCO_3$ (or 73.8 mg $SrCO_3$) and 39.9 mg TiO_2 were added into the Teflon vessel. Finally, the Teflon vessel was put into the stainless-steel autoclave and kept in the oven at different temperatures (180 ℃, 200 °C and 220 °C) for different times (12 h, 18 h and 24 h), see Table 1 for all the details about the corresponding parameters of this synthesis.

Method 3 (hydrothermal synthesis) was used to prepare BT19 – BT27 and ST19 – ST27 samples. The synthesis process is similar to Method 1. The only difference is that, instead of using 5 g of solid NaOH, 6 mL of 5 M NaOH solution was used in Method 3. The 5 M NaOH solution was prepared by adding 10 g of solid NaOH into 50 mL deionized water, and keeping the mixed solution on the stirring plate for 10 min. See Table 1 for all the details about the corresponding parameters of this synthesis.

The obtained $BaTiO_3$ and $SrTiO_3$ nanoparticles were collected by centrifuging and washed with acetic acid and ethanol to remove impurities. In the typical procedure, 25 mL of acetic acid was added into 25 mL of deionized water under continuous stirring. The solution was stirred for 5 min. $BaTiO_3$ (or $SrTiO_3$) powder was added to the solution and mixed for 10 minutes. The $BaTiO_3$ (or $SrTiO_3$)/acetic acid/DI water solution was divided into two 50 mL centrifuge tubes; each tube was filled to 25 mL. The samples were washed once with the diluted acetic acid solution and twice with ethanol. All the experiments, including the reaction temperature, reaction time and precursors, are summarized in Table 1.

Table 1: Synthesis conditions (reaction time, reaction temperature and precursors) to produce $BaTiO_3$ and $SrTiO_3$ powder.

Sample	Temperature (°C)	Time (h)	Carbonate precursor (mg)	Nitrate precursor (mg)	NaOH (g)	KOH (g)	TiO_2 (mg)	Deionized water (mL)
Method 1 (Hydrothermal synthesis)								
BT1	180	12	0	66.6	5	0	20.4	25
BT2	180	18	0	66.6	5	0	20.4	25

Table 1: continued

BT3	180	24	0	66.6	5	0	20.4	25
BT4	200	12	0	66.6	5	0	20.4	25
BT5	200	18	0	66.6	5	0	20.4	25
BT6	200	24	0	66.6	5	0	20.4	25
BT7	220	12	0	66.6	5	0	20.4	25
BT8	220	18	0	66.6	5	0	20.4	25
BT9	220	24	0	66.6	5	0	20.4	25
ST1	180	12	0	54	5	0	20.4	25
ST2	180	18	0	54	5	0	20.4	25
ST3	180	24	0	54	5	0	20.4	25
ST4	200	12	0	54	5	0	20.4	25
ST5	200	18	0	54	5	0	20.4	25
ST6	200	24	0	54	5	0	20.4	25
ST7	220	12	0	54	5	0	20.4	25
ST8	220	18	0	54	5	0	20.4	25
ST9	220	24	0	54	5	0	20.4	25
Method 2 (Molten-salt synthesis)								
BT10	180	12	98.7	0	4.635	4.365	39.9	0
BT11	180	18	98.7	0	4.635	4.365	39.9	0
BT12	180	24	98.7	0	4.635	4.365	39.9	0
BT13	200	12	98.7	0	4.635	4.365	39.9	0
BT14	200	18	98.7	0	4.635	4.365	39.9	0

Table 1: continued

BT15	200	24	98.7	0	4.635	4.365	39.9	0
BT16	220	12	98.7	0	4.635	4.365	39.9	0
BT17	220	18	98.7	0	4.635	4.365	39.9	0
BT18	220	24	98.7	0	4.635	4.365	39.9	0
ST10	180	12	73.8	0	4.635	4.365	39.9	0
ST11	180	18	73.8	0	4.635	4.365	39.9	0
ST12	180	24	73.8	0	4.635	4.365	39.9	0
ST13	200	12	73.8	0	4.635	4.365	39.9	0
ST14	200	18	73.8	0	4.635	4.365	39.9	0
ST15	200	24	73.8	0	4.635	4.365	39.9	0
ST16	220	12	73.8	0	4.635	4.365	39.9	0
ST17	220	18	73.8	0	4.635	4.365	39.9	0
ST18	220	24	73.8	0	4.635	4.365	39.9	0
Method 3 (Hydrothermal synthesis)								
BT19	180	12	0	66.6	6 mL	0	20.4	25
BT20	180	18	0	66.6	6 mL	0	20.4	25
BT21	180	24	0	66.6	6 mL	0	20.4	25
BT22	200	12	0	66.6	6 mL	0	20.4	25
BT23	200	18	0	66.6	6 mL	0	20.4	25
BT24	200	24	0	66.6	6 mL	0	20.4	25
BT25	220	12	0	66.6	6 mL	0	20.4	25
BT26	220	18	0	66.6	6 mL	0	20.4	25

Table 1: continued

BT27	220	24	0	66.6	6 mL	0	20.4	25
ST19	180	12	0	54	6 mL	0	20.4	25
ST20	180	18	0	54	6 mL	0	20.4	25
ST21	180	24	0	54	6 mL	0	20.4	25
ST22	200	12	0	54	6 mL	0	20.4	25
ST23	200	18	0	54	6 mL	0	20.4	25
ST24	200	24	0	54	6 mL	0	20.4	25
ST25	220	12	0	54	6 mL	0	20.4	25
ST26	220	18	0	54	6 mL	0	20.4	25
ST27	220	24	0	54	6 mL	0	20.4	25

2.2 X-RAY DIFFRACTION (XRD)

Phase and phase purity were characterized by X-ray diffraction (XRD) on a D2 Phaser (Bruker AXS, Madison, WI). Data were collected from using a step size of 0.014 degrees 2θ and a count time of 0.3 s, scanning from 15 to 85 degrees 2θ.

2.3 SCANNING ELECTRON MICROSCOPY (SEM)

The synthesized $BaTiO_3$ (or $SrTiO_3$) nanoparticles were dispersed into 300 mL isopropanol (IPA); the solution was stirred for 5 min. The uniformed solution was ultrasonicated for 25 min by using a pulse ultrasonicator; the cycle consists of 30 s “on” and 10 s “off”. Finally, one drop of the above uniformed solution was placed on the silicon wafer and left in the open atmosphere at room temperature to allow the solvent to evaporate gradually. Before acquiring the images, the samples were sputter coated by iridium. SEM images were acquired on a FEI Apreo SEM, operating at 5 kV and 0.10 nA, and FEI Quanta FEG 250 SEM, operating at 5 kV and 0.10 nA.

2.4 TRANSMISSION ELECTRON MICROSCOPY (TEM)

The morphology of the synthesized $BaTiO_3$ and $SrTiO_3$ nanoparticles were characterized by transmission electron microscopy (TEM). The obtained $BaTiO_3$ and $SrTiO_3$ nanoparticles were dispersed into 300 mL isopropanol (IPA). TEM samples were prepared by first adding three drops of a 300 mL dilute suspension of the nanoparticles into 25 mL IPA. The suspension was ultrasonicated for 25 min by using a bath ultrasonicator. One drop of the above further diluted solution was placed on a 200-mesh carbon-coated copper grid. The grid was placed in the furnace at 75 ℃ to completely evaporate the solvent. TEM images, HRTEM images and electron diffraction patterns were obtained by using a Thermofisher Talos 200X G2-S transmission electron microscope operated at 200 kV.

CHAPTER 3 RESULTS AND DISCUSSIONS

3.1 XRD RESULTS

In order to study which synthesis method (hydrothermal or molten-salt) can successfully get $BaTiO_3$ or $SrTiO_3$ phase, XRD was used to determine the crystal structure of synthesized $BaTiO_3$ and $SrTiO_3$ material. Furthermore, based on the XRD results and Scherrer equation [77], the influences of reaction temperature, reaction time and synthesis methods on the size of $BaTiO_3$ and $SrTiO_3$ crystallites were discussed.

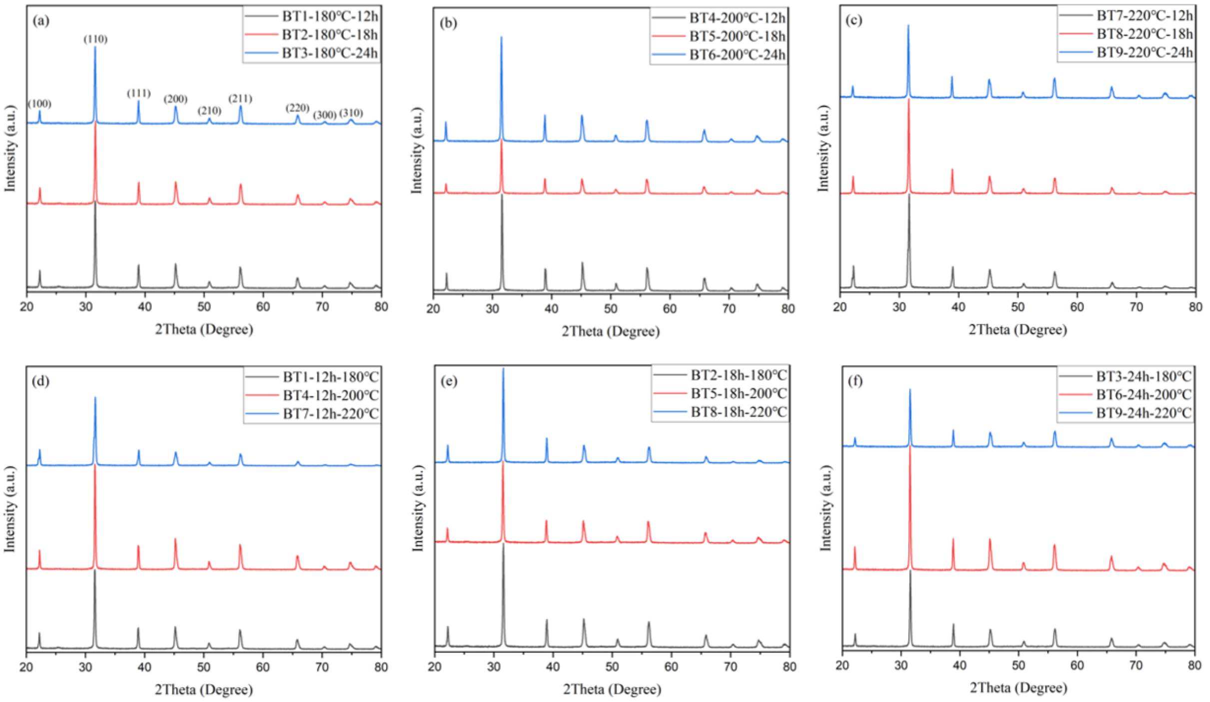

Figure 26: XRD results of $BaTiO_3$ powder (BT1 - BT9) synthesized by Method 1 (hydrothermal).

Figure 26 shows the X-ray diffraction patterns of $BaTiO_3$ powder synthesized at different reaction temperatures (180 °C, 200 °C and 220 °C) and reaction times (12 h, 18 h and 24 h) by the above-mentioned Method 1 (hydrothermal). All diffraction peaks were indexed as (100), (110), (111), (200), (210), (211), (220), (300), (310) and (311) crystal planes which corresponds to the cubic perovskite $BaTiO_3$ phase (PDF#01-070-9165). No other peaks were observed which indicates the high purity of synthesized $BaTiO_3$ powder. In addition, the diffraction peaks are sharp which indicates the high crystallinity of synthesized $BaTiO_3$ power. Therefore, based on the above XRD results, the $BaTiO_3$ nanoparticles can be successfully synthesized by Method 1 (hydrothermal).

Furthermore, from the XRD results summarized on Figure 26, the width of diffraction peaks did not change by changing the reaction time (as shown in Figure 26(a) – 24(c)) and reaction temperature (as shown in Figure 26(d) – 24(f)), which indicates that by increasing the reaction time from 12 h to 24 h and reaction temperature from 180 ℃ to 220 ℃, the size of $BaTiO_3$ crystallites did not change significantly. This result suggested that the growth of $BaTiO_3$ crystallites has completed when the synthesis was conducted at 180 ℃ for 12 h. Further increasing reaction time and reaction temperature does not significantly affect the growth of $BaTiO_3$ crystallites.

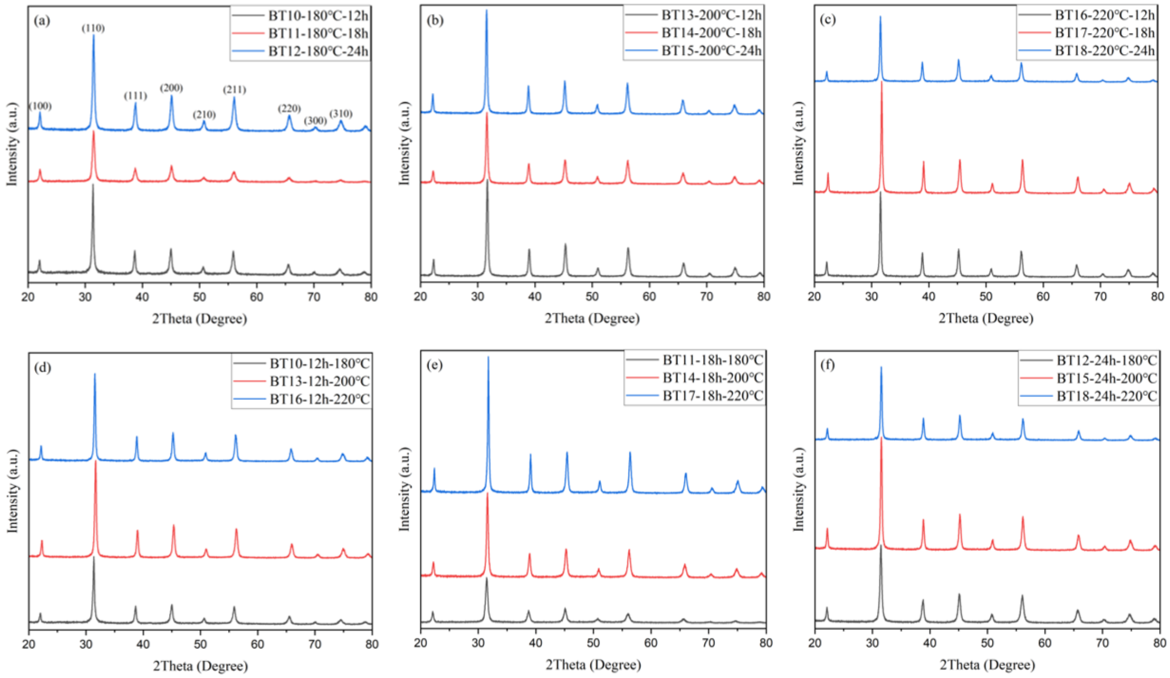

Figure 27: XRD results of $BaTiO_3$ powder (BT10 - BT18) synthesized by Method 2 (molten-salt).

Figure 27 shows the X-ray diffraction patterns of $BaTiO_3$ powder synthesized at different reaction temperatures (180 ℃, 200 ℃ and 220 ℃) and reaction times (12 h, 18 h and 24 h) by the above-mentioned Method 2 (molten-salt). All diffraction peaks corresponded to the cubic perovskite $BaTiO_3$ phase (PDF#01-070-9165). No impurities were observed, and the sharp diffraction peaks indicated the high crystallinity of synthesized $BaTiO_3$ powder. Therefore, based on the XRD results summarized on Figure 27, the $BaTiO_3$ nanoparticles can also be successfully obtained by Method 2. Similar to the $BaTiO_3$ powder synthesized by Method 1, the width of diffraction peaks also did not change with changing the reaction temperature and time, which indicates the size of $BaTiO_3$ crystallites did not significantly change by increasing the reaction temperature and time.

In order to verify the above results that the size of $BaTiO_3$ crystallites synthesized by Method 1 and Method 2 did not significantly depend on the reaction temperature and reaction time, the crystallite size of $BaTiO_3$ was calculated by using Scherrer equation, as shown in equation (1), where D is the nanoparticle size, κ is the Scherrer constant ($\kappa = 0.9$ [77]), λ is the X-ray wavelength ($\lambda = 0.15406$ nm for Cu Kα X-ray), β is the full width at half maximum ((110) peak was used to calculate the value of full width at half maximum) and θ is the diffraction angle.

$$\boldsymbol{D = \frac{\kappa\lambda}{\beta cos\theta}} \ (\mathbf{1})$$

From Table 2, the crystallite size of synthesized $BaTiO_3$ material produced by Method 1 was in the range of 35 - 38 nm (except for the size of BT4 and BT7 samples which were found to be 41 and 26 nm). The crystallite size of $BaTiO_3$ material produced by Method 2 is in the range of 21 - 27nm (except for the size of BT11 and BT12 samples which were found to be 16 and 19 nm, respectively). The corresponding standard deviations were calculated for $BaTiO_3$ nanoparticles synthesized by Method 1 and Method 2 at different reaction temperatures and reaction times, which were only 1 nm and 2 nm. These results confirmed the above-mentioned conclusion that the size of synthesized $BaTiO_3$ crystallites did not significantly depend on the reaction temperature and reaction time.

In addition, comparing the diffraction peaks of $BaTiO_3$ nanoparticles synthesized through Method 1 and Method 2, the size difference can be observed by using the Scherrer equation. From Scherrer equation, small crystallite corresponds to broader diffraction peaks [78]. Figure 28 shows the XRD results of $BaTiO_3$ crystallites synthesized by Method 1 and Method 2 at the same reaction time and reaction temperature. When using Method 2, the diffraction peaks of $BaTiO_3$ crystallites are broader than the peaks of $BaTiO_3$ crystallites synthesized by Method 1, which indicates $BaTiO_3$ crystallites synthesized by Method 2 have smaller size. In addition, from Table 2, the $BaTiO_3$ crystallites synthesized by Method 2 (21 – 27 nm) had smaller sizes than the $BaTiO_3$ crystallites produced by Method 1 (35 – 38 nm) at the same reaction temperature and reaction time, which further confirmed the above result. Therefore, the size of $BaTiO_3$ crystallites synthesized by Method 1 and Method 2 follows the relationship of $BaTiO_{3\ (\text{Method 2})} < BaTiO_{3\ (\text{Method 1})}$.

Based on the calculation results presented here and the size-property relationship discussed in the Introduction part, the ferroelectric and dielectric properties can be different due to the corresponding crystallite size differences of the $BaTiO_3$. Further studies can be focused on investigating how this size difference will affect the ferroelectric and dielectric properties of the synthesized $BaTiO_3$, which can lead to a better understanding of the size-property relationship.

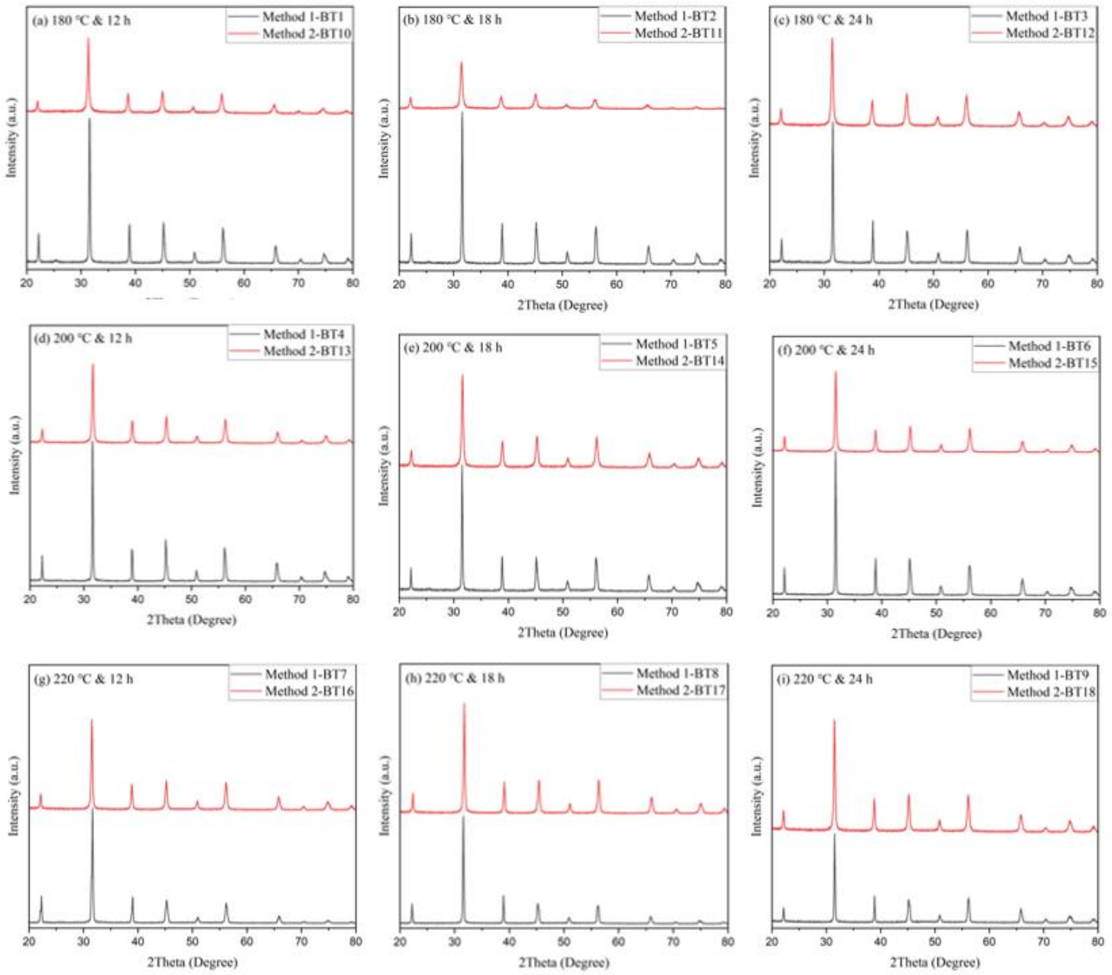

Figure 28: XRD results of $BaTiO_3$ powder synthesized by Method 1 and Method 2 under the same reaction temperature and reaction time.

Table 2: Calculation results of full width at half maximum (FWHM) and crystallite size of synthesized $BaTiO_3$.

Sample	FWHM	Crystallite size (nm)
Method 1 (Hydrothermal synthesis)		
BT1	0.2314	36
BT2	0.2368	35
BT3	0.2267	36
BT4	0.2021	41

Table 2: Continued.

BT5	0.2270	36
BT6	0.2155	38
BT7	0.3128	26
BT8	0.2179	38
BT9	0.2195	38
Method 2 (Molten-salt synthesis)		
BT10	0.3824	22
BT11	0.5255	16
BT12	0.4416	19
BT13	0.3686	22
BT14	0.4011	21
BT15	0.3408	24
BT16	0.3172	26
BT17	0.3108	27
BT18	0.3237	26

Figure 29 shows the X-ray diffraction patterns of $BaTiO_3$ nanoparticles synthesized at different reaction temperatures (180 ℃, 200 ℃ and 220 ℃) and reaction times (12 h, 18 h and 24 h) by the above-mentioned Method 3 (hydrothermal). As shown in Figure 29(a) and 29(c), a mixture of TiO_2 phase (shown by the triangle mark) and cubic $BaTiO_3$ phase was verified by XRD for the reaction temperature of 180 ℃ and reaction times of 12 h and 24 h. In contrast, no cubic barium titanate phase was obtained for the reaction time of 18 h, and all diffraction peaks corresponded to the TiO_2 phase, as demonstrated in Figure 29(b). When the reaction temperature was 200 °C (shown in Figure 29(d) – 29(f)), the diffraction peaks were indexed as (100), (110), (111), (200), (210), (211), (220), (300), (310) and (311) crystal planes, and a small amount of TiO_2 impurities was observed. For BT25 (synthesized at 220 °C for 12 h, shown in Figure 29(g)), the synthesized product was found to be a mixture of $BaTiO_3$ and TiO_2 phase. For BT26 (synthesized at 220 °C for 18 h, shown in Figure 29(h)), no $BaTiO_3$ phase was observed. The diffraction peaks were indexed to the barium titanium oxide phase ($Ba_6Ti_{17}O_{40}$, PDF#00-035-0817, shown by the circle mark) and to titanium oxide phase ($TiO_{1.25}$, PDF#01-078-5811, shown by the rhombus mark). For BT27 (220°C and 24h, shown in Figure 29(i)), no cubic $BaTiO_3$ phase was observed. The $BaTiO_3$ phase corresponded to a tetragonal phase (PDF#01-070-9164) with a small amount of barium titanium oxide phase (Ba_2TiO_4, PDF#01-075-0677, shown by the arrow mark).

Therefore, based on the above XRD results, Method 3 was not suitable to obtain $BaTiO_3$ nanoparticles. Impurities can be observed in all products, as shown in Figure 29(a) – 29(i) for BT19 – BT27 samples. The reason needs to be further investigated. However, by comparing Method 1 with Method 3, one possible reason can be proposed. The only difference between Method 1 and Method 3 is that in Method 3, 5 g of solid NaOH was replaced by 6 mL of 5 M NaOH solution, therefore less amount of NaOH (about 1.2 g) were used in Method 3. As a result, the reaction between different precursors ($Ba(NO_3)_2$, TiO_2 and NaOH) was incomplete, which results in the formation of impurities and by-products. Future studies can be focused on investigating how the amount of NaOH affects the formation of $BaTiO_3$ nanoparticles by Method 3.

According to the above XRD results (shown on Figures 26, 27 and 29) and discussion, $BaTiO_3$ nanoparticles with high crystallinity and purity can be successfully synthesized by Method 1 and Method 2.

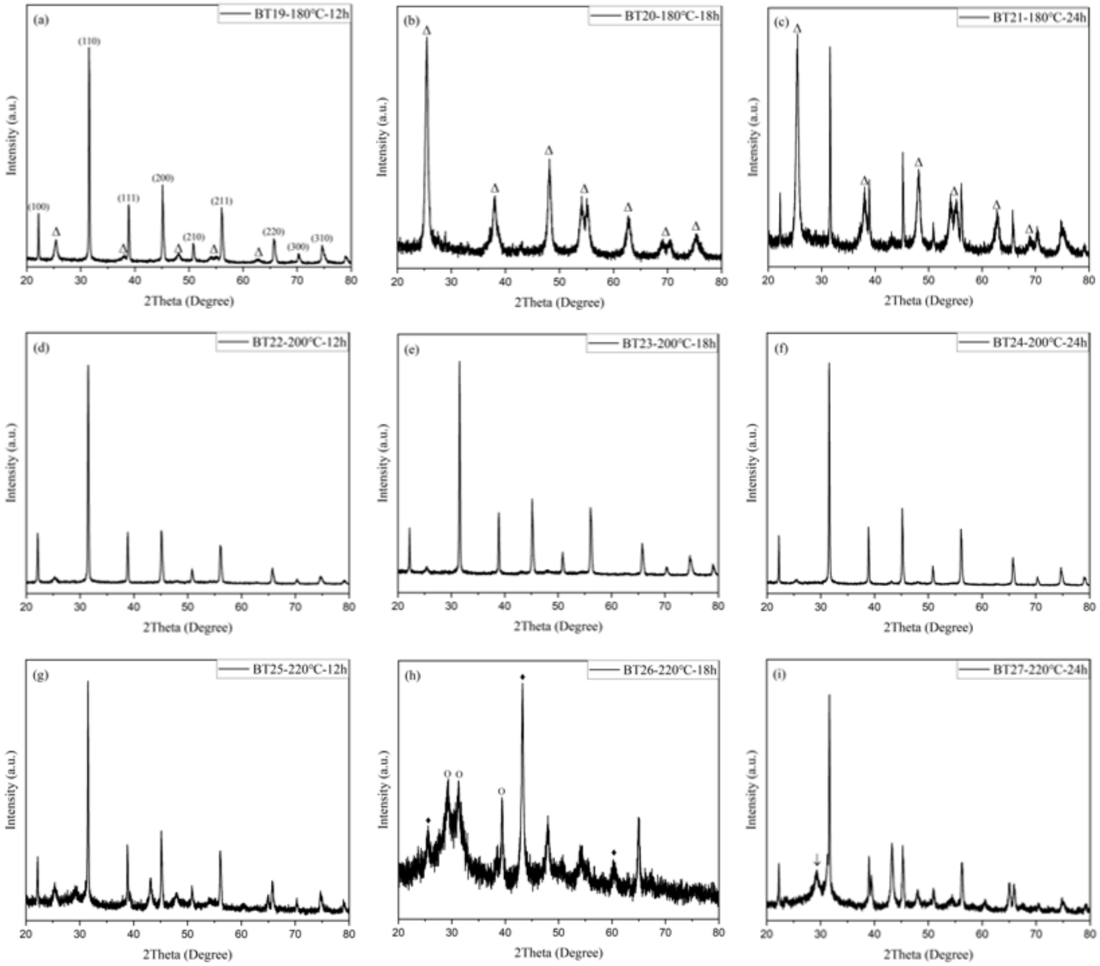

Figure 29: XRD results of $BaTiO_3$ powder (BT19 - BT27) synthesized by Method 3 (hydrothermal).

Figure 30 shows the X-ray diffraction patterns of $SrTiO_3$ powder synthesized at different reaction temperatures (180 ℃, 200 ℃ and 220 ℃) and times (12 h, 18 h and 24 h) by Method 1 (hydrothermal). All diffraction peaks were indexed as (100), (110), (111), (200), (210), (211), (220), (300) and (310) crystal planes which corresponds to the cubic perovskite $SrTiO_3$ phase (PDF#01-070-8508). No other peaks were observed which indicates the high purity of synthesized $SrTiO_3$ powder. From the diffraction patterns, by increasing the reaction time (as shown in Figure 30(a) – 30(c) and reaction temperature (as shown in Figure 30(d) – 30(f)), the width of diffraction peaks did not change accordingly, which indicates that the crystallite size of $SrTiO_3$ did not significantly depend on the reaction temperature and reaction time. The growth of $SrTiO_3$

crystallites has completed when the synthesis was conducted at the reaction temperature of 180 °C and reaction time of 12 h. Further increasing reaction time and reaction temperature did not significantly affect the growth of $SrTiO_3$ crystallites.

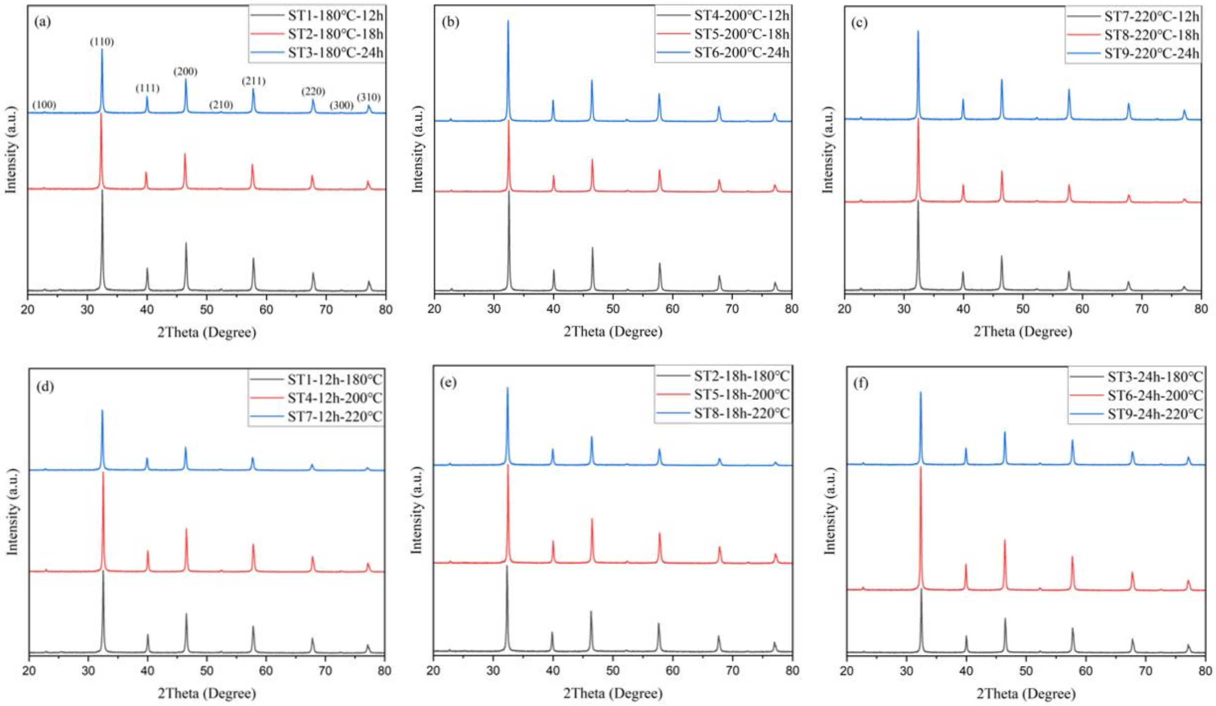

Figure 30: XRD results of $SrTiO_3$ powder (ST1 - ST9) synthesized by Method 1 (hydrothermal).

Figure 31 shows the X-ray diffraction patterns of $SrTiO_3$ powder synthesized at different reaction temperatures (180 °C, 200 °C and 220 °C) and reaction times (12 h, 18 h and 24 h) by Method 2 (molten-salt). From XRD results, the diffraction peaks can be indexed to the cubic perovskite $SrTiO_3$ phase (PDF#01-070-8508). However, the crystallinity of synthesized $SrTiO_3$ powder was found to be poor, especially for the low reaction temperature (180°C) and short reaction time (12 h), as shown in Figure 31(a). By increasing reaction temperature and time, the crystallinity improves, as verified in Figure 31(b) and 31(c). For example, by prolonging the reaction time to 24 h, while keeping the reaction temperature at 220 °C, the diffraction peaks of $SrTiO_3$ powder (ST18) became sharper than those of ST16 and ST17, which indicates the improvement of crystallinity, as shown in Figure 31(c). The same trend also applied to the reaction temperature, as shown in Figure 31(d) – 31(e). For example, by increasing the reaction temperature to 220℃, while keeping the reaction time (24h), the diffraction peaks of $SrTiO_3$ powder (ST18) became much sharper than those of ST12 and ST15, which indicates a significant crystallinity's improvements, as demonstrated on Figure 31(f). In addition, from the XRD results, the reaction temperature has a greater influence on the crystallinity of $SrTiO_3$ powder than the reaction time. Specifically, despite the short reaction time (for example 12h), the $SrTiO_3$ powder synthesized at higher reaction temperature (220 °C) have much better crystallinity than those synthesized at lower temperature (180 °C), see Figure 31(d). However, even if prolonging the reaction time to 24h, the crystallinity of the corresponding $SrTiO_3$ powder synthesized at low reaction temperature (180 °C) was still poor, see Figure 31(a).

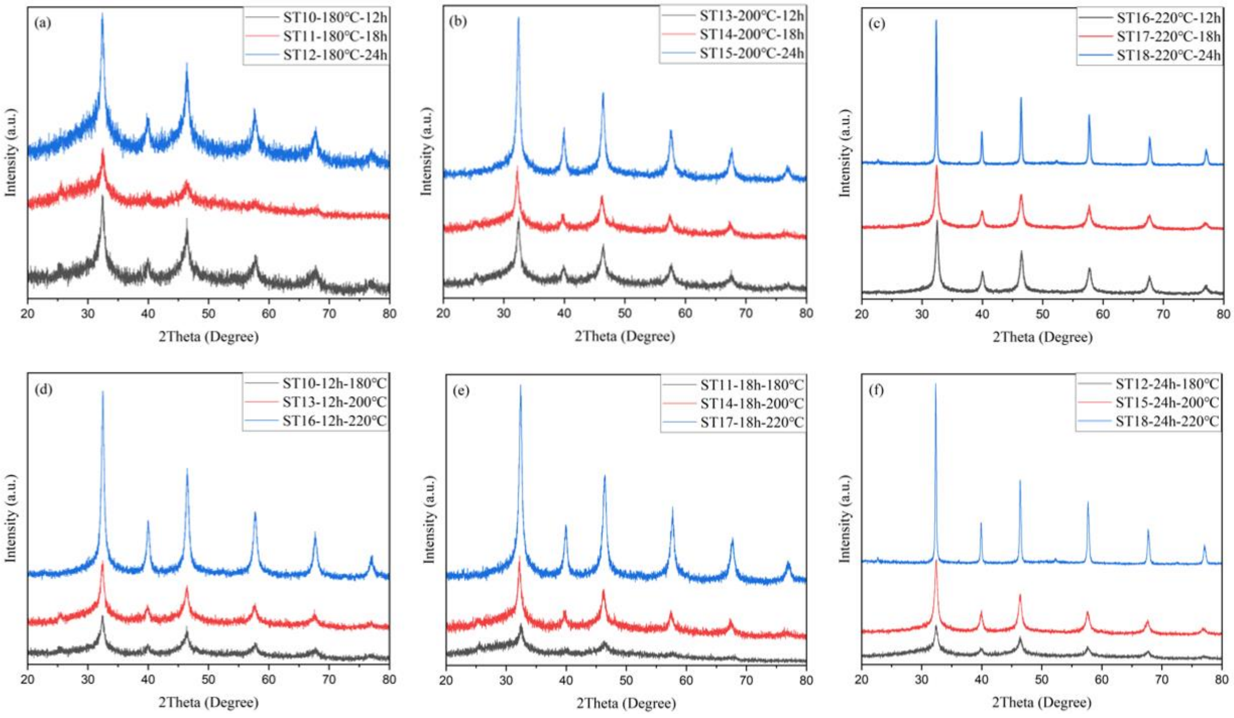

Figure 31: XRD results of $SrTiO_3$ powder (ST10 - ST18) synthesized by Method 2 (molten-salt).

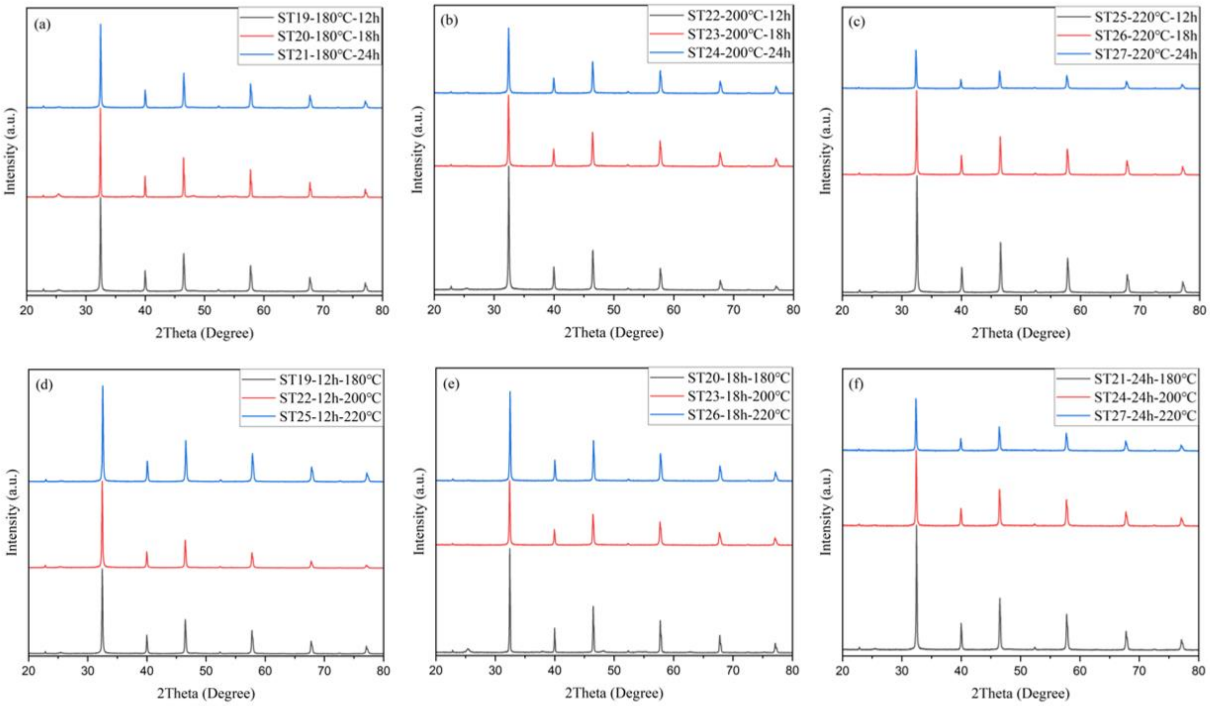

Figure 32: XRD results of $SrTiO_3$ powder (ST19 - ST27) synthesized by Method 3 (hydrothermal).

Figure 32 shows the X-ray diffraction patterns of $SrTiO_3$ powder synthesized at different reaction temperatures (180 ℃, 200 ℃ and 220 ℃) and time (12 h, 18 h and 24 h) by Method 3 (hydrothermal). All diffraction peaks were indexed as (100), (110), (111), (200), (210), (211), (220), (300) and (310) crystal planes which corresponds to the cubic perovskite $SrTiO_3$ phase (PDF#01-070-8508). When the reaction temperature was low (180 ℃) and reaction time was short (12 h), as shown in Figure 32(a) and Figure 32(d), a small amount of TiO_2 impurities were observed in the diffraction patterns, which indicates that the reaction was not complete due to the low reaction temperature and short reaction time. When prolonging the reaction time to 18 h or 24 h (as shown in Figure 32(b) and Figure 32(c)) and increasing the reaction temperature to 200 ℃ or 220 ℃ (as shown in Figure 32(e) and Figure 32(f)), no other peaks were observed which indicates the high purity of synthesized $SrTiO_3$ powder. Similar to the $SrTiO_3$ synthesized by Method 1, the width of diffraction peaks also does not change with changing the reaction temperature and time, which indicates the crystallite size of $SrTiO_3$ did not significantly change by increasing the reaction temperature and time.

In order to verify the above results that the size of $SrTiO_3$ crystallites synthesized by Method 1 and Method 3 did not significantly depend on the reaction temperature and reaction time (See Figure 30 and 32), the crystallite size of $SrTiO_3$ was calculated by using the above-mentioned Scherrer equation (shown in equation (1)). From Table 3, the crystallite size of $SrTiO_3$ material produced by Method 1 was in the range of 32 - 38 nm, while the crystallite size of $SrTiO_3$ synthesized by Method 3 was in the range of 41 - 46 nm (except for the size of ST20 sample which was found to be 54 nm). The corresponding standard deviations were calculated for $SrTiO_3$ crystallites synthesized by Method 1 and Method 3 at different reaction temperatures and reaction times, which were only 2 nm and 1 nm. These calculation results confirmed the conclusion that the size of synthesized $SrTiO_3$ nanoparticles did not significantly depend on the reaction temperature and reaction time.

By comparing the crystallite size between $SrTiO_3$ material synthesized through Method 1 and Method 3, Scherrer equation was applied to analyze the diffraction pattern. From Scherrer equation, small crystallites correspond to broader diffraction peaks [78]. Figure 33 shows the XRD results of $BaTiO_3$ nanoparticles synthesized by Method 1 and Method 3 at the same reaction time and reaction temperature. However, from Figure 33, the crystallite size difference of $SrTiO_3$ synthesized through Method 1 and Method 3 cannot be directly observed. In order to further verify the above discussion related to the influence of synthesis methods on the crystallite size of $SrTiO_3$, the crystallite size of $SrTiO_3$ material synthesized by Method 1 and Method 3 were compared based on the calculation results listed in Table 3. From Table 3, the smaller crystallite sizes of $SrTiO_3$ synthesized by Method 1 (32 - 38 nm) compared with the one produced by Method 3 (41

- 46 nm) was confirmed. Therefore, the crystallite size of $SrTiO_3$ synthesized by Method 1 and Method 3 follows the relationship of $SrTiO_{3\ (Method\ 1)} < SrTiO_{3\ (Method\ 3)}$. Based on the calculation results, $SrTiO_3$ with different crystallite sizes can be successfully synthesized by hydrothermal method. By only replacing 5 g of solid NaOH (in Method 1) with 6 mL 5M NaOH solution (in Method 3), $SrTiO_3$ with larger crystallite size can be successfully produced, which provided a convenient way to control the crystallite size of $SrTiO_3$.

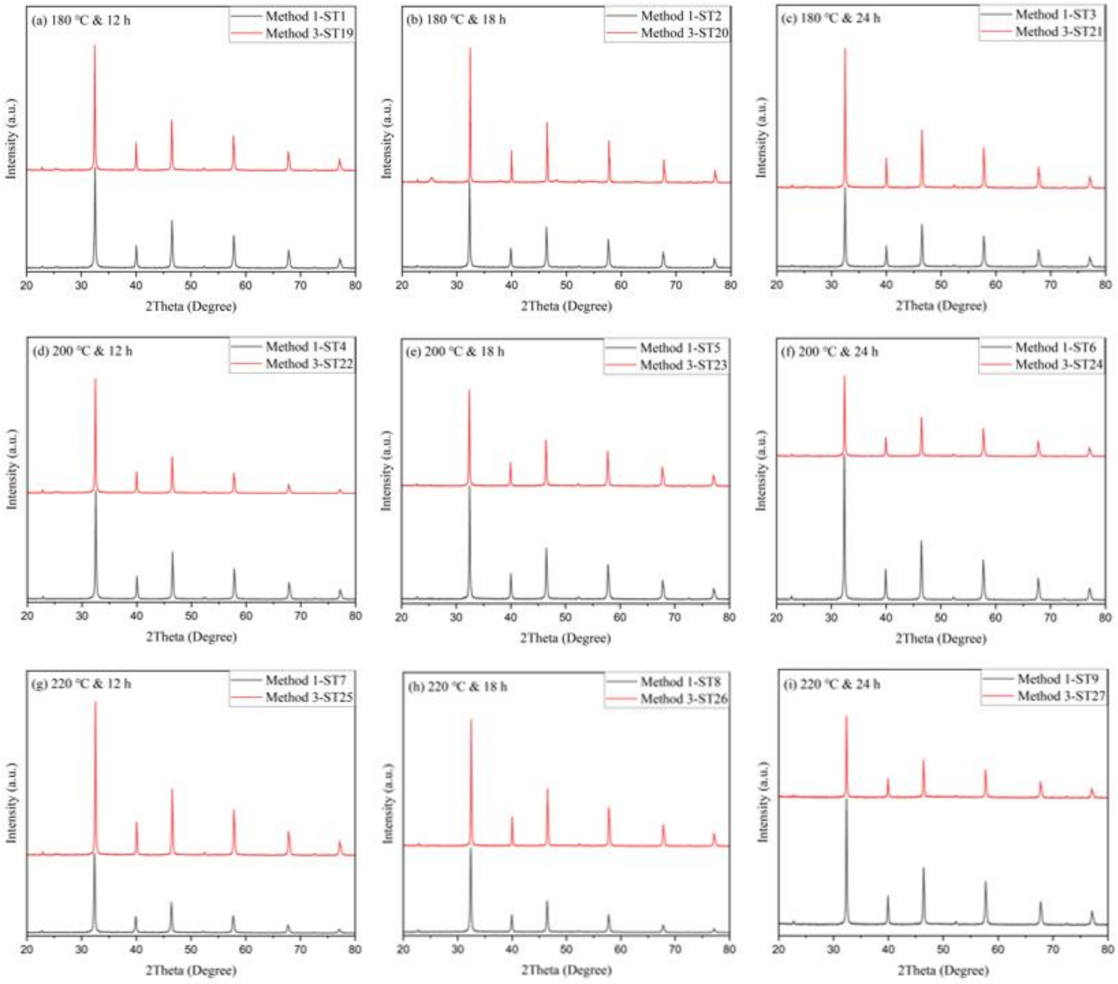

Figure 33: XRD results of $SrTiO_3$ powder synthesized by Method 1 and Method 3 under the same reaction temperature and reaction time.

Table 3: Calculation results of full width at half maximum (FWHM) and crystallite size of synthesized $SrTiO_3$.

Sample	FWHM	Crystallite size (nm)
Method 1 (Hydrothermal synthesis)		
ST1	0.2517	33
ST2	0.2310	36
ST3	0.2290	36
ST4	0.2241	37
ST5	0.2261	37
ST6	0.2237	37
ST7	0.2549	32
ST8	0.2559	32
ST9	0.2184	38
Method 3 (Hydrothermal synthesis)		
ST19	0.1914	43
ST20	0.1537	54
ST21	0.1814	46
ST22	0.1942	43
ST23	0.1969	42
ST24	0.1986	42
ST25	0.2011	41
ST26	0.1858	45
ST27	0.1874	44

According to the above XRD results (shown in Figures 30, 31 and 32) and discussion, $SrTiO_3$ powder with high crystallinity and purity can be successfully synthesized by Method 1 and Method 3. For Method 2, the reaction temperature needs to be controlled in order to get the appropriate phase for $SrTiO_3$ material. In addition, when the reaction temperature is low and reaction time is short, the synthesized $SrTiO_3$ powder have poor crystallinity. $SrTiO_3$ powder with high crystallinity and purity can only be obtained by Method 2 at the high reaction temperature (220 °C) and long reaction time (24 h), as shown on Figure 31(f).

3.2 SEM RESULTS

As previously mentioned, the $BaTiO_3$ powder with high crystallinity and purity can be successfully synthesized by Method 1 and Method 2. The $SrTiO_3$ powder with high crystallinity and purity can be successfully produced by Method 1 and Method 3. In order to investigate which synthesis method is suitable to get $BaTiO_3$ and $SrTiO_3$ nanocubes, scanning electron microscopy (SEM) was applied to determine the morphology of the obtained $BaTiO_3$ and $SrTiO_3$ nanoparticles.

Figure 34 shows the SEM images of $BaTiO_3$ crystallites (BT1 – BT9) synthesized by Method 1. From these SEM images, $BaTiO_3$ crystallites have elliptical or spherical shape. In addition, the small $BaTiO_3$ crystallites (see Figure 34) aggregated together to form large $BaTiO_3$ particles with multiple facets which have sizes larger than 500 nm, as shown on Figure 35.

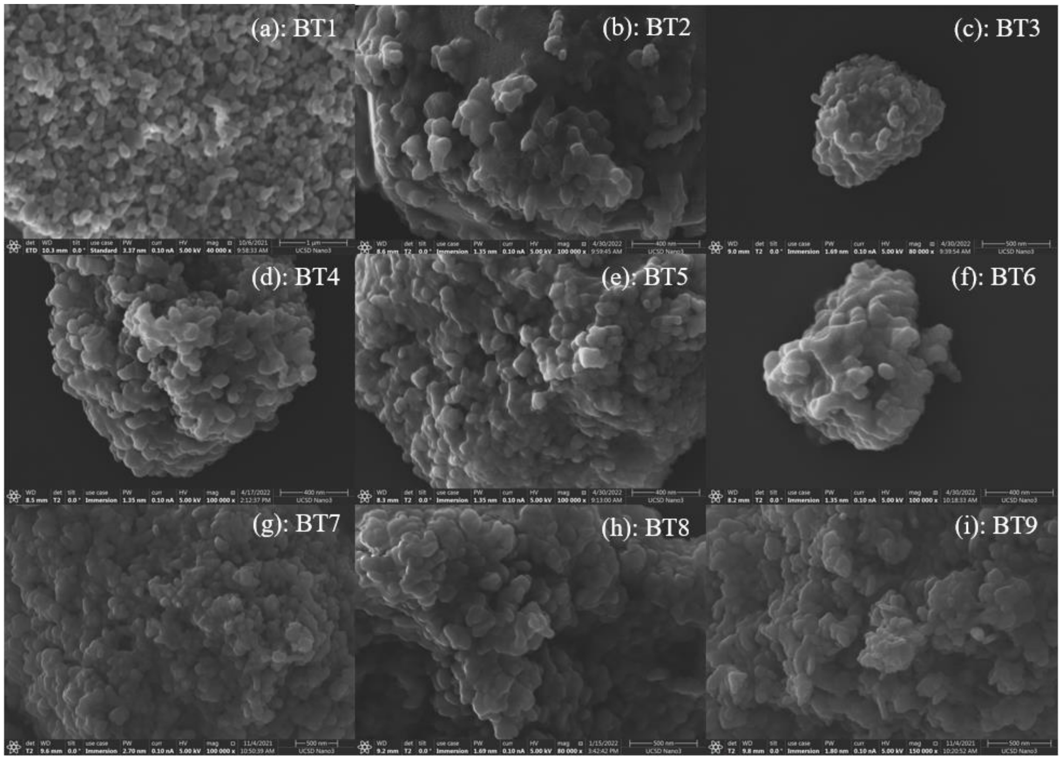

Figure 34: SEM images of $BaTiO_3$ crystallites (BT1 - BT9) synthesized by Method 1 (hydrothermal).

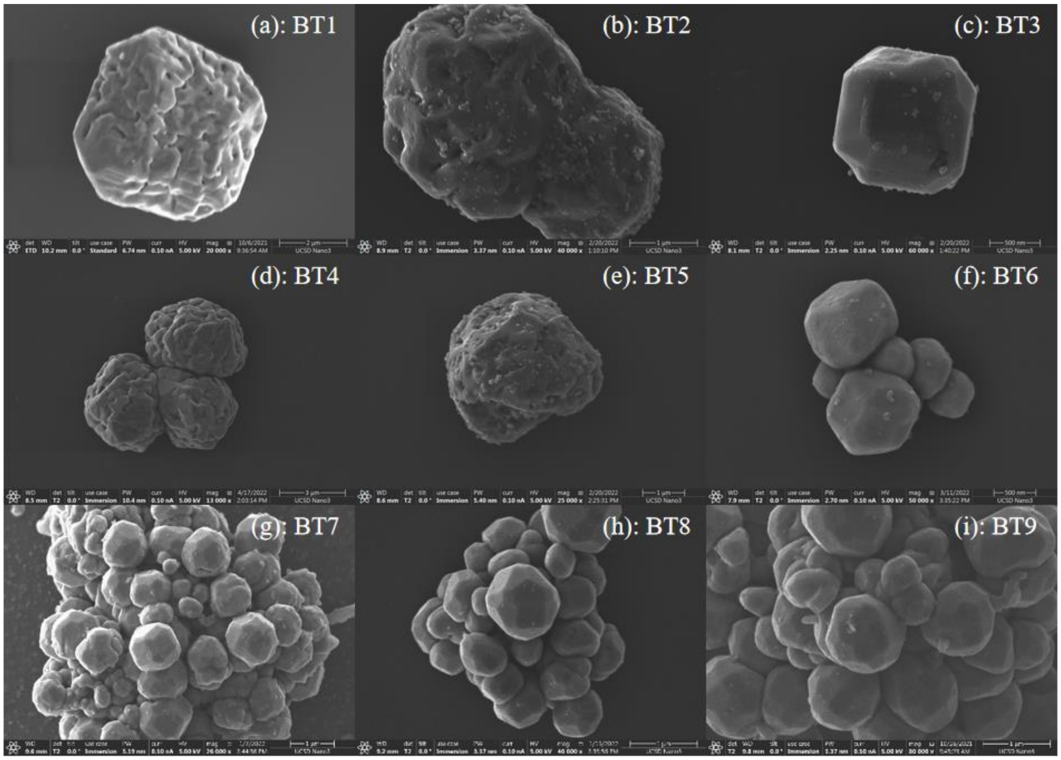

Figure 35: SEM images of large $BaTiO_3$ particles (BT1 - BT9) synthesized by Method 1 (hydrothermal).

Figure 36 shows the SEM images of $BaTiO_3$ crystallites (BT10 – BT18) synthesized by Method 2. From the SEM images shown in Figure 36, the reaction temperature and time affected the morphology of $BaTiO_3$ crystallites. When the reaction temperature was low (for example, for sample BT10 synthesized at 180 ℃ for 12 h), the crystallites have both spherical and cubic shape (see Figure 36(a)), and most crystallites were in spherical shape. By increasing the reaction temperature to 220 ℃, while keeping the same reaction time, crystallites only have cubic morphology, as shown in Figure 36(g) for BT16 sample. In addition, when the reaction time was short (for example, for BT10 sample synthesized at 180 ℃ for 12 h), most crystallites have spherical shape as shown in Figure 36(a). By increasing the reaction time to 24 h, while keeping the same reaction temperature, crystallites (BT12) only have cubic morphology (see Figure 36(c)). Based on the above discussion, higher reaction temperature and longer reaction time can facilitate the formation of $BaTiO_3$ nanocubes. Therefore, the best reaction temperature and time for getting the $BaTiO_3$ nanocubes were found to be 220 ℃ and 24 h (as shown on Figure 36(i)). Different from the $BaTiO_3$ crystallites synthesized by Method 1, no large particles (≥ 500 nm) were obtained by Method 2, most probably because the molten salt (mixture of NaOH and KOH) was used as solvent for Method 2. The highly viscous solvent will decrease the mobility of small crystallites, which restricts the formation of large particles [70].

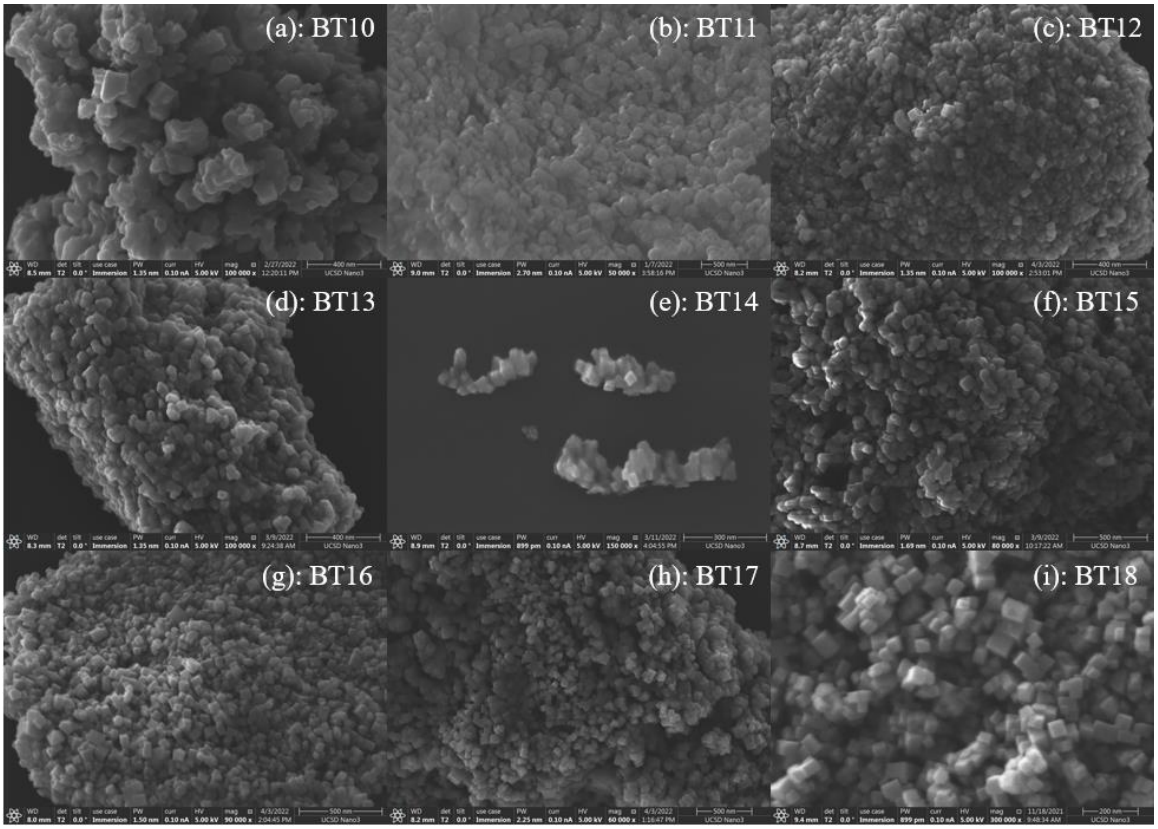

Figure 36: SEM images of $BaTiO_3$ nanoparticles (BT10 - BT18) synthesized by Method 2 (molten-salt).

Based on the above SEM images (shown on Figure 34 and 36) and previous XRD results (see Figure 26 and 27), $BaTiO_3$ crystallites can be successfully synthesized by Method 1 and Method 2. However, in order to get $BaTiO_3$ crystallites with cubic morphology, Method 2 is a promising way. In addition, the best reaction temperature and reaction time to obtain $BaTiO_3$ nanocubes by Method 2 are 220 ℃ and 24 h.

Figure 37 shows the SEM images of $SrTiO_3$ crystallites (ST1 – ST9) synthesized by Method 1. From SEM images, $SrTiO_3$ crystallites have cubic morphology. In addition, the small $SrTiO_3$ crystallites aggregated together to form large $SrTiO_3$ cubic particles which have sizes larger than 500 nm, as shown in Figure 38.

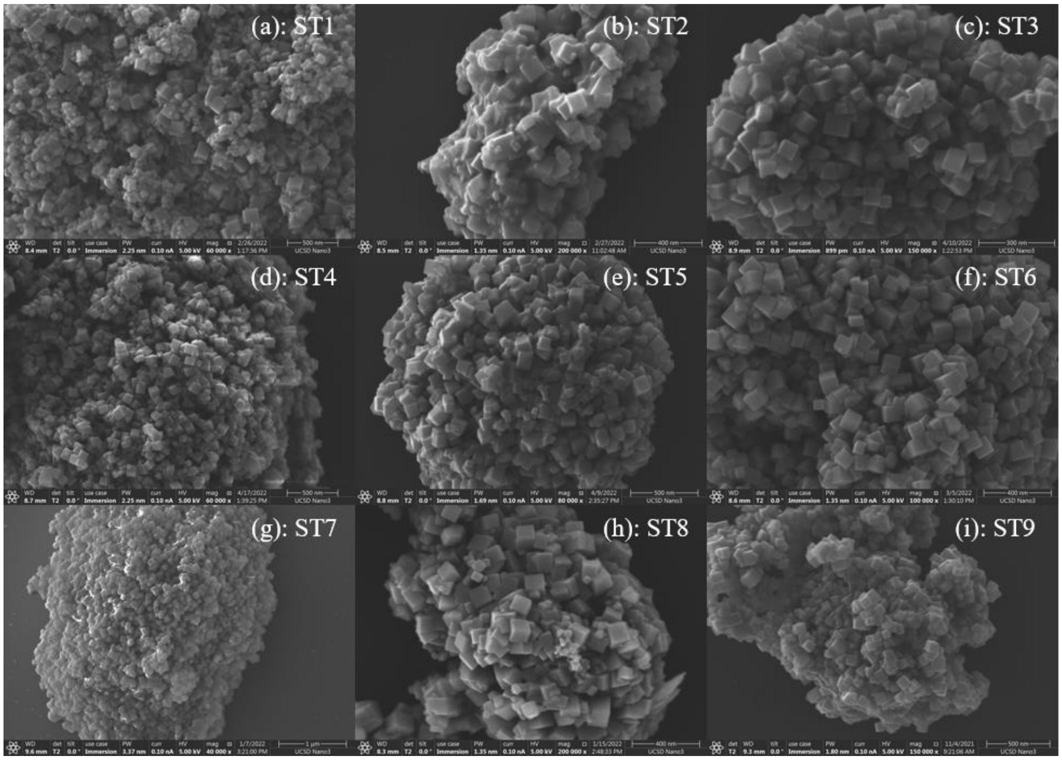

Figure 37: SEM images of $SrTiO_3$ crystallites (ST1 - ST9) synthesized by Method 1 (hydrothermal).

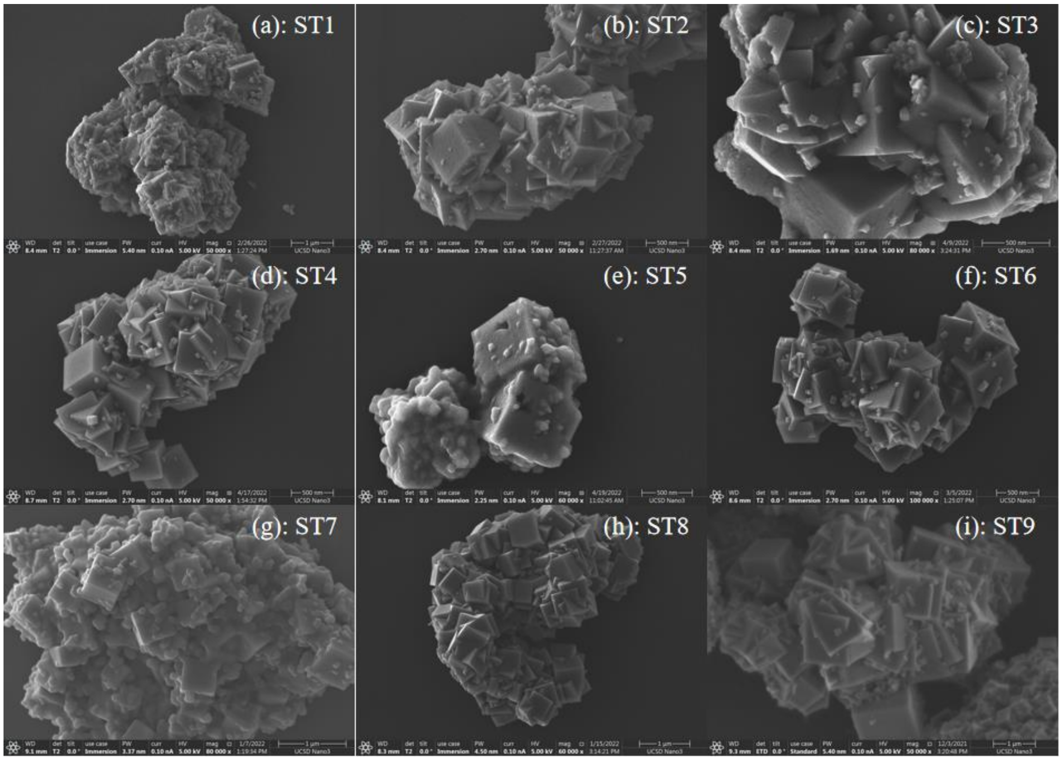

Figure 38: SEM images of large $SrTiO_3$ cubic particles (ST1 - ST9) synthesized by Method 1 (hydrothermal).

Figure 39 shows the SEM images of $SrTiO_3$ crystallites (ST19 – ST27) synthesized by Method 3. $SrTiO_3$ crystallites shown on this Figure have cubic morphology. Also, the small $SrTiO_3$ nanoparticles aggregated together to form large cubic particles by face-to-face attachment, as shown on Figure 40.

Based on the above SEM images (shown in Figure 37 and 39) and previous XRD results (see Figures 28 and 30), $SrTiO_3$ nanocubes can be successfully synthesized by using Method 1 and Method 3. The only difference between $SrTiO_3$ nanocubes synthesized by using Method 1 and method 3 is the size of $SrTiO_3$ nanocubes. $SrTiO_3$ nanocubes synthesized by using method 1 have smaller size (32 - 38 nm from Table 3) than those synthesized by using method 3 (41 - 46 nm from Table 3), which also provides a promising way to modify the size of $SrTiO_3$ nanocubes.

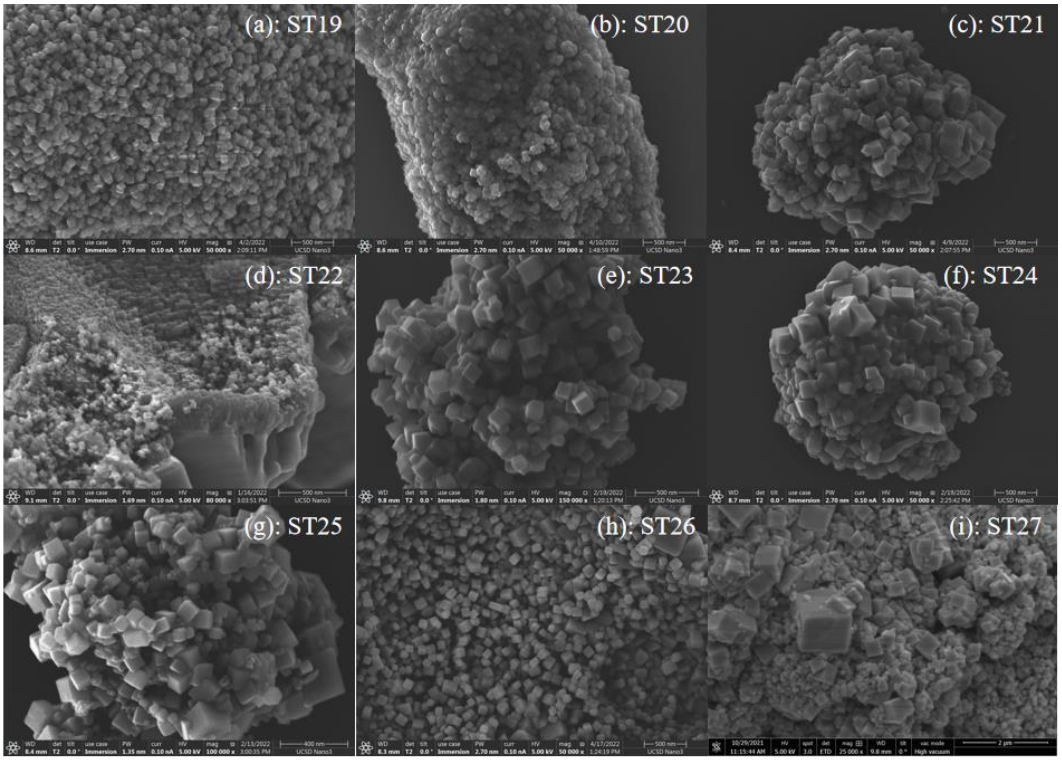

Figure 39: SEM images of $SrTiO_3$ nanoparticles (ST19 - ST27) synthesized by Method 3 (hydrotheraml).

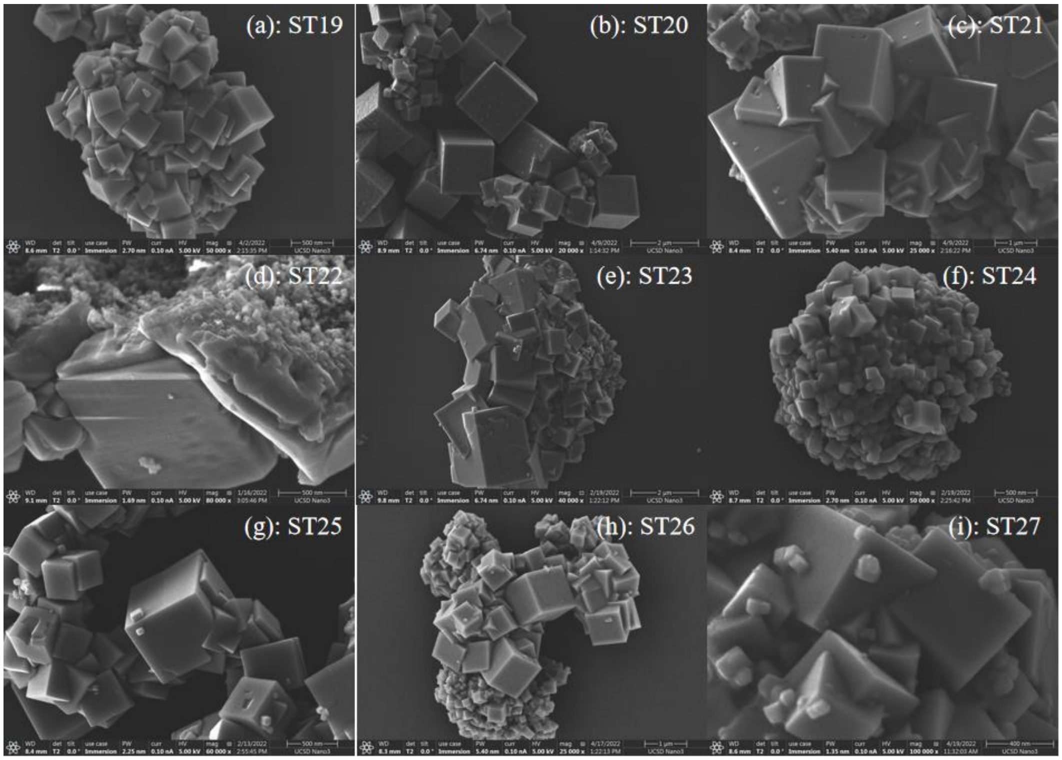

Figure 40: SEM images of large $SrTiO_3$ cubic particles (ST19 - ST27) synthesized by Method 3 (hydrothermal).

However, Method 1 and Method 3 have a common problem of a formation of large $SrTiO_3$ cubic particles from smaller ones (as shown in Figures 38 and 40), which is not the main for this thesis goal (to get $SrTiO_3$ crystallite with cubic morphology, see Figures 37 and 39). One reason for the formation of these large $SrTiO_3$ cubic particles is that, according to the Derjaguin-Landau-Verwey-Overbeak (DLVO) theory, the interaction energy barrier decreases with decreasing particle size, which leads to a high attachment efficiency [79]. As a result, the small nanocubes will tend to form large particles. Another reason for this formation can be explained by the high surface energy possessed by the small nanocubes [80]. As a result, to decrease the overall surface energy, small nanocubes will form large particles.

Reaction temperature and time will also affect the formation of large $SrTiO_3$ cubic particles. By increasing the reaction temperature, the random kinetic energy increases and the interaction energy barrier deceases which both significantly increase the aggregation rate [81]–[83]. Therefore, the small $SrTiO_3$ nanocubes can easily form large particles. By increasing the reaction time, small $SrTiO_3$ nanocubes will have sufficient time to collide with each other, which increases the opportunity of successful attachment, which also results in the formation of large $SrTiO_3$ cubic particles.

In order to restrict the formation of large particles and only get small $SrTiO_3$ nanocubes, one promising way is to decrease the reaction temperature and use a relatively short reaction time. Another promising way is to use capping agents which can modify the surfaces and decease the surface energy of $SrTiO_3$ nanocubes. Therefore, further studies can be focused on the identification of the lowest reaction temperature and the shortest reaction time as well as finding the suitable capping agents, by which the small $SrTiO_3$ nanocubes can be successfully.

3.3 TEM RESULTS AND FORMATION MECHANISM OF BARIUM AND STRONTIUM TITANATE NANOCUBES

Based on the SEM images (Figure 36) and XRD results (Figure 27), $BaTiO_3$ nanocubes can be successfully synthesized by Method 2 (Molten-salt synthesis). $SrTiO_3$ nanocubes can be successfully synthesized by Method 1 and 3 (Hydrothermal synthesis), according to the SEM (see Figure 37 and 39) and XRD results (see Figure 30 and 32). In order to investigate the underlying formation mechanism of $BaTiO_3$ and $SrTiO_3$ nanocubes, TEM was applied to obtain the TEM and HRTEM images, as well as the electron diffraction patterns, of $BaTiO_3$ and $SrTiO_3$ nanocubes.

Figure 41 shows the TEM image, HRTEM image and electron diffraction pattern of a single $BaTiO_3$ nanocube (sample BT18, synthesized by Method 2 at 220 ℃ for 24h). From TEM image (shown on Figure 41(a)), the cubic morphology can be clearly observed, which further confirms SEM results (see Figure 36(i)). From the high-resolution TEM image (see Figure 41(b)), the d-spacing was calculated by using ImageJ software. The calculation result of d-spacing is 4.054 Å which corresponds to the (100) crystal plane. The electron diffraction pattern, shown on Figure 41(c), is obtained from [001] zone axis, and indexed as (100), (110), (200), (210) and (220) crystal planes, which confirms the cubic structure of synthesized $BaTiO_3$ material. The above TEM results confirmed that the $BaTiO_3$ nanocubes can be successfully synthesized by using molten-salt method.

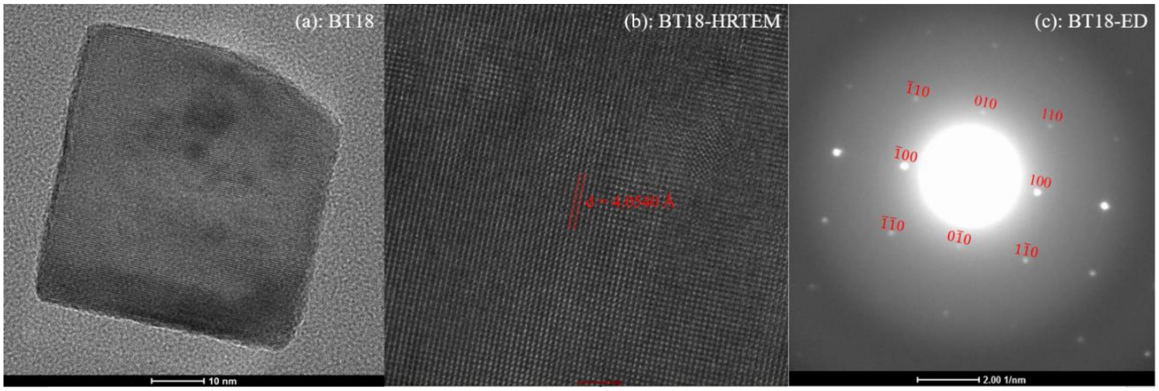

Figure 41: TEM image, HRTEM image and electron diffraction pattern of a single $BaTiO_3$ nanocube (sample BT18, synthesized by Method 2 at 220 °C for 24h).

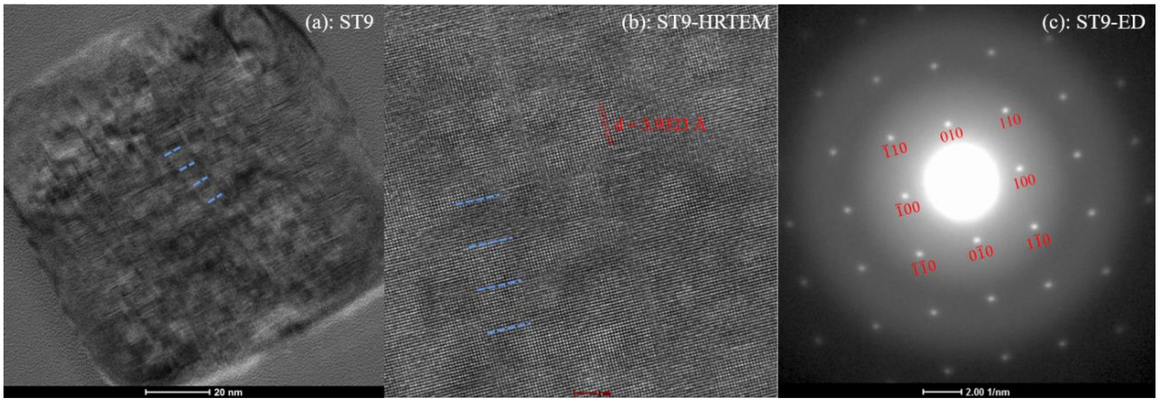

Figure 42: TEM image, HRTEM image and electron diffraction pattern of a single $SrTiO_3$ nanocube (ST9, synthesized by Method 1 at 220 °C for 24h).

Figure 42 shows the TEM image, HRTEM image and electron diffraction pattern of a single $SrTiO_3$ nanocube (sample ST9, synthesized by Method 1 at 220 °C for 24h). The $SrTiO_3$ nanocube can be clearly observed from Figure 42(a). From the high-resolution TEM image (see

Figure 42(b)), the d-spacing was calculated to be 3.9323 Å which corresponds to the (100) crystal plane. The electron diffraction pattern is obtained from [001] zone axis, and indexed to (100), (110), (200), (210) and (220) crystal planes, which confirms the cubic structure of synthesized $SrTiO_3$ nanocubes. These TEM results verified that the $SrTiO_3$ nanocubes can be successfully synthesized by using hydrothermal method.

Based on the TEM characterization results and previously mentioned formation mechanisms of metal oxide nanocubes in the Introduction section [40], [47], [50], the formation mechanisms for $BaTiO_3$ and $SrTiO_3$ nanocubes were proposed. Based on the Wulff construction theory [84], the final morphology of the equilibrium nanoparticles is determined by the surface energy of exposed crystal facets. Crystal planes with low surface energy are preferred than crystal planes with high surface energy. For cubic morphology, the surface energy has relationship of $\gamma_{\{100\}} < \gamma_{\{111\}} < \gamma_{\{110\}}$. Therefore, {100} crystal planes are preferred crystal growth planes, which will minimize the overall surface energy of the final nanocubes. From the previous HRTEM images (see Figure 41(b) and 42(b)), the d-spacing is correspond to {100} crystal planes for both $BaTiO_3$ and $SrTiO_3$ nanocubes, which confirms that the {100} crystal planes are preferred crystal growth planes in the crystal growth stage.

Figure 43 shows the schematic representation of the proposed formation mechanisms of $BaTiO_3$ and $SrTiO_3$ nanocubes. In the case of $BaTiO_3$, the small spherical nuclei will first form through nucleation. Next, the growth of {100} crystal planes will result in the final $BaTiO_3$ nanocubes. However, for $SrTiO_3$, the first step is the formation of small spherical nuclei. Further growth of {100} crystal planes will result in the small $SrTiO_3$ nanocubes. The final nanocube is formed by the face-to-face attachment of small $SrTiO_3$ nanocubes, which can be confirmed from Figure 42 (a) and 42(b). From the HRTEM image of the single $SrTiO_3$ nanocube (see the blue dashed lines on Figure 42 (a) and 42(b)), the small steps, which indicates the small $SrTiO_3$ nanocubes, can be clearly observed, which confirms the face-to-face attachment of small $SrTiO_3$ nanocubes. From previous SEM images, shown in Figure 39(d) and 40 (d) for ST22, the large $SrTiO_3$ cubic particles were formed by the aggregation of small $SrTiO_3$ nanocubes by face-to-face attachment through {100} crystal planes, which also confirms the proposed formation mechnism of $SrTiO_3$ nanocubes.

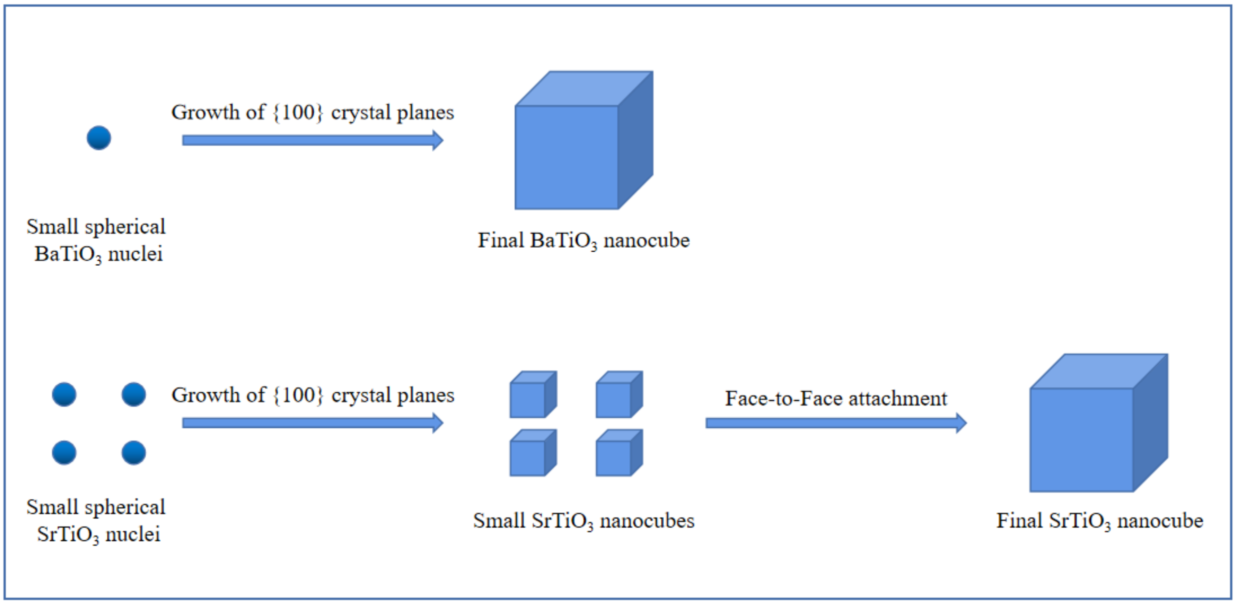

Figure 43: Proposed formation mechanisms of $BaTiO_3$ and $SrTiO_3$ nanocubes.

CHAPTER 4 CONCLUSIONS

In this thesis, different synthesis methods (Methods 1, 2 and 3) were used to investigate how to obtain $BaTiO_3$ and $SrTiO_3$ nanocubes. Based on the XRD and SEM results, $BaTiO_3$ nanocubes can be successfully synthesized by Method 2, and the size of obtained $BaTiO_3$ nanocubes was in the range of 21 - 27 nm.

In addition, Method 1 and Method 3 can be used to successfully synthesize $SrTiO_3$ nanocubes. The size of $SrTiO_3$ nanocubes synthesized by Method 1 was in the range of 32 - 38 nm, while the size of $SrTiO_3$ nanocubes obtained by Method 3 was in the range of 41 - 46 nm.

The influence of reaction conditions on the morphology and size of synthesized $BaTiO_3$ and $SrTiO_3$ nanocubes were also discussed. Based on the XRD and SEM results, the size of $BaTiO_3$ nanocubes did not significantly depend on the reaction time and reaction temperature. However, the morphology of $BaTiO_3$ nanocubes was affected by the reaction time and reaction temperature. Specifically, when the reaction time was short (12 h) and reaction temperature was low (180 ℃), the obtained product was a mixture of the spherical and cubic $BaTiO_3$ nanoparticles. By increasing the reaction temperature and reaction time, only $BaTiO_3$ nanocubes can be synthesized.

For $SrTiO_3$ nanocubes, the size and morphology did not depend on the reaction temperature and reaction time. However, the size of $SrTiO_3$ nanocubes depends on the synthesis method. $SrTiO_3$ nanocubes synthesized by Method 1 (32 - 38 nm) was smaller than those obtained by Method 3 (41 - 46 nm). These results are important for the future studies on the size-property and morphology-property relationships, since as was shown previously, ferroelectric, paraelectric and dielectric properties of $SrTiO_3$ and $BaTiO_3$ nanocubes significantly depend on the size and morphology of $SrTiO_3$ and $BaTiO_3$ nanocubes.

TEM results further confirm the formation of $BaTiO_3$ and $SrTiO_3$ nanocubes. Based on the TEM results and Wulff construction theory, formation mechanisms for both barium titanate and strontium titanate nanocubes were discussed. The cubic morphology was formed through the growth of {100} crystal planes, which will minimize the overall surface energy of the final products. This formation mechanism is important because the formation of $SrTiO_3$ and $BaTiO_3$ nanocubes discussed in this thesis was not influenced by any capping agent.

Based on the XRD, SEM and TEM results, it was verified that the $SrTiO_3$ and $BaTiO_3$ nanocubes with high purity can be successfully synthesized by molten-salt method and hydrothermal method without capping agents. Future studies can be focused on investigating the synthesis of other metal oxide nanocubes by using the synthesis methods and formation mechanisms proposed in this thesis.

REFERENCES

[1] M. Fernandez and J. Rodriguez, “Metal Oxide Nanoparticles Marcos,” *Nanomaterials: Inorganic and Bioinorganic Perspectives*, no. 10, 2007.

[2] M. E. Franke, T. J. Koplin, and U. Simon, “Metal and metal oxide nanoparticles in chemiresistors: Does the nanoscale matter?,” *Small*, vol. 2, no. 1. 2006. doi: 10.1002/smll.200500261.

[3] M. S. Chavali and M. P. Nikolova, “Metal oxide nanoparticles and their applications in nanotechnology,” *SN Applied Sciences*, vol. 1, no. 6. 2019. doi: 10.1007/s42452-019-0592-3.

[4] M. P. Nikolova and M. S. Chavali, “Metal oxide nanoparticles as biomedical materials,” *Biomimetics*, vol. 5, no. 2. 2020. doi: 10.3390/BIOMIMETICS5020027.

[5] Y. M. Chiang, E. B. Lavik, I. Kosacki, H. L. Tuller, and J. Y. Ying, “Nonstoichiometry and Electrical Conductivity of Nanocrystalline CeO2-x,” *Journal of Electroceramics*, vol. 1, no. 1, 1997, doi: 10.1023/a:1009934829870.

[6] J. Wu, “Broadband efficiency enhancement in quantum dot solar cells coupled with multispiked plasmonic nanostars,” *Nano Energy*, vol. 13, 2015, doi: 10.1016/j.nanoen.2015.02.012.

[7] S. AlYahya, “Size dependent magnetic and antibacterial properties of solvothermally synthesized cuprous oxide (Cu2O) nanocubes,” *Journal of Materials Science: Materials in Electronics*, vol. 29, no. 20, pp. 17622–17629, Oct. 2018, doi: 10.1007/s10854-018-9865-7.

[8] W. E. Mahmoud, F. Al-Hazmi, F. Al-Noaiser, A. A. Al-Ghamdi, and L. M. Bronstein, “A facile method to syntheses monodisperse γ-Fe2O 3 nanocubes with high magnetic anisotropy density,” *Superlattices and Microstructures*, vol. 68, pp. 1–5, Apr. 2014, doi: 10.1016/j.spmi.2014.01.009.

[9] Z. P. Chen, W. Q. Fang, B. Zhang, and H. G. Yang, “High-yield synthesis and magnetic properties of ZnFe2O 4 single crystal nanocubes in aqueous solution,” *Journal of Alloys and Compounds*, vol. 550, pp. 348–352, Feb. 2013, doi: 10.1016/j.jallcom.2012.10.105.

[10] M. Ravichandran and S. Velumani, “Manganese ferrite nanocubes as an MRI contrast agent,” *Materials Research Express*, vol. 7, no. 1, 2020, doi: 10.1088/2053-1591/ab66a4.

[11] H. Yang, T. Ogawa, D. Hasegawa, and M. Takahashi, “Synthesis and magnetic properties of monodisperse magnetite nanocubes,” in *Journal of Applied Physics*, 2008, vol. 103, no. 7. doi: 10.1063/1.2833820.

[12] F. Y. Jiang, C. M. Wang, Y. Fu, and R. C. Liu, “Synthesis of iron oxide nanocubes via microwave-assisted solvolthermal method,” *Journal of Alloys and Compounds*, vol. 503, no. 2. Elsevier Ltd, Jul. 23, 2010. doi: 10.1016/j.jallcom.2010.05.020.

[13] Q. Song and Z. J. Zhang, “Shape Control and Associated Magnetic Properties of Spinel Cobalt Ferrite Nanocrystals,” *J Am Chem Soc*, vol. 126, no. 19, pp. 6164–6168, May 2004, doi: 10.1021/ja049931r.

[14] A. Sathya, “CoxFe3-xO4 Nanocubes for Theranostic Applications: Effect of Cobalt Content and Particle Size,” *Chemistry of Materials*, vol. 28, no. 6, pp. 1769–1780, Mar. 2016, doi: 10.1021/acs.chemmater.5b04780.

[15] W. E. M. Elsayed, F. S. Al-Hazmi, L. S. Memesh, and L. M. Bronstein, “A novel approach for rapid green synthesis of nearly mono-disperse iron oxide magnetic nanocubes with remarkable surface magnetic anisotropy density for enhancing hyperthermia performance,” *Colloids and Surfaces A: Physicochemical and Engineering Aspects*, vol. 529, pp. 239–245, Sep. 2017, doi: 10.1016/j.colsurfa.2017.06.008.

[16] S. F. Situ-Loewenstein, “A novel synthetic route for high-index faceted iron oxide concave nanocubes with high T2 relaxivity for in vivo MRI applications,” *Journal of Materials Science: Materials in Medicine*, vol. 29, no. 5, May 2018, doi: 10.1007/s10856-018-6052-6.

[17] T. J. Fisher, Y. Zhou, T. S. Wu, M. Wang, Y. L. Soo, and C. L. Cheung, “Structure-activity relationship of nanostructured ceria for the catalytic generation of hydroxyl radicals,” *Nanoscale*, vol. 11, no. 10, pp. 4552–4561, Mar. 2019, doi: 10.1039/c8nr09393h.

[18] M. Alhumaimess, O. Aldosari, H. Alshammari, M. M. Kamel, M. A. Betiha, and H. M. A. Hassan, “Ionic liquid green synthesis of CeO 2 nanorods and nano-cubes: Investigation of the shape dependent on catalytic performance,” *Journal of Molecular Liquids*, vol. 279, pp. 649–656, Apr. 2019, doi: 10.1016/j.molliq.2019.02.014.

[19] H. He, “Controllable synthesis, characterization, and CO oxidation activity of CeO2 nanostructures with various morphologies,” *Ceramics International*, vol. 42, no. 6, pp. 7810–7818, May 2016, doi: 10.1016/j.ceramint.2016.02.005.

[20] X. Hao, “Atomic-Scale Valence State Distribution inside Ultrafine CeO2 Nanocubes and Its Size Dependence,” *Small*, vol. 14, no. 42, Oct. 2018, doi: 10.1002/smll.201802915.

[21] Y. Hu, W. Zhang, and W. Pan, “Photocatalytic activities of hydrothermally synthesized In(OH)3 and In2O3 nanocubes,” *Materials Research Bulletin*, vol. 48, no. 2, pp. 668–671, Feb. 2013, doi: 10.1016/j.materresbull.2012.11.029.

[22] L. Meng, D. Jiang, C. Xing, X. Lü, and M. Chen, “Synthesis and size-dependent electrochemical nonenzymatic H2O2 sensing of cuprous oxide nanocubes,” *RSC Advances*, vol. 5, no. 100, pp. 82496–82502, Sep. 2015, doi: 10.1039/c5ra14373j.

[23] M. P. Chavhan, S. Som, and C. H. Lu, “Size-controlled ceria nanocubes obtained via hydrothermal route for electrochemical capacitors,” *Materials Letters*, vol. 257, Dec. 2019, doi: 10.1016/j.matlet.2019.126598.

[24] G. M. Lyu, “Hydrophilic CeO2 nanocubes protect pancreatic β-cell line INS-1 from H2O2-induced oxidative stress,” *Nanoscale*, vol. 8, no. 15, pp. 7923–7932, Apr. 2016, doi: 10.1039/c6nr00826g.

[25] G. S. Jang, S. Ameen, M. S. Akhtar, and H. S. Shin, “Cobalt oxide nanocubes as electrode material for the performance evaluation of electrochemical supercapacitor,” *Ceramics International*, vol. 44, no. 1, pp. 588–595, Jan. 2018, doi: 10.1016/j.ceramint.2017.09.217.

[26] F. Hu, T. Liu, J. Pang, Z. Chu, and W. Jin, “Facile preparation of porous Co3O4 nanocubes for directly screen-printing an ultrasensitive glutamate biosensor microchip,” *Sensors and Actuators, B: Chemical*, vol. 306, Mar. 2020, doi: 10.1016/j.snb.2019.127587.

[27] T. T. D. Nguyen, H. N. Choi, M. J. Ahemad, D. van Dao, I. H. Lee, and Y. T. Yu, “Hydrothermal synthesis of In2O3 nanocubes for highly responsive and selective ethanol gas sensing,” *Journal of Alloys and Compounds*, vol. 820, Apr. 2020, doi: 10.1016/j.jallcom.2019.153133.

[28] S. S. Parizi, A. Mellinger, and G. Caruntu, “Ferroelectric barium titanate nanocubes as capacitive building blocks for energy storage applications,” *ACS Applied Materials and Interfaces*, vol. 6, no. 20, pp. 17506–17517, Oct. 2014, doi: 10.1021/am502547h.

[29] Z. Yang, Y. Huang, J. Hu, L. Xiong, H. Luo, and Y. Wan, “Nanocubic CoFe2O4/graphene composite for superior lithium-ion battery anodes,” *Synthetic Metals*, vol. 242, pp. 92–98, Aug. 2018, doi: 10.1016/j.synthmet.2018.05.010.

[30] X. Zhang, “NiFe2O4 nanocubes anchored on reduced graphene oxide cryogel to achieve a 1.8 V flexible solid-state symmetric supercapacitor,” *Chemical Engineering Journal*, vol. 360, pp. 171–179, Mar. 2019, doi: 10.1016/j.cej.2018.11.206.

[31] J. H. Fendler, “Chemical self-assembly for electronic applications,” *Chemistry of Materials*, vol. 13, no. 10. 2001. doi: 10.1021/cm010165m.

[32] V. Polshettiwar, B. Baruwati, and R. S. Varma, “Self-assembly of metal oxides into three-dimensional nanostructures: Synthesis and application in catalysis,” *ACS Nano*, vol. 3, no. 3, 2009, doi: 10.1021/nn800903p.

[33] G. Guo, “Self-assembly of transition-metal-oxide nanoparticle supraparticles with designed architectures and their enhanced lithium storage properties,” *Journal of Materials Chemistry A*, vol. 4, no. 41, 2016, doi: 10.1039/c6ta07184h.

[34] K. C. Barick and D. Bahadur, “Self-assembly of colloidal nanoscale particles: Fabrication, properties and applications,” in *Journal of Nanoscience and Nanotechnology*, 2010, vol. 10, no. 2. doi: 10.1166/jnn.2010.1734.

[35] D. Caruntu, T. Rostamzadeh, T. Costanzo, S. Salemizadeh Parizi, and G. Caruntu, "Solvothermal synthesis and controlled self-assembly of monodisperse titanium-based perovskite colloidal nanocrystals," *Nanoscale*, vol. 7, no. 30, pp. 12955–12969, Aug. 2015, doi: 10.1039/c5nr00737b.

[36] S. O'Brien, L. Brus, and C. B. Murray, "Synthesis of monodisperse nanoparticles of barium titanate: Toward a generalized strategy of oxide nanoparticle synthesis," *Journal of the American Chemical Society*, vol. 123, no. 48. pp. 12085–12086, Dec. 05, 2001. doi: 10.1021/ja011414a.

[37] J. Miao, C. Hu, H. Liu, and Y. Xiong, "BaTiO3 nanocubes: Size-selective formation and structure analysis," *Materials Letters*, vol. 62, no. 2, pp. 235–238, Jan. 2008, doi: 10.1016/j.matlet.2007.05.009.

[38] X. Zhu, "TEM characterization and Raman spectra of hydrothermal BaTiO 3 nanoparticles," in *Integrated Ferroelectrics*, 2011, vol. 127, no. 1, pp. 178–183. doi: 10.1080/10584587.2011.576122.

[39] J. Feng and H. C. Zeng, "Size-controlled growth of Co3O4 nanocubes," *Chemistry of Materials*, vol. 15, no. 14, pp. 2829–2835, Jul. 2003, doi: 10.1021/cm020940d.

[40] F. Dang, "In situ growth BaTiO 3 nanocubes and their superlattice from an aqueous process," *Nanoscale*, vol. 4, no. 4, pp. 1344–1349, Feb. 2012, doi: 10.1039/c2nr11594h.

[41] Q. Ma, K. I. Mimura, and K. Kato, "Diversity in size of barium titanate nanocubes synthesized by a hydrothermal method using an aqueous Ti compound," *CrystEngComm*, vol. 16, no. 36, pp. 8398–8405, Sep. 2014, doi: 10.1039/c4ce01195c.

[42] Y. Zheng, "Synthesis and performance study of zinc borate nanowhiskers," *Colloids and Surfaces A: Physicochemical and Engineering Aspects*, vol. 339, no. 1–3, 2009, doi: 10.1016/j.colsurfa.2009.02.018.

[43] Z. Sun, "Experimental and simulation-based understanding of morphology controlled barium titanate nanoparticles under co-adsorption of surfactants," *CrystEngComm*, vol. 19, no. 24, pp. 3288–3298, 2017, doi: 10.1039/c7ce00279c.

[44] M. Vara, M. Chi, and Y. Xia, "Facile Synthesis of BaTiO3 Nanocubes with the Use of Anatase TiO2 Nanorods as a Precursor to Titanium Hydroxide," *ChemNanoMat*, vol. 2, no. 9, pp. 873–878, Sep. 2016, doi: 10.1002/cnma.201600164.

[45] K. C. Huango, T. C. Huango, and W. F. Hsieh, "Morphology-controlled synthesis of barium titanate nanostructures," *Inorganic Chemistry*, vol. 48, no. 19, pp. 9180–9184, 2009, doi: 10.1021/ic900854x.

[46] S. Adireddy, C. Lin, B. Cao, W. Zhou, and G. Caruntu, "Solution-based growth of monodisperse cube-like BaTiO3 colloidal nanocrystals," *Chemistry of Materials*, vol. 22, no. 6, pp. 1946–1948, Mar. 2010, doi: 10.1021/cm9038768.

[47] A. E. Souza, “Photoluminescence of SrTiO 3: Influence of particle size and morphology,” *Crystal Growth and Design*, vol. 12, no. 11, pp. 5671–5679, Nov. 2012, doi: 10.1021/cg301168k.

[48] J. Muro-Cruces, “Precise Size Control of the Growth of Fe3O4 Nanocubes over a Wide Size Range Using a Rationally Designed One-Pot Synthesis,” *ACS Nano*, 2019, doi: 10.1021/acsnano.9b01281.

[49] L. Qiao, “Standardizing Size- and Shape-Controlled Synthesis of Monodisperse Magnetite (Fe3O4) Nanocrystals by Identifying and Exploiting Effects of Organic Impurities,” *ACS Nano*, vol. 11, no. 6, 2017, doi: 10.1021/acsnano.7b02752.

[50] K. Tsukiyama, M. Takasaki, Y. Oaki, and H. Imai, “Evolution of Co3O4 Nanocubes through Stepwise Oriented Attachment,” *Langmuir*, vol. 35, no. 24, pp. 8025–8030, Jun. 2019, doi: 10.1021/acs.langmuir.9b00342.

[51] Y. Bai, T. Yang, Q. Gu, G. Cheng, and R. Zheng, “Shape control mechanism of cuprous oxide nanoparticles in aqueous colloidal solutions,” *Powder Technology*, vol. 227, pp. 35–42, Sep. 2012, doi: 10.1016/j.powtec.2012.02.008.

[52] E. Ko, J. Choi, K. Okamoto, Y. Tak, and J. Lee, “Cu2O nanowires in an alumina template: Electrochemical conditions for the synthesis and photoluminescence characteristics,” *ChemPhysChem*, vol. 7, no. 7, 2006, doi: 10.1002/cphc.200600060.

[53] M. L. F. Nascimento, E. B. Ferreira, and E. D. Zanotto, “Kinetics and mechanisms of crystal growth and diffusion in a glass-forming liquid,” *Journal of Chemical Physics*, vol. 121, no. 18, 2004, doi: 10.1063/1.1803813.

[54] C. L. de Castro and B. S. Mitchell, “Crystal growth kinetics of nanocrystalline aluminum prepared by mechanical attrition in nylon media,” *Materials Science and Engineering A*, vol. 396, no. 1–2, 2005, doi: 10.1016/j.msea.2005.01.008.

[55] J. R. C. Mateo, A. L. Salut, and M. C. Marquez, “Surfactant assisted sol-gel synthesis of nickel oxide nanostructures,” in *Materials Science Forum*, 2018, vol. 916 MSF, pp. 74–78. doi: 10.4028/www.scientific.net/MSF.916.74.

[56] G. Bai, “The microemulsion preparation and high catalytic performance of mesoporous NiO nanorods and nanocubes for toluene combustion,” *Chemical Engineering Journal*, vol. 219, pp. 200–208, Mar. 2013, doi: 10.1016/j.cej.2013.01.008.

[57] W. Wu, R. Hao, F. Liu, X. Su, and Y. Hou, “Single-crystalline α-Fe2O3 nanostructures: Controlled synthesis and high-index plane-enhanced photodegradation by visible light,” *Journal of Materials Chemistry A*, vol. 1, no. 23, pp. 6888–6894, Jun. 2013, doi: 10.1039/c3ta10886d.

[58] T. Taniguchi, K. I. Katsumata, S. Omata, K. Okada, and N. Matsushita, “Tuning growth modes of ceria-based nanocubes by a hydrothermal method,” *Crystal Growth and Design*, vol. 11, no. 9, pp. 3754–3760, Sep. 2011, doi: 10.1021/cg101585b.

[59] Q. Wu, “Great influence of anions for controllable synthesis of CeO2 nanostruetures: From nanorods to nanocubes,” *Journal of Physical Chemistry C*, vol. 112, no. 44, pp. 17076–17080, Nov. 2008, doi: 10.1021/jp804140e.

[60] T. J. Fisher, M. Wang, Y. Ibrahim, B. Steffensmeier, and C. L. Cheung, “Effect of sodium nitrate on microwave-assisted synthesis of ceria nanocubes,” *Materials Letters*, vol. 178, pp. 71–74, Sep. 2016, doi: 10.1016/j.matlet.2016.04.186.

[61] O. Mendiuk, M. Nawrocki, and L. Kepinski, “The synthesis of Ce1-xLnxO2-y (Ln=Pr, Sm, Gd, Tb) nanocubes by hydrothermal methods,” *Ceramics International*, vol. 42, no. 1, pp. 1998–2012, Jan. 2016, doi: 10.1016/j.ceramint.2015.10.006.

[62] M. Niederberger, G. Garnweitner, N. Pinna, and G. Neri, “Non-aqueous routes to crystalline metal oxide nanoparticles: Formation mechanisms and applications,” *Progress in Solid State Chemistry*, vol. 33, no. 2-4 SPEC. ISS., 2005, doi: 10.1016/j.progsolidstchem.2005.11.032.

[63] D. Yu, N. X. Xu, L. Hu, Q. L. Zhang, and H. Yang, “Nanocomposites with BaTiO3-SrTiO3 hybrid fillers exhibiting enhanced dielectric behaviours and energy-storage densities,” *Journal of Materials Chemistry C*, vol. 3, no. 16, 2015, doi: 10.1039/c4tc02972k.

[64] D. Zhu, H. Yan, S. Tian, and Z. Wang, “Size, Shape, and Material Effects in Ferroelectric Octahedral Nanoparticles,” *Journal of Nanomaterials*, vol. 2021, 2021, doi: 10.1155/2021/2371168.

[65] N. Nuraje and K. Su, “Perovskite ferroelectric nanomaterials,” *Nanoscale*, vol. 5, no. 19. 2013. doi: 10.1039/c3nr02543h.

[66] M. J. Polking, A. P. Alivisatos, and R. Ramesh, “Synthesis, physics, and applications of ferroelectric nanomaterials,” *MRS Communications*, vol. 5, no. 1. 2015. doi: 10.1557/mrc.2015.8.

[67] Yuanbing Mao, Hongjun Zhou, and Stanislaus S. Wong, “Synthesis, Properties, and Applications of Perovskite-Phase Metal Oxide Nanostructures Properties of Perovskite Systems,” *Material Matters*, vol. 5, no. 2, 2010.

[68] Ö. Küçük, S. Teber, İ. Cihan Kaya, H. Akyıldız, and V. Kalem, “Photocatalytic activity and dielectric properties of hydrothermally derived tetragonal BaTiO3 nanoparticles using TiO2 nanofibers,” *Journal of Alloys and Compounds*, vol. 765, 2018, doi: 10.1016/j.jallcom.2018.06.165.

[69] K. Fujinami, K. Katagiri, J. Kamiya, T. Hamanaka, and K. Koumoto, “Sub-10 nm strontium titanate nanocubes highly dispersed in non-polar organic solvents,” *Nanoscale*, vol. 2, no. 10, pp. 2080–2083, Oct. 2010, doi: 10.1039/c0nr00543f.

[70] M. Borah and D. Mohanta, “Composite-hydroxide-mediated formation of barium titanate nanocubes and their optical emission response,” *Chinese Journal of Physics*, vol. 53, no. 1, pp. 1–11, 2015, doi: 10.6122/CJP.20140804C.

[71] B. Hou, Y. Xu, D. Wu, and Y. Sun, “Preparation and characterization of single-crystalline barium strontium titanate nanocubes via solvothermal method,” *Powder Technology*, vol. 170, no. 1, pp. 26–30, Nov. 2006, doi: 10.1016/j.powtec.2006.08.010.

[72] K. I. Mimura and K. Kato, “Dielectric properties of barium titanate nanocube ordered assembly sintered at various temperatures,” in *Japanese Journal of Applied Physics*, Oct. 2014, vol. 53, no. 9. doi: 10.7567/JJAP.53.09PA03.

[73] K. I. Mimura, K. Kato, H. Imai, S. Wada, H. Haneda, and M. Kuwabara, “Fabrication and characterization of dielectric nanocube self-assembled structures,” in *Japanese Journal of Applied Physics*, Sep. 2012, vol. 51, no. 9 PART 2. doi: 10.1143/JJAP.51.09LC03.

[74] K. I. Mimura, “Characterization of dielectric nanocubes ordered structures fabricated by solution self-assembly process,” *Japanese Journal of Applied Physics*, vol. 50, no. 9 PART 3, Sep. 2011, doi: 10.1143/JJAP.50.09NC09.

[75] K. I. Mimura and K. Kato, “Fabrication and piezoresponse properties of {100} BaTiO3 films containing highly ordered nanocube assemblies on various substrates,” *Journal of Nanoparticle Research*, vol. 15, no. 10, Oct. 2013, doi: 10.1007/s11051-013-1995-5.

[76] Q. Ma and K. Kato, “Crystallographic fusion behavior and interface evolution of mono-layer BaTiO3 nanocube arrangement,” *CrystEngComm*, vol. 18, no. 9, pp. 1543–1549, 2016, doi: 10.1039/c5ce02235e.

[77] C. Hammond, “The Basics of Crystallography and Diffraction (2nd edn),” *Measurement Science and Technology*, vol. 13, no. 2, 2002, doi: 10.1088/0957-0233/13/2/708.

[78] N. W. Gregory, “Elements of X-Ray Diffraction,” *J Am Chem Soc*, vol. 79, no. 7, 1957, doi: 10.1021/ja01564a077.

[79] D. G. Capco and Y. Chen, *Nanomaterial impacts on Cell Biology and Medicine*, vol. 811. 2014.

[80] G. A. Waychunas, C. S. Kim, and J. F. Banfield, “Nanoparticulate iron oxide minerals in soils and sediments: Unique properties and contaminant scavenging mechanisms,” in *Journal of Nanoparticle Research*, 2005, vol. 7, no. 4–5. doi: 10.1007/s11051-005-6931-x.

[81] P. L. Houston, R. Conte, and J. M. Bowman, “Collisional energy transfer in highly excited molecules,” *Journal of Physical Chemistry A*, vol. 118, no. 36, 2014, doi: 10.1021/jp506202g.

[82] J. C. Crittenden, R. R. Trussel, D. W. Hand, K. J. Howe, and G. Tchobanoglous, “MWH’s Water Treatment: Principles and Design,” in *John Wiley & Sons, Inc*, 2012.

[83] A. Pierres, A. M. Benoliel, C. Zhu, and P. Bongrand, “Diffusion of microspheres in shear flow near a wall: Use to measure binding rates between attached molecules,” *Biophysical Journal*, vol. 81, no. 1, 2001, doi: 10.1016/S0006-3495(01)75677-9.

[84] A. R. Roosen, R. P. Mccormack, and W. C. Carter, “Wulffman: A tool for the calculation and display of crystal shapes,” 1998.